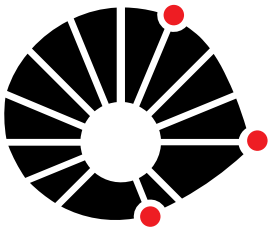

UNICAMP

UNIVERSIDADE ESTADUAL DE CAMPINAS

Instituto de Física "Gleb Wataghin"

PEDRO HENRIQUE PINHEIRO CINTRA

Supernova observation and distance estimation using neutrino detectors

Campinas

08/2023

Pedro Henrique Pinheiro Cintra

Supernova observation and distance estimation using neutrino detectors

Dissertação apresentada ao Instituto de Matemática, Estatística e Computação Científica da Universidade Estadual de Campinas como parte dos requisitos exigidos para a obtenção do título de Mestre em Física.

Supervisor: Ernesto Kemp

Este exemplar corresponde à versão final da Dissertação defendida pelo aluno Pedro Henrique Pinheiro Cintra e orientado pelo Prof. Dr. Ernesto Kemp.

Campinas

08/2023

Ficha catalográfica
Universidade Estadual de Campinas
Biblioteca do Instituto de Física Gleb Wataghin
Lucimeire de Oliveira Silva da Rocha - CRB 8/9174

C493s

Cintra, Pedro Henrique Pinheiro, 1996-
Supernova observation and distance estimation using neutrino detectors / Pedro Henrique Pinheiro Cintra. – Campinas, SP : [s.n.], 2023.

Orientador: Ernesto Kemp.
Dissertação (mestrado) – Universidade Estadual de Campinas, Instituto de Física Gleb Wataghin.

1. Supernova (Estrela). 2. Detectores de neutrinos. 3. Astrofísica de partículas. 4. Detecção de supernova. I. Kemp, Ernesto, 1965-. II. Universidade Estadual de Campinas. Instituto de Física Gleb Wataghin. III. Título.

Informações Complementares

Título em outro idioma: Observação de supernovas e estimativa de distâncias utilizando detectores de neutrinos
Palavras-chave em inglês:
Supernovae
Neutrinos detectors
Astroparticle physics
Supernova detection
Área de concentração: Física Aplicada
Titulação: Mestre em Física
Banca examinadora:
Pedro Cunha de Holanda
Arlene Cristina Aguilar
Kate Scholberg
Data de defesa: 04-10-2023
Programa de Pós-Graduação: Física

Identificação e informações acadêmicas do(a) aluno(a)
- ORCID do autor: https://orcid.org/0000-0001-6604-3597
- Currículo Lattes do autor: http://lattes.cnpq.br/1191661313631770

INSTITUTO DE FÍSICA
GLEB WATAGHIN

MEMBROS DA COMISSÃO EXAMINADORA DA DISSERTAÇÃO DE MESTRADO DO ALUNO PEDRO HENRIQUE PINHEIRO CINTRA - RA 235648, APRESENTADA E APROVADA AO INSTITUTO DE FÍSICA GLEB WATAGHIN, DA UNIVERSIDADE ESTADUAL DE CAMPINAS, EM 04/10/2023.

COMISSÃO JULGADORA:

- Prof. Dr. Pedro Cunha de Holanda – Presidente (IFGW/UNICAMP)

- Profa. Dra. Arlene Cristina Aguilar (IFGW/UNICAMP)

- Dra. Kate Scholberg (Duke University)

OBS.: Ata da defesa com as respectivas assinaturas dos membros encontra-se no SIGA/Sistema de Fluxo de Dissertação/Tese e na Secretaria do Programa da Unidade.

CAMPINAS

2023

This work is dedicated to all my friends and loved ones, who are the reason I was able to complete this step

Acknowledgements

Mais uma vez na vida me deparo com esta etapa, que talvez seja uma das mais difíceis de todo o trabalho. Tentarei não me estender muito. Assim como feito em meu trabalho de conclusão de curso, seguirei uma ordem cronológica.

Agradeço primeiramente aos meus pais, pelo apoio e as virtudes que a mim ensinaram. Agradeço também a todos os amigos de infância que até hoje se encontram presentes em minha vida, Rafa, Henrique, Lucas e Tati, ter crescido com vocês me rende sempre boas memórias e guardo memórias de todos com carinho. Minha família como um todo também não poderia ficar de fora, todos os meus primos e primas, tios e tias e vovó, o apoio de vocês é muito importante e as brincadeiras que vivemos juntos sempre foi algo que tive certeza que moldou parte do meu jeito ninja de ser.

Chegamos então em meus mais queridos amigos da graduação: Igor, Vavá, João, Lud, Felipe, Ranier, Batata, Paulo, Vitor Dantas, Vitor Machado, Bedorah, Mari, Caio e Borraxa. No início desse mestrado, estávamos no ápice da pandemia de COVID-19, eu nunca teria continuado neste trabalho se não fossem todas as tardes e noites que passamos jogando, conversando e até trabalhando remotamente, porém juntos. Se não fossem os projetos paralelos que desenvolvemos nesse período, minha mente teria se deteriorado infinitamente mais. Obrigado a todos vocês, hoje só cheguei aonde cheguei graças a vocês.

Ainda neste grupo de amigos, algumas eu não posso deixar de mencionar de forma mais particular. Igor, muito obrigado pela sua companhia, pelos diversos audios trocados e rolês feitos, ter você morando em uma cidade por perto é sempre um conforto que carrego dentro de mim. Vavá, se hoje eu decidi explorar o fantástico mundo da ecologia teórica, você teve tudo a ver com isso. Você é um cientísta incrível e uma das pessoas, senão a pessoa, mais inteligente que eu já conheci. João, fico muito feliz que a distância de alguns milhares de quilômetros não tenha diminuído nossa amizade, anseio muito por te ver e agradeço por ter se feito disponível para mim tantas e tantas vezes. Finalmente, Mari, sinto muita saudade de ti e sempre adoro conversar com você, também fico muito feliz que a distância continental não enfraqueceu nossa proximidade. Ter você e o Vavá aqui por perto nos primeiros meses em que me mudei para Campinas fez toda a diferença.

E por falar em minha mudança para Campinas, é impossível não mencionar a Giovanna, Luísa, Du, Berg, Alvarez, Bidu, Vitor, Jacinto, Kalebe, Lu, Be e Jão. Vocês todos foram as pessoas mais incríveis que eu podia conhecer aqui em Campinas. Berg e Alvarez, eu nunca teria conseguido fazer o que fiz neste trabalho se não tivesse vocês dois dividindo sala comigo. Bidu, Vitor e Jacinto, vocês são companhias maravilhosas e para sempre guardarei com carinho as memórias de nossos rolês, obrigado a cada um de vocês

por me ensinar tanto sobre os mais diversos assuntos.

Passamos então para a parte mais recente. A todos os amigos que fiz durante o curso de verão de ecologia teórica em São Paulo: Anna, Amanda, Pedro, Pedro, Sarah, Tiago, Kalu, Joka e Dani. Vocês todos moram no meu coração (a Anna mais hihihi). Quando entre naquele curso nunca imaginaria o impacto que ele e as pessoas que conheci teriam na minha vida. Em dois meses fiz amizades tão íntimas que sinto que os conheço a anos. Obrigado a todos por me ajudarem e me guiarem nesse processo de transição física → ecologia.

Aqui entra um agradecimento ainda neste grupo de amigos, porém extremamente importante. Anna, você é a inspiração que eu busco todos os dias. Todas as vezes em que penso em um modelo de cientista dentro da ecologia teórica, você me vem a mente. Sem você em minha vida eu garanto que a qualidade da escrita deste trabalho seria muito menor. Obrigado por estar comigo no final dessa fase e me apoiar constantemente, espero conseguir retornar para você toda a alegria e bem-estar que você me traz. Sinto que o nosso futuro juntos é brilhante e prazeroso. Te amo infinitamente, você é a paixão da minha vida.

Finalmente, chegamos aos meus queridos professores e orientadores, Flávia Marquitti, Pedro Holanda, Arlene Cristina, Orlando Peres, Pablo de Castro, Pizza, Fabrício e Glauco. Cada um me trouxe ensinamentos, tanto sobre o mestrado quanto sobre a ciência, e me inspiraram a tentar ser cada vez mais como vocês em algum aspecto. Claro que não poderia deixar de fora, o meu grande orientador Ernesto Kemp, que se mostrou extremamente empolgado com este projeto e compartilhou diversas ideias comigo. Obrigado a todos por me orientarem, cada um do seu jeito.

E por fim, eu agradeço a Unicamp, por me propiciar um ambiente sem igual para estudar e trabalhar.

Desejo a todos o melhor que a vida pode oferecer.

O presente trabalho foi realizado com apoio da Coordenação de Aperfeiçoamento de Pessoal de Nível Superior - Brasil (CAPES) - Código de Financiamento 001

This study was financed in part by the Coordenação de Aperfeiçoamento de Pessoal de Nível Superior - Brasil (CAPES) - Finance Code 001

"Somewhere, something incredible is waiting to be known."
(Carl Sagan)

Resumo

Desde a observação da SN1987 pelo detector Kamiokande, a sensibilidade de detectores de neutrinos aumentou drasticamente. Nos próximos anos, uma nova geração de detectores está programada para entrar em operação. Dentre os objetivos destes detectores, está a observação de uma supernova de colapso estelar através do espectro de neutrinos, fenômeno no qual se espera ser capaz de produzir observações físicas ricas em dados e fornecer respostas para tanto a física de neutrinos como a astrofísica de supernovas. Neste trabalho, consideramos a observação futura de supernovas com detectores da atual e próxima geração. Desenvolvemos um código em Python de acesso livre para simular a detecção de tais eventos, levando em conta o efeito de matéria terrestre na oscilação de neutrinos, e usamos métodos estatísticos para reconstruir a distância de supernovas de colapso estelar simuladas, tendo o espectro de energias dos neutrinos observados. Ainda mais, investigamos alguns métodos para usar detectores Cherenkov afim de obter a direção destes eventos, melhorando a habilidade de determinar a localização da supernova através de neutrinos.

Palavras-chave: Supernovas, detector de neutrinos, astropartículas, detecção de supernovas

Abstract

Since the observation of SN1987 by the Kamiokande-II, the IMB and the Baksan detectors, the sensitivity of neutrino detectors has increased drastically. In the coming years, a new generation of neutrino detectors is scheduled to be in operation. One of the main objectives of neutrino detectors is to observe a core-collapse supernova in the neutrino spectrum, a phenomenon that is expected to produce physics rich data and provide answers to both neutrino physics and astrophysics. In this work, we consider the future observation of supernovae using current and next generation detectors. We develop a python code fully open source in order to simulate the detection of such events, taking into account the Earth matter effect in neutrino oscillations, and use statistical methods to reconstruct the distance of a core collapse supernova, given the neutrino energy spectrum observed. On top of that, we investigate methods for using water Cherenkov detectors to obtain the direction of the event.

Keywords: Supernovas, neutrino detector, astroparticle physics, supernova detection

List of Figures

List of Tables

List of Source Codes

Todos os códigos desenvolvidos neste trabalho serão disponibilizados através de uma biblioteca em Python para uso livre. Atualmente, enquanto a biblioteca não está pronta, todos os códigos podem ser encontrados no meu repositório do GitHub.

All code developed in this work will be compiled in a Python library for free usage. While not ready, the entire code may be found on my GitHub repo.

Contents

Preface

What is my objective with this work? That is the question I kept in my head while writing. Every time I though about what should be included or excluded from this work, that is the question that came to my head. In the end I want this to be a useful work for future MsC or PhD students, and I hope to achieve this goal. Aiming to this goal, I decided to give more details to the first chapters, as a result I acknowledge that this dissertation is big. That's the price I paid. If you are reading this work and is familiar to stellar life cycle and neutrino oscillations, you can very well skip the first three chapters. Maybe for you they will only serve as little references for you to check something while reading the other chapters. But for students fresh from their undergraduation, stating their Masters or PhDs, I know how a detailed thesis is worth more than dozens of papers on the subject.

The second objective with this work is to provide some sort of "physics behind the code" text for anyone who might, in the future, use the Python library I build or that I contribute to. Other libraries for simulating supernova neutrinos already exist in other programming languages (check SNOwGLoBES for example), but I know that the Python community is an always growing one and as my personal view, building a library for Python users is a great contribution to the young scientific community.

Update Nov 2023: An effort for building a Python package for simulating supernova neutrinos is already on the way with SNEWPY. Thus, there appears to be no point in building a library of my own, and the objective of my code is to provide a contribution to the SNEWPY package.

Aiming at these two main objectives, I tried to write a text that suits these tasks better. Some redundancies were placed on purpose throughout the text, in order to avoid the reader some forgetting. I tried producing visual and pleasing figures to help guiding the reader. Some historical references are here just as a way of providing the reader an easy access to the history of physics itself. There are some footnotes with personal recommendations for external content on some topic, for those who become curious. And finally, it is not my objective to write a book, thus there was a limit to how didatic or even self-consistent I could be. It was assumed during the writing of this work that the reader is at least a fresh graduated student from his/her/their undergraduate course. I hope you have a great reading.

Introduction

In 1987, the Kamiokande II neutrino detector, the Irvine–Michigan–Brookhaven detector and the Baksan Neutrino Observatory made the first observation of a core collapse supernova burst through neutrinos. The detection gave birth to the field of neutrino astronomy, i. e., the study of astrophysical events such as Gamma Ray Bursts (GRB) and supernovae using neutrino fluxes that arrive from these events [8, 9]. Given the nature of neutrino interactions, the emission of neutrinos from a dying star occurs prior to the burst of light. In fact, the neutrino signal arrived two to three hours earlier than light from SN1987 could be observed.

Today, the SuperNova Early Warning System (SNEWS) uses advantage of the early arrival of neutrinos to serve as an alarm for supernovae, indicating to optical telescopes that the electromagnetic signal of a supernova is about to reach Earth, in order to capture the incoming photons from the event [10]. Futhermore, the possibility of using neutrino detectors alongside gravitational wave detectors to observe neutron star mergers in the multimessenger framework allows a maximal extraction of information and inference of the physical processes in astrophysical events [11]. However, supernovas are not a common event and the only observation ever made using neutrinos is the SN1987A. With only 25 neutrinos being detected, this single event provides little information regarding the physics of neutrino production and star core collapse. Aiming to capture more events when the next supernova occurs and investigate with more precision the core collapse mechanism, laboratories around the world prepare the next generation of neutrino detectors, such as the Deep Underground Neutrino Detector (DUNE) and the Hyper-Kamiokande.

Therefore, at this moment numerical simulations provide our best tool for the study of supernova neutrino detection on current generation detectors and the next generation ones. In this project, we aim to use numerical and theoretical tools to evaluate how the detection of neutrinos from supernovae may provide information regarding the characteristics of the explosion, the distance and the location. We plan to investigate how the distance affects the information extracted from the detection.

It is important to state here that from now on, whenever the term “supernova” is used, it refers to core collapse supernova, not including type Ia supernovae [12].

Part I

Neutrino Production and Emission by Supernovae

1 Supernova Explosion Mechanism

This chapter describes the mechanism in which massive stars collapse and explode, and the production of neutrinos and antineutrinos during this process.

> Our bodies are made of supernova dust, the epitome of ultimate destruction and shatter. And though we are whole, beings with bodies and souls, with cosmos in our eyes and black heart holes, we love as fiercely as the force of creation.
>
> *Hubert Martin*

In ancient China during the end of the Han dynasty, in the year 185 AD, there were reports of a bright star that suddenly appeared in the sky, shining strong for a couple of weeks and then vanished. This type of star was mentioned in the Chinese historical book *Houhanshu* by the name "guest star". At first, modern scholars believed this guest star to be actually a comet [13]. However, recent evidence from descriptions of comets at the same period and the linguistics of the guest star's mentions suggests that the reports of were probably the first written register of a supernova in the sky [14]. The same supernova was also probably recorded in Roman texts, with mentions of it shinning for a few days brighter than Venus [15]. Later, in 393, during the Qing dynasty, another guest star was reported by Chinese astronomers, with modern astronomical observations pointing again to a supernova as the culprit [16]. In 1054, again a bright star became visible to Chinese and Japanese astronomers, being associated with the supernova explosion that created the Crab Nebula (Figure 1), the first astronomical object to recognized as being linked to a supernova [17, 18]. The latest sighting of a supernova shining in the sky was in 1987, as mentioned before.

Throughout this chapter we take look into the mechanism that drives the explosion of massive stars, producing the supernovas observable by human's eyes and the neutrinos, observable by the human's detectors. The curious reader seeking more information may read [19].

1.1 Stellar Evolution

Stars, like our Sun, are astrophysical bodies sustained by the balance between their own gravity and the internal pressure generated by nuclear fusion deep in their cores.

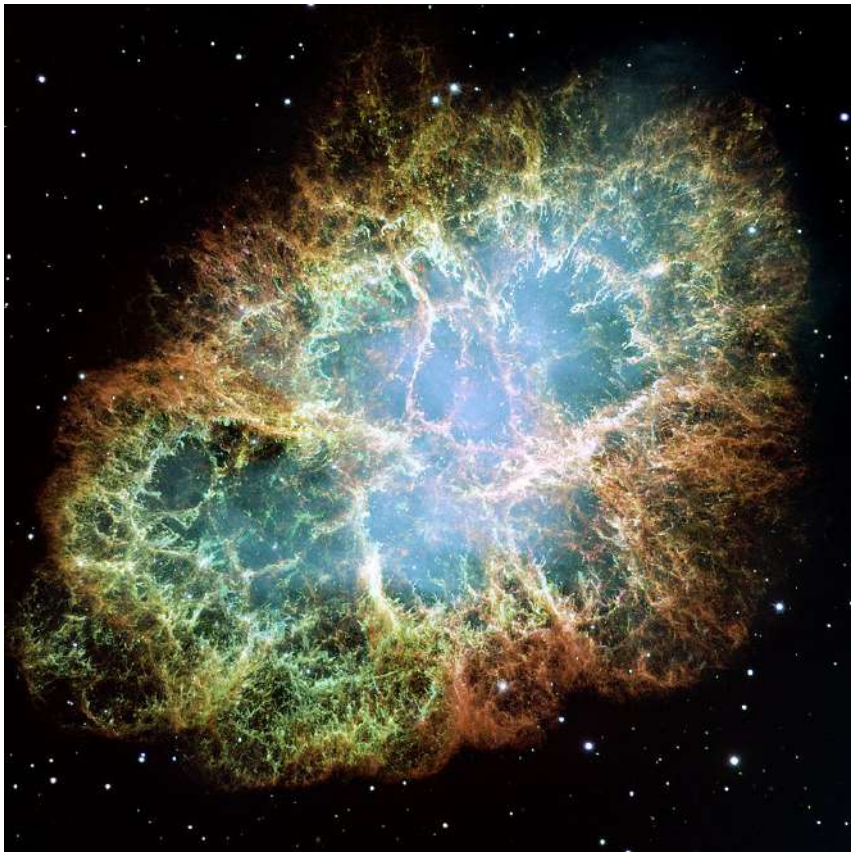

Figure 1 – Mosaic image from the Hubble Space Telescope of the Crab Nebula (designations M1, NGC 1952, Taurus A). Composed of 24 individual Wide Field and Planetary Camera 2 exposures.

Stars are formed in regions of space where matter densities are high, in big gas clouds made of almost only hydrogen, the so-called stellar nursery, such as the Orion Nebula (Figure 2) [20]. As the gas collapses gravitationally, the temperature and pressure increases eventually leads to the formation of a protostar. The protostar then accretes mass until the threshold of $0.08 M_{\odot}$ is reached and nuclear fusion ignites in the core, promoting the protostar to a main sequence star [21].

Once the accretion of mass in the gas cloud reaches nuclear fusion threshold, the temperature and pressure in the core became high enough to ignite the fusion of hydrogen into helium through several paths such as the proton-proton chain (p-p chain), the most common pathway for hydrogen fusion. In the p-p chain, two hydrogen atoms (^{1}H) fuse into a deuteron (^{2}D), emitting a positron and an electron neutrino. The deuteron is fused with another hydrogen, resulting in helium-3 (^{3}He). Two cores of ^{3}He then fuse and create the more stable ^{4}He releasing two protons.

$$
\begin{aligned}
{}^{1}\mathrm{H} + {}^{1}\mathrm{H} &\rightarrow {}^{2}\mathrm{D} + e^{+} + \nu_{e}, \\
{}^{2}\mathrm{D} + {}^{1}\mathrm{H} &\rightarrow {}^{3}\mathrm{He} + \gamma, \\
{}^{3}\mathrm{He} + {}^{3}\mathrm{He} &\rightarrow {}^{4}\mathrm{He} + 2p + \gamma.
\end{aligned}
$$

From this point forward, stars spend most of their life in the main sequence[1], fusing hydrogen into helium. When main sequence stars begin exhausting the hydrogen in their core, the pressure released by nuclear fusion decreases and the star contracts. That contraction increases the pressure and temperature in the core, driving a faster fusion of helium into carbon, carbon into neon and oxygen, then silicon and finally iron. This processes increases the internal pressure and pushes back against the outer layers of the star, making it grow bigger. That is the so-called giant phase [22, 23].

Figure 2 – Composed image of the Orion Nebula, captured by the Hubble Space Telescope in 2006.

Iron is the chemical element with the highest binding energy per nucleon, thus the fusion of iron into heavier elements does not release energy, i. e. the stellar

[1] The main sequence is a continuous region observed in HR-diagrams of temperature per luminosity. Most stars are found within this region, obeying well established relations connecting their temperature with their luminosity. For the curious reader, I recommend a Youtube video about the size and life of the stars from the channel Kurzgesagt - In a Nutshell with the title The biggest star in the universe.

nucleosynthesis stops at iron. From this point, the star keeps burning elements into iron, increasing the mass of the core. The final profile of the star is an onion like structure with lighter elements on the outer layers (Figure 3).

As the iron core grows in mass and size, the pressure generated from nuclear fusion decreases. Finally, when the core mass hits the Chandrasekhar limit between $1.38M_{\odot}$ to $1.8M_{\odot}$, the nuclear fusion completely stops, electrons are captured by the iron nuclei and the core becomes unable to support itself [24].

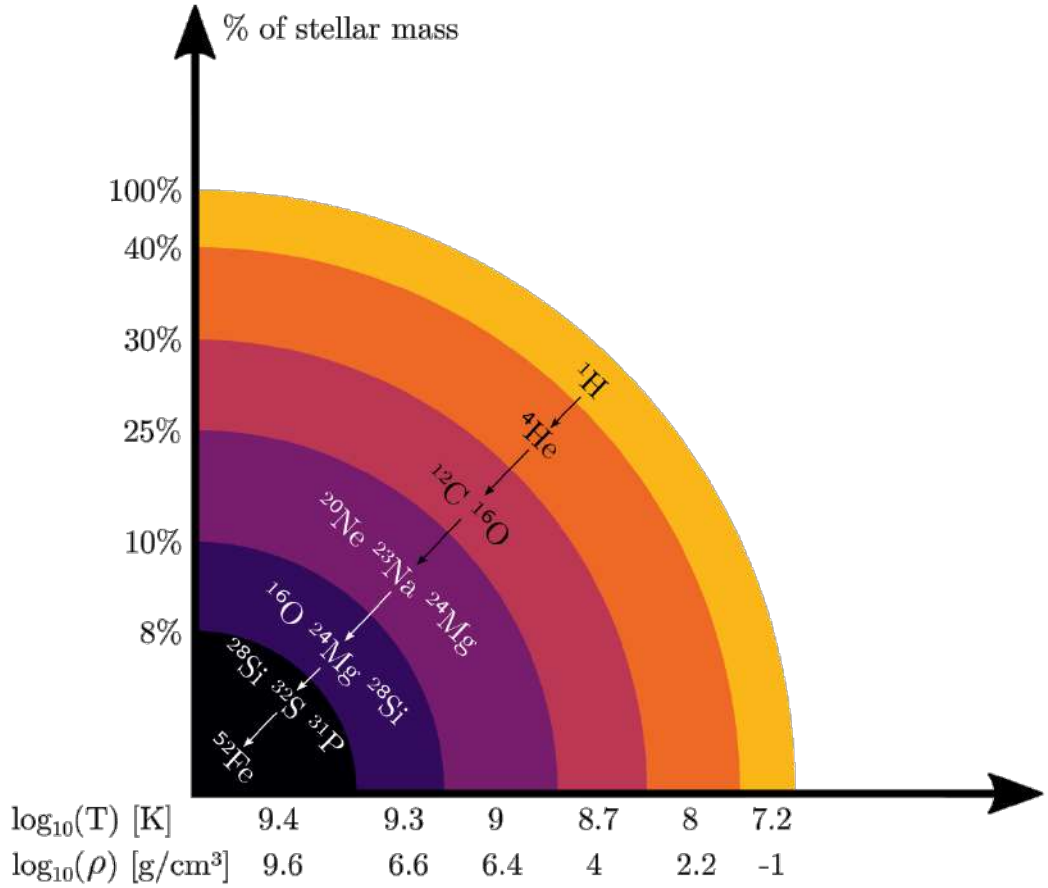

Figure 3 – Onion like structure of a massive star. The horizontal axis represents the values of each stellar layer according to [1]. The percentages in the vertical axis indicate the fraction of mass below the transition between layers, for example, 40% of the star mass is below the hydrogen layer [2].

1.2 Onset of Collapse

The iron core is mostly an homogeneous dense sphere sustained by electron degeneracy pressure, associated with the Fermi-Dirac distribution for fermions, preventing more than one electron from occupying the same state as another, which creates a outward pressure that opposes the compression of matter, alongside the internal pressure from

thermonuclear fusion. For massive stars ($M \geqslant 8M_{\odot}$), the halting of thermonuclear fusion of iron drives the compression of the star, leading to a increased pressure on top of the star's nucleus. The electron degeneracy pressure is not enough to counteract the gravitational force and the star collapses on top of the nucleus.

As matter is squeezed tighter and temperatures in the core reach 10^{10}K, thermal photons became energetic enough to partially disintegrate iron nuclei into α-particles and free nucleons, releasing neutrinos in the process. At the same time, electron-capture by the protons produces electron neutrinos (reaction 1.1), which initially escape from the dying star. As a result of this process, neutron-rich nuclei are produced, leading to the phase known as *neutronization*.

Once the density of the core exceeds 10^{12}g/cm^3 the core becomes opaque to neutrinos, trapping electron neutrinos, that enter thermal equilibrium with the stellar plasma and form a degenerate Fermi gas until the core density reach the order of 10^{14}g/cm^3 and the nucleon repulsive force halts the compression [25]. The outer shells bounce off the core, creating a shock wave that travels back to the star's surface, exploding the outer regions of the star and releasing a neutrino burst in a tens of milliseconds [26]. Shortly after the neutronization burst, beta decay drives the production of anti-electron neutrinos (reaction 1.2) [2]. Since almost no energy escapes from the collapsing star by the first electron neutrinos that escape before opacity is reached, the collapse of a stellar core is almost adiabatic [27]. Due to a lower coupling constant of the weak interaction, compared to the electromagnetic interaction, neutrinos reach the surface of the star before photons, since photons interact with matter on the way[2].

$$e^{-} + p \rightarrow n + \nu_e, \tag{1.1}$$

$$n \rightarrow p + e^{-} + \overline{\nu}_e. \tag{1.2}$$

1.3 The Explosion

Milliseconds after the neutrino trapping, the star's center reaches nuclear matter densities, where nuclei dissolve into a uniform nuclear medium. The phase transition induces a sharp rise in the incompressibility of the core, due to strong nuclear repulsion between nuclei. The infalling layers bounce on the hard core, initiating a shock wave that travels outwards supersonically, ejecting the star's material in a violent explosion (Fig 4 part 3).

[2] Again I recommend an YouTube video on the topic, this time the video Neutron Stars: The Most Extreme Object that aren't Black Holes, by Kurzgesagt. Also for a technical review on the subject, check ref [3].

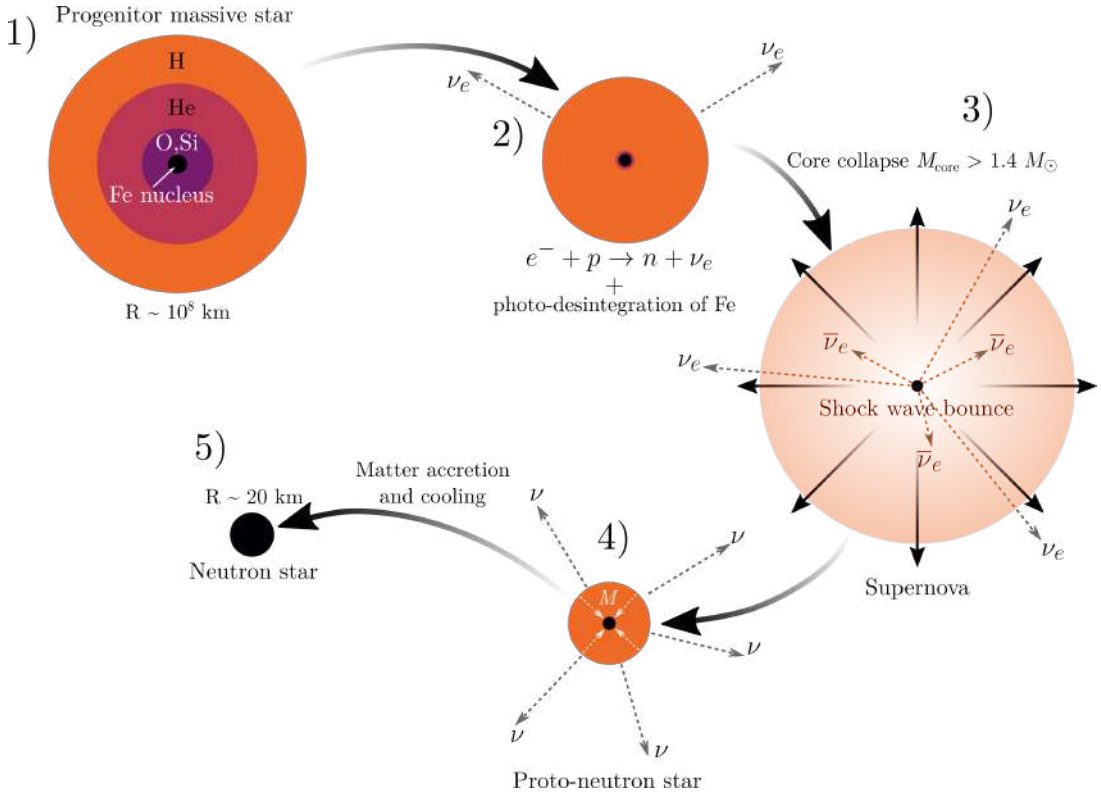

Figure 4 – Dynamics of core collapse supernova. The progenitor star initiates instability with an onion-like structure (1). While the nucleus is compressed by the top layers of the star, a few electron neutrinos generated by electron-capture and photo-desintegration of iron escape the star (2). Shortly after, the core reaches critical density to become opaque to neutrinos, trapping these particles until the top layers bounce of the hard core, expelling the star material and releasing the trapped neutrinos. Electron antineutrinos electron are created shortly after the electron ones due to beta decay of the neutron rich matter (3). The remaining mass forms a proto-neutron star, from which mass accretion and cooling drive emission of neutrinos from all flavors, represented by the symbol ν without subscript (4). Finally, a neutron star is left from the explosion (5).

During the propagation of the shock wave, the density of the medium drops to the point where matter is again transparent to neutrinos. That releases a burst of electron neutrinos in what is called *neutronization burst*.

As the shock wave weakens, matter is accreted to the core for a few hundreds of milliseconds, resulting in a neutron star or a black hole. At this stage, neutrinos and anti-neutrinos from all flavors are created through weak interactions between electrons and anti-electrons (reaction 1.3 and Fig 4 part 4). As a result, a neutrino flux is emitted with all flavors from energies in the range of a few MeV [26].

$$e^- + e^+ \rightarrow \nu_\alpha + \overline{\nu}_\alpha, \qquad \text{where } \alpha = e, \mu, \tau, \tag{1.3}$$

During the matter accretion phase by the proto-neutron star, the dense object

enters the Kelvin-Helmholtz cooling phase emitting neutrinos and antineutrinos from all flavors by nucleon-nucleon *bremsstrahlung*. At the same time, the URCA and modified URCA processes drives the production of electron neutrinos for a few seconds [28]. While the star cools down by neutrino emissions, the neutrinos from the neutrinosphere[3] deposit energy in the top cooler layers by neutrino-neutron interactions (reaction 1.4) and inverse beta decay (reaction 1.5), reducing the average energy of electron neutrinos and antineutrinos compared to muon and tau neutrinos/antineutrinos. This drives an mass-loss from the surface of the proto-neutron star with a rate of $10^{-2} M_{\odot}/s$, the so-called neutrinodriven wind.

$$\nu_e + n \rightarrow p + e^-, \tag{1.4}$$

$$\overline{\nu}_e + p \rightarrow n + e^+. \tag{1.5}$$

After the proto-neutron star cools down and the accretion of matter reaches the end, a neutron star or a black hole is left from the progenitor star (Fig 4 part 5), and the ejected matter forms a planetary nebula surrounding the SN reminiscent (Fig 1). If a black hole is formed, than the cooling phase is not present and the accretion is suddenly halted due to the black hole formation. This affects the neutrino flux, causing a sharp cut in the flux emitted [29]. However, in this work we will always work with the full flux, thus we will assume only CCSNs in which a neutron star is left (the largest stellar mass considered is 27 $M_{\odot}$).

[3] The neutrinosphere is the region enclosed by a sphere where the volume encloses the medium that is dense enough for matter to become opaque to neutrinos.

2 Neutrinos

In this chapter we give a brief overview of what are neutrinos and their properties.

> Neutrino physics is largely an art of learning a great deal by observing nothing.
>
> *Haim Harari*

On December 4, 1930, Wolfgang Pauli sent a letter to the radioactive group at the regional meeting in Tübingen, proposing the existence of a yet unseen subatomic particle, that should be emitted along with an electron in the beta decay, in order to "save" the energy conservation[1]. According to his letter, the particle should be neutral in charge, light in mass and have a spin 1/2, he called it the "neutron". But Pauli was not talking about the usual neutron known nowadays to compose atomic nuclei along with the proton, he was talking about what we call today the *neutrino* ("small neutron" in Italian). The name was suggested by Enrico Fermi, after developing a theory for beta decay with the inclusion of this new particle [30]. Later in 1956 the neutrino was finally confirmed experimentally by Clyde Cowan and Frederick Reines [31]. Today, neutrinos are one of the most intriguing particles described by the Standard Model of Particle Physics. Throughout this chapter we will present briefly the description of neutrinos as fundamental particles and their flavor oscillation phenomena.

2.1 But what are neutrinos?

As Pauli put it, neutrinos are elementary[2] spin 1/2 particles that are neutral in electric charge. Furthermore, neutrinos are fermions (Figure 5), meaning that they do not mediate interactions as bosons do, they only take part in them. In fact, the neutrino is the only neutral fermion that we know of until now.

Since neutrinos are neutral, they do not participate in the electromagnetic interaction, and due to the fact that they are leptons, they are also excluded from the strong interaction, leaving them with only the weak force and gravity. As a result of this,

[1] The interested reader may find the copy of the original letter in German at the CERN Document Server.

[2] Pauli did not say anything about neutrinos being elementary particles; this is understood today according to our best experimentally validated model of particle physics. It does not prove that neutrinos are indeed fundamental either, but we stick with the term since they are treated this way in the standard model.

neutrinos interact very rarely with matter. It is commonly said that we need a light-year thick lead wall to stop 50% of neutrinos that come from the sun.

Due to their neutrality, one may ask if neutrinos are their own antiparticles, but the answer for this question is not yet known. Ettore Majorana developed a framework in 1937 where a neutral fermion could be its own antiparticle [32], in contrast to Dirac's framework. However, the true relationship between the neutrino and antineutrino still lacks experimental proof, with many different experiments trying to validate the possible mechanism for distinguishing Dirac and Majorana neutrinos, with as yet no definitive answer [33, 34, 35].

According to the standard model, the Lagrangian of the neutrino is written as

$$\mathcal{L}_\nu = \underbrace{\overline{\psi}_\nu \left(-i\gamma^\mu \partial_\mu\right) \psi_\nu}_{\text{Free propagation}} + \underbrace{\frac{g}{\cos(\theta_W)} \left(I_\nu^3 \overline{\psi}_\nu \gamma^\mu \frac{1-\gamma^5}{2} \psi_\nu \right) Z_\mu}_{\text{Neutral current interactions}} - \underbrace{\frac{g}{\sqrt{2}} \overline{\psi}_l \gamma^\mu \frac{1-\gamma^5}{2} \psi_\nu W_\mu}_{\text{Charged current interactions}}, \quad (2.1)$$

where ψ_ν is the neutrino spinor that solves Dirac equation and ψ_l is the spinor of the associated lepton produced by a charged current interaction, I_ν^3 is the neutrino weak isospin, $\gamma^5 = i\gamma^0\gamma^1\gamma^2\gamma^3$, Z_μ is the vector field of the Z^0 boson and similarly W_μ is the field of the $W^\pm$ boson. Notice however that there is no mass term in the neutrino Lagrangian. That is due to the fact that only neutrinos with left helicity have been observed and thus the standard model assumes no existence of a right-handed neutrino. Since the coupling with the Higgs field is achieved by both helicities, the neutrino, having only left helicity, does not interact with the Higgs field and therefore should not have mass.

2.2 Neutrinos actually have mass

There are three types of neutrinos (Figure 5), each one associated with a corresponding charged lepton, hence their names. Back in 1960s only two types of neutrinos were known. At that time, the now-famous Homestake experiment attempted to measure the flux of neutrinos coming from the sun in order to validate nuclear models for the sun's combustion, known as the Standard Solar Model (SSM). After the first runs, the experiment found a flux between one third and one half of the one predicted by the SSM [36]. At the time, other experiments, SAGE and GALLEX, also performed measurements of the solar neutrino flux. All found discrepancies between the model and the data [37]. Although changes were proposed to the SSM, no reasonable change could explain the data.

However, the solution for this problem had already begun to take shape before the problem itself. In 1957, Bruno Pontecorvo already suggested that some elementary particles could change their flavor in a oscillatory behavior, in analogy to kaon oscillations [38]. This solution was only fully developed in 1985 resulting in the mathematical formalism

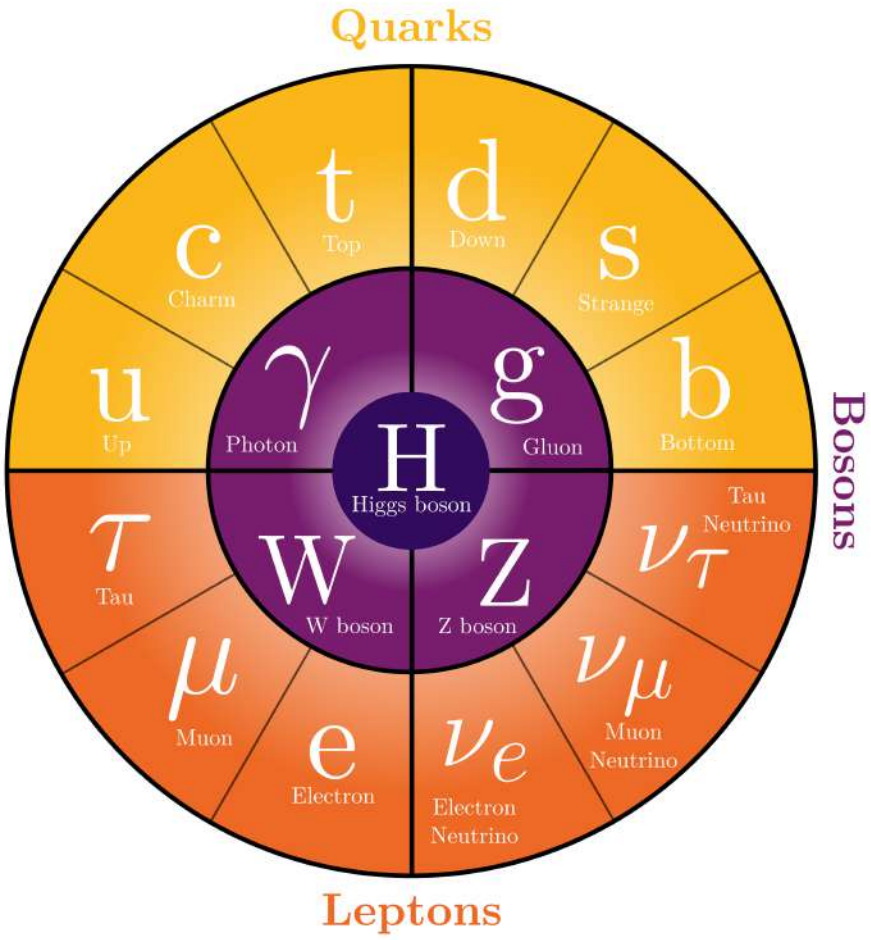

Figure 5 – Standard model of particle physics. Fermions are represented by the outer ring and are subdivided in quarks and leptons. Bosons are represented by the internal ring and are subdivided in the vector bosons such as the photon, gluon and Z/W, and the scalar boson, the Higgs. This diagram is a remake of the one produced by Symmetry Magazine.

of neutrino oscillations and the MSW effect, which will be further described in the next chapter. However the experimental evidence that neutrinos actually changed flavor between their production inside the sun and their detection by Earth's detectors only came in the 90's and early 2000's by the Kamiokande Neutrino Detector and the Sudbury Neutrino Observatory [39, 40]. Today, several ongoing and future experiments aim to study neutrino oscillations as a potential for beyond the standard model physics [41].

Surprisingly, the observation of neutrino oscillations also implied in the existence of a non-zero mass for at least 2 neutrinos. In the standard derivation of neutrino oscillations, we consider a neutrino of flavor $\alpha = e, \mu, \tau$ produced by a charged current interaction alongside a charged lepton or antilepton $l_\alpha^\pm$. We may describe the flavor state of the recently produced neutrino by

$$|\nu_\alpha\rangle = \sum_k U^*_{\alpha k} |\nu_k\rangle , \tag{2.2}$$

where $|\nu_\alpha\rangle$ is the quantum state describing the neutrino's wave function and $U^*_{\alpha k}$ is the element of the Pontecorvo–Maki–Nakagawa–Sakata (PMNS) mixing matrix that relates the flavor states with mass states [42]. Usually this matrix is diagonal i. e. a mass state is the same as a flavor state. However, when the matrix is not diagonal, as is the case for neutrinos, the interaction state is not the same as the propagation state.

$$\begin{aligned} U &= \begin{pmatrix} U_{e1} & U_{e2} & U_{e3} \\ U_{\mu 1} & U_{\mu 2} & U_{\mu 3} \\ U_{\tau 1} & U_{\tau 2} & U_{\tau 3} \end{pmatrix} = \\ &= \begin{pmatrix} c_{12}s_{13} & s_{12}c_{13} & s_{13}e^{-i\delta_{CP}} \\ -s_{12}c_{23} - c_{12}s_{23}s_{13}e^{i\delta_{CP}} & c_{12}c_{23} - s_{12}s_{23}s_{13}e^{i\delta_{CP}} & s_{23}c_{13} \\ s_{12}s_{23} - c_{12}c_{23}s_{13}e^{i\delta_{CP}} & -c_{12}s_{23} - s_{12}c_{23}s_{13}e^{i\delta_{CP}} & c_{23}c_{13} \end{pmatrix}, \end{aligned} \tag{2.3}$$

where s_{ij} denotes $\text{sen}(\theta_{ij})$ and similarly $c_{ij} = \cos(\theta_{ij})$, being θ_{ij} the so-called neutrino mixing angles and δ_{CP} the CP phase violation. In order to ensure that the flavor states are normalized, we must have a normalization for mass states as well

$$\langle \nu_k | \nu_j \rangle = \delta_{kj} \Rightarrow \langle \nu_\alpha | \nu_\beta \rangle = \delta_{\alpha\beta}. \tag{2.4}$$

Since there are three known flavors of neutrinos, the minimum quantity of mass states is three. If more than three mass states exist, that implies the existence of a fourth neutrino that does not interact via weak force, leading to the so-called 3+1 sterile neutrino formulation[3]

The temporal evolution of a flavor state may be described in terms of the temporal evolution of mass states

$$|\nu_\alpha(t)\rangle = \sum_k U^*_{\alpha k} e^{-iE_k t} |\nu_k\rangle . \tag{2.5}$$

Using the unitary relation of the mixing matrix

$$U^\dagger U = 1 \Rightarrow \sum_\alpha U^*_{\alpha k} U_{\alpha j} = \delta_{kj}, \tag{2.6}$$

[3] The curious reader interested in sterille neutrinos may read the recent results from the MicroBooNE experiment [43] and the revision works [44, 45].

we may express the mass state as a flavor state

$$|\nu_k\rangle = \sum_\alpha U_{\alpha k} |\nu_\alpha\rangle . \tag{2.7}$$

Substituting the expression for the temporal evolution of ν_α (2.5), we are left with

$$|\nu_\alpha(t)\rangle = \sum_\beta \left(\sum_k U^*_{\alpha k} e^{-iE_k t} U_{\beta k} \right) |\nu_\beta\rangle . \tag{2.8}$$

That way, a superposition of mass states $|\nu_\alpha\rangle$, which is initially a pure flavor state, becomes a mixed state of superpositions of flavor states, unless U is diagonal. The transition amplitude from the state of flavor α to β is given simply by

$$A_{\nu_\alpha \to \nu_\beta}(t) = \langle \nu_\beta | \nu_\alpha(t) \rangle = \sum_k U^*_{\alpha k} U_{\beta k} e^{-iE_k t}, \tag{2.9}$$

and the probability of detecting a neutrino, that was initially produced in the α flavor state, with flavor β is written as

$$P_{\nu_\alpha \to \nu_\beta}(t) = \left| A_{\nu_\alpha \to \nu_\beta}(t) \right|^2 = \sum_{k,j} U^*_{\alpha k} U_{\beta k} U_{\alpha j} U^*_{\beta j} e^{-i(E_k - E_j)t}. \tag{2.10}$$

In the case of ultra relativistic neutrinos, that is, $v \approx c$[4], we may write the energy of the neutrino in terms of the mass of the corresponding mass states that compose each flavor.

$$E_k \approx E + \frac{m_k^2}{2E} \Rightarrow \tag{2.11}$$

$$\Rightarrow E_k - E_j \approx \frac{\Delta m^2_{jk}}{2E}, \tag{2.12}$$

where $E = |\vec{p}|$ and $\Delta m^2_{jk} = m^2_k - m^2_j$. We may express the transition probability between flavors in terms of the square mass difference between the massive states and the total energy of the neutrino.

[4] It is important not to think of ultra-relativistic as being the same of relativistic. The nomenclature "relativistic" is used when the velocity of a particle is not negligible, compared to the speed of light. A particle with velocity $v = 0.1c$ is an example of a relativistic particle. The term "ultra-relativistic" refers to the case where the particle's velocity is close to the speed of light c, such as $v = 0.99c$, for example.

$$P_{\nu_\alpha \to \nu_\beta}(t) = \sum_{k,j} U^*_{\alpha k} U_{\beta k} U_{\alpha j} U^*_{\beta j} e^{-i\frac{\Delta m^2_{jk}}{2E}t}. \tag{2.13}$$

From the experimental view, it is useful to seek expressing the probability in terms of the distance traveled by the neutrino, instead of the time, $t = vL \approx cL$. In natural units however, $c = 1$, thus $t = L$.

$$P_{\nu_\alpha \to \nu_\beta}(L) = \sum_{k,j} U^*_{\alpha k} U_{\beta k} U_{\alpha j} U^*_{\beta j} \exp\left(-i\frac{\Delta m^2_{jk} L}{2E}\right). \tag{2.14}$$

In the case of antineutrinos, we exchange the elements of the mixing matrix, once the relation between an antineutrino flavor state α and its k mass states is

$$|\overline{\nu}_\alpha\rangle = \sum_k U_{\alpha k} |\overline{\nu}_k\rangle. \tag{2.15}$$

Therefore, the transition probability for antineutrinos is given by

$$P_{\overline{\nu}_\alpha \to \overline{\nu}_\beta}(L) = \sum_{k,j} U^*_{\alpha k} U_{\beta k} U_{\alpha j} U^*_{\beta j} \exp\left(-i\frac{\Delta m^2_{jk} L}{2E}\right). \tag{2.16}$$

Note that the oscillation amplitude depends on the matrix element of the PMNS mixing matrix, which is constant. The oscillation frequency depends on the square mass difference between neutrino mass states. Both of these dependencies may be extracted in neutrino oscillation experiments. As shown in (2.3), the PMNS matrix is fully described by three mixing angles and a phase. The mixing angles θ are measured to be, as of November 2022[5]

$$\begin{aligned}
\theta_{12} &= 33.41^{\circ\,+0.75^\circ}_{\quad -0.72^\circ}, \\
\theta_{13} &= 8.54^{\circ\,+0.11^\circ}_{\quad -0.12^\circ}, \\
\theta_{23} &= 49.1^{\circ\,+1.0^\circ}_{\quad -1.3^\circ}, \\
\delta_{CP} &= 197^{\circ\,+42^\circ}_{\quad -25^\circ},
\end{aligned}$$

while the square mass differences are given by the Particle Data Group to be [47]

[5] These values were extracted from the best-fit in NuFIT.org assuming normal mass hierarchy. These best-fit points were the ones used in all numerical simulations. The CP phase was recently measured by the T2K experiment to be $\delta_{CP} = -112.9^{\circ\,+55.6^\circ}_{\quad -40.1^\circ}$ at the 90% confidence level [46].

$$\Delta m^2_{12} = \Delta m^2_{\text{sol}} = (0.753 \pm 0.018) \times 10^{-4}\ \text{eV}^2,$$
$$\Delta m^2_{13} = \Delta m^2_{32} = \Delta m^2_{\text{atm}} = (2.44 \pm 0.06) \times 10^{-3}\ \text{eV}^2.$$

Thus, the observation of neutrino oscillations is implied by the non-diagonal character of U and in the non-zero square mass difference Δm^2_{jk}. A more realistic description of neutrino oscillations must take into consideration the locality of the production and detection events of neutrinos. As seen in introductory books to quantum mechanics, real particles are described by a superpostion of plane waves known as wave package [48].

This approach yields an oscillation probability given by

$$P_{\nu_\alpha \to \nu_\beta}(L) = \sum_{k,j} U^*_{\alpha k} U_{\beta k} U_{\alpha j} U^*_{\beta j} \exp\left[-2\pi i \frac{L}{L^{\text{osc}}_{kj}} - \left(\frac{L}{L^{\text{coh}}_{kj}}\right)^2 - 2\pi^2 \left(1 - \frac{\vec{L}\cdot\vec{\xi}}{L}\right)^2 \left(\frac{\sigma_x^2}{L^{\text{osc}}_{kj}}\right)^2 \right], \tag{2.17}$$

where $L^{\text{osc}}_{kj} = 4\pi E/\Delta m^2_{kj}$ is the oscillation distance and $L^{\text{coh}}_{kj} = 4\sqrt{2}E^2\sigma_x/|\Delta m^2_{kj}|$ is the coherence distance. In the limit where the effects of the wave package are negligible, for $L \ll L^{\text{coh}}_{kj}$ and $\sigma_x \ll L^{\text{osc}}_{kj}$, the oscillation probability returns to the usual probability given by the standard derivation.

It is worthy while to discuss the physical meaning of the coherence and locality term. The locality term suppresses the oscillation if $\sigma_x \geqslant L^{\text{osc}}_{kj}$. That means that, in order to observe flavor oscillation between the k and j components of massive neutrinos, the production and detection processes need to be located in space separated by a distance smaller than L^{osc}_{kj}. In practice this term tells us that the bigger the neutrino energy, the farther away from the font the detector needs to be. As discussed in [49], this term is what differs oscillation experiments from mass measurement experiments through conservation of momentum in neutrino generation processes. In the limit where interference occurs, the locality term may be ignored. In this case the transition probability equation becomes

$$P_{\nu_\alpha \to \nu_\beta}(L) = \sum_{k,j} U^*_{\alpha k} U_{\beta k} U_{\alpha j} U^*_{\beta j} \exp\left[-2\pi i \frac{L}{L^{\text{osc}}_{kj}} - \left(\frac{L}{L^{\text{coh}}_{kj}}\right)^2 \right]. \tag{2.18}$$

For distances grater than $L \gg L^{\text{coh}}_{kj}$, the coherence suppresses the oscillation (Figure 6). From this distance, the separation of wave packages between massive neutrinos prevents interference and thus, the oscillation [50]. In this situation, only one of the mass states contributes to the detection processes. If the distance is smaller than the coherence term, this term is also negligible and the expression assumes the usual form.

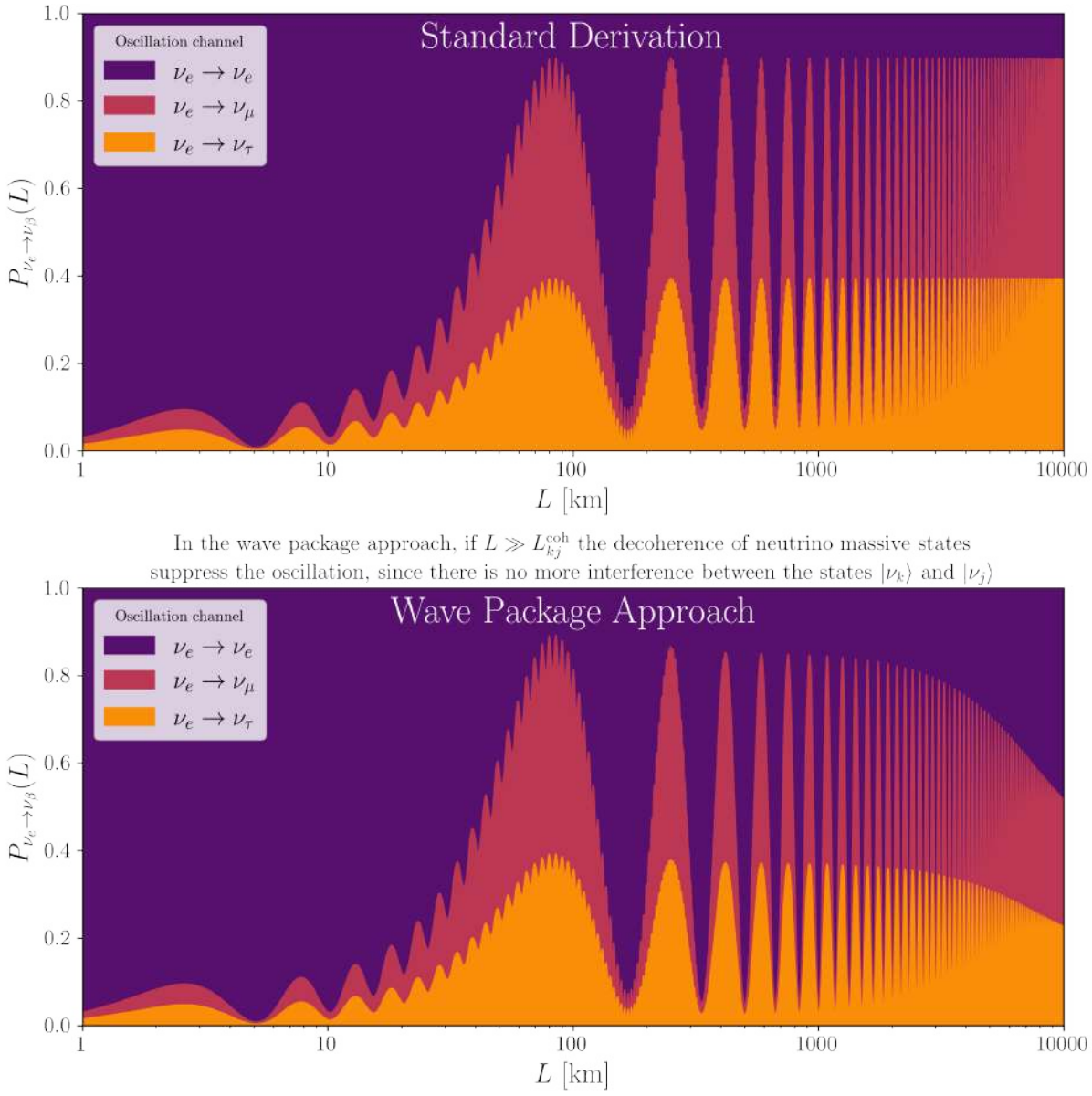

Figure 6 – *Top*: Oscillation probability for an electron neutrino produced with an energy of 10 MeV. The vertical size of each color at a given distance represents the transition probability. *Bottom*: Same as situation, but considering the decoherence term in (2.18). The oscillation probability is suppressed for distances $L \gg L_{kj}^{\text{coh}}$.

The wave package treatment is necessary in order to derive the oscillation probability with a consistent quantum theory, that needs to take into account the locality of creation and detection of particles, associated with momentum and position uncertainties. In practice the wave package treatment may be neglected in oscillation experiments where $L \ll L_{jk}^{\text{coh}}$ or those that don't have enough resolution to differentiate the probability amplitudes of the detection and production processes [50]. The necessity of wave package treatments is also necessary to realistic describe phenomena in which interference is present, such as neutron interferometry [51].

However, vacuum oscillation is not the reason for the results observed by the Homestake experiment. In the core of the sun, as well as in the core of supernovae, neutrinos are produced in coherent mass eigenstates. Thus no oscillation should take place and the flavor partition of the neutrino flux should be the same between production and detection. But this is not the case, as we will see in the next chapter, neutrinos suffer a flavor transition inside matter, which is the responsible for the true discrepancy. Since solar neutrinos are not the objective of this work, we will now focus exclusively on supernova neutrinos, but the curious reader that wishes to dive deeper into solar neutrino physics may read [52, 53].

3 Neutrino Oscillations in Matter

Here the effects present during the neutrino emission from the supernova that determine the final neutrino spectrum are discussed.

I have done a terrible thing: I have postulated a particle that cannot be detected.

I have done a terrible thing: I have postulated a particle that cannot be detected.

Wolfgang Pauli

Contrary to other fundamental particles, neutrinos produced in a flavor α, such as an electron neutrino, may be later detected in a flavor $\beta \neq \alpha$, such as a muon neutrino. This flavor oscillation effect was first proposed by Bruno Pontecorvo in 1957 [38] and first evidenced in the late 60's by the Homestake experiment [54]. However, flavor oscillations were only experimentally confirmed between the end of the 90's and early 2000's by the Kamiokande Neutrino Detector and the Sudbury Neutrino Observatory [39, 40] using data from atmospheric and solar neutrinos. Today, several ongoing and future experiments aim to study neutrino oscillations as a potential for beyond the standard model physics [41].

As discussed in the previous chapter, during the stellar collapse, neutrinos are continuously produced, carrying away most of the energy from the process as they escape the collapsing star. In this chapter we discuss how the effects of stellar matter affect the produced spectra and fluxes of neutrinos from the supernova.

3.1 Neutrino Production Stages

Three main phases characterize neutrino production on a supernova. During the core compression phase, electron capture and photo-desintegration of iron drives the production of electron neutrinos, which initially escape the dying star, but then get trapped as the density of the core increases to the point in which neutrinos are coupled with matter. Shortly after the core-bounce, the density drops and those neutrinos quickly escape the supernova environment, in a phase called ν_e-burst or neutronization burst (Fig 7). At this stage, a peak in electron neutrino luminosity is observed[1] Right after this process, while matter is accreted to the proto-neutron star nucleon-nucleon *bremsstrahlung* and the URCA process drives the production of neutrinos from all flavors and electron neutrinos,

[1] Here luminosity stands for the total energy in neutrinos produced per unit of time.

respectively. This process continues and than decreases as the neutron star is cooled, or is abruptly stopped if a black hole is formed (See ref [55] for a simulation of neutrino emission from a supernova resulting in a black hole).

At all time, the produced neutrino flux may be parameterized by a pinched Fermi-Dirac distribution on energy [25]

$$\mathcal{F}^0_\beta(E,t) = \frac{\mathrm{d}N_\beta(t)}{\mathrm{d}E} = \frac{L_\beta(t)(1+\alpha_\beta(t))^{1+\alpha_\beta(t)}}{\Gamma(1+\alpha_\beta(t))\left\langle E_\beta(t)\right\rangle^{2+\alpha_\beta(t)}} E^{\alpha_\beta(t)} \exp\left(-\frac{(\alpha_\beta(t)+1)E}{\left\langle E_\beta(t)\right\rangle}\right), \tag{3.1}$$

where $\beta = e, \mu, \tau$ is the neutrino flavor, L_β is the luminosity of the flavor β, $\langle E_\beta \rangle$ is the average energy of a neutrino of flavor β, α_β is the pinching parameter and the superscript 0 means that this is the flux produced at the supernova. The pinching parameter arises from the dependency of the neutrinosphere radius with neutrino energy, i.e. the volume that encloses the region where neutrinos are trapped inside matter varies with neutrino energies, this leads to a pinch on both tails of a perfect Fermi-Dirac distribution. A Fermi-Dirac distribution with zero chemical potential is achieved when $\alpha \approx 2.3$, while a Maxwell-Boltzmann distribution is found if $\alpha = 2$. Figure 7 shows how the luminosity L and the average energy $\langle E \rangle$ changes for each neutrino flavor during each stage according to hydrodynamical simulations of supernovae, the non-electron flavors $\nu_\mu, \nu_\tau, \overline{\nu}_\mu$ and $\overline{\nu}_\tau$ are all condensed under the same flavor index x.

The pinching parameter may be computed from the statistical moments of the energy spectrum, $\langle E \rangle$ and $\langle E^2 \rangle$

$$\frac{\langle E^2\rangle}{\langle E\rangle^2} = \frac{2+\alpha}{1+\alpha} \quad \Rightarrow \quad \alpha = \frac{2\langle E\rangle^2 - \langle E^2\rangle}{\langle E^2\rangle - \langle E\rangle^2}. \tag{3.2}$$

However, during all phases, neutrinos must travel through high densities of stellar matter in order to escape the supernova environment. Due to the high density, electron neutrinos interact with electrons in the medium through charged-current foward coherent scattering [56, 57], due to an effective matter potential field for neutrino interactions. This field changes the energy levels of the neutrino mass eigenstates, provoking subsequent changes in the dynamics of neutrino flavor oscillation, thus the neutrino flux emitted from the supernova is different from the neutrino flux produced.

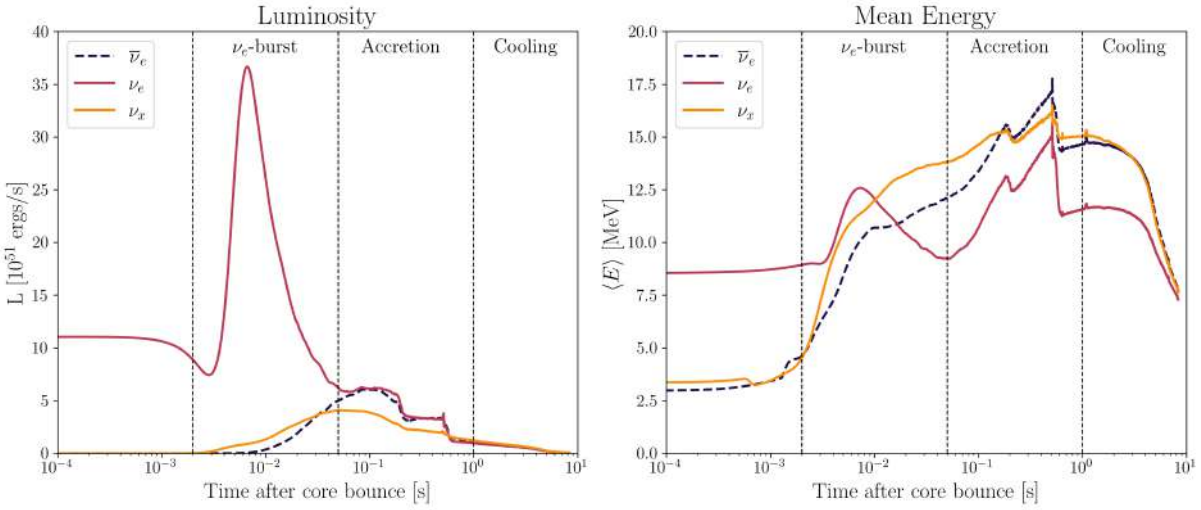

Figure 7 – Neutrino signal in a core collapse supernova. Progenitor star mass $M = 27M_{\odot}$. The *left panel* shows the luminosity in 10^{51} ergs/s during the three main stages after core bounce. The transition of stellar density from opaque to transparent, leading to the burst of electron neutrinos, initially trapped, from electron capture (ν_e-burst) The subsequent accretion of matter by the proto-neutron star (PNS) remanescent (Accretion) and the final PNS cooling phase (Cooling). The *right panel* shows the same stages for the mean energy of each neutrino flavor. Simulations performed by the Garching Group [3].

3.2 Mikheyev–Smirnov–Wolfenstein Effect

Already in 1978, Wolfenstein showed theoretically that under the presence of matter, neutrinos suffer a phenomena analogous to refraction by light photons. The coherent scattering with particles in the medium induces an effective potential that changes the mixing angle between neutrino flavors (see diagram below) [56]. Later in 1985, Mikheyev and Smirnov found that if the matter density changes as the neutrino moves through it, it is possible to obtain a resonance on flavor transition [58]. This matter effect is since then known as Mikeyev-Smirnov-Wolfestein (MSW) effect, and it successfully explained the flavor conversion between neutrinos from the Sun to Earth during the time of the solar neutrino problem[2].

[2] The curious reader may found more information about the solar neutrino problem in [59].

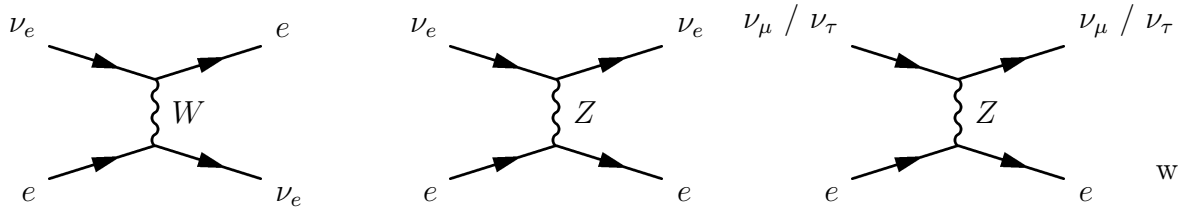

Figure 8 – Neutrino coherent forward scattering channels. From left to right: Electron neutrino charged-current interaction with the exchange of a W boson, electron neutrino neutral-current interaction via exchange of a Z boson and non electron neutrino neutral-current interaction via exchange of a Z boson.

On the scenario of three neutrino flavors, the time evolution of a flavor state is described in terms of an effective potential introduced by the presence of matter in the medium

$$
\begin{aligned}
& i\frac{\mathrm{d}}{\mathrm{d}t}\left|\nu_\alpha\right\rangle = H_{\alpha\beta}(t)\left|\nu_\beta\right\rangle \Rightarrow \\
& \Rightarrow H(t) = \underbrace{\frac{1}{2E}\begin{pmatrix} m^2_{ee} & m^2_{e\mu} & m^2_{e\tau} \\ m^2_{\mu e} & m^2_{\mu\mu} & m^2_{\mu\tau} \\ m^2_{\tau e} & m^2_{\tau\mu} & m^2_{\tau\tau} \end{pmatrix}}_{\text{Vacuum}} + \overbrace{2EA(t)}^{\text{Matter}},
\end{aligned}
\tag{3.3}
$$

where each $m^2_{\alpha\beta}$ is the squared mass difference between flavor eigenstates[3], and $A(t)$ is the matter potential matrix, given by

$$
A(t) = \begin{pmatrix} \sqrt{2}G_F N_e(t) & 0 & 0 \\ 0 & 0 & 0 \\ 0 & 0 & 0 \end{pmatrix}. \tag{3.4}
$$

Since only the electron neutrino element suffers the effect of matter potential, we may rotate the $\mu-\tau$ submatrix without provoking any change in the physics, diagonalizing this submatrix and going from the flavor state $(\nu_e, \nu_\mu, \nu_\tau)$ to $(\nu_e, \nu_{\mu'}, \nu_{\tau'})$ [60]. On this new basis, the Hamiltonian assumes the form

$$
H(t) = \frac{1}{2E}\begin{pmatrix} m^2_{ee} + 2E\sqrt{2}G_F N_e(t) & m^2_{e\mu'} & m^2_{e\tau'} \\ m^2_{\mu' e} & m^2_{\mu'\mu'} & 0 \\ m^2_{\tau' e} & 0 & m^2_{\tau'\tau'} \end{pmatrix}. \tag{3.5}
$$

[3] Here we choose not to use the common notation for squared mass difference in order to avoid the possible confusion with the squared mass difference in mass eigenstates $\Delta m^2_{\alpha\beta} \neq \Delta m^2_{ij}$.

If $N_e \gg \Delta m_{ij}/2E$, than the off diagonal terms may be neglected and the Hamiltonian is fully diagonal $\mathcal{H} \approx \text{Diag}\left(A, m^2_{\mu'\mu'}, m^2_{\tau'\tau'}\right)$. It is important to notice that a potential for μ and τ flavors appear in second order interactions [61]

$$A_{\mu\tau} = A\frac{3G_F m_\tau^2}{2\sqrt{2}\pi^2 Y_e}\left[\ln\left(\frac{m_W^2}{m_\tau^2}\right) - 1 + \frac{Y_n}{3}\right] \approx 10^{-4}A, \tag{3.6}$$

where m_τ is the mass of the tau lepton, m_W is the mass of the W boson, Y_e and Y_n are electron and neutron densities per nucleon. At very high densities, such as inside the neutrinosphere[4] $A_{\mu\tau} \approx \Delta m^2_{\text{atm}}/2E \approx 2m^2_{\mu\tau}/2E$ and the Hamiltonian assumes the diagonal form $H = \text{Diag}\,(A, 0, A_{\mu\tau})$. The effect of this form is that at very high densities, the flavor states coincides with the matter eigenstates in the medium; as a result, neutrinos are produced coherently inside the stellar nucleus and only undergo flavor oscillation when traveling to lower density regions.

The conversion probabilities therefore depend on the electron density of matter N_e as neutrinos travel. In the effective potential, only the first term in the diagonal is non zero once charged-current interactions with μ and τ require much higher energies and are much rarer; as a result mainly electron neutrinos feel the matter potential.

We start the description of neutrino oscillations in matter initially supposing a two neutrino scenario. This scenario presents a reasonable description of the phenomena since only the $\nu_e \leftrightarrow \nu_\mu, \nu_\tau$ transitions are affected by the presence of matter, while $\nu_\mu \leftrightarrow \nu_\tau$ transitions remain unchanged. Moreover, μ and τ neutrinos are indistinguishable in the supernova environment, as a consequence only elements of the mixing of electron neutrinos determine neutrino oscillation effects in supernovae.

3.2.1 2 flavor scenario

In the presence of interactions with matter, the temporal evolution of neutrino wave functions is given by [62]

$$i\frac{\mathrm{d}}{\mathrm{d}t}\begin{pmatrix}\nu_e\\ \nu_\mu\end{pmatrix} = \begin{pmatrix}-\dfrac{\Delta m^2}{4E}\cos(2\theta) + \sqrt{2}G_F N_e & \dfrac{\Delta m^2}{4E}\text{sen}(2\theta)\\ \dfrac{\Delta m^2}{4E}\text{sen}(2\theta) & \dfrac{\Delta m^2}{4E}\cos(2\theta)\end{pmatrix}\begin{pmatrix}\nu_e\\ \nu_\mu\end{pmatrix}. \tag{3.7}$$

This Hamiltonian may be diagonalized, introducing the matter mixing angles $\tilde{\theta}$ in analogy to a two neutrino vacuum scenario

[4] The neutrinosphere is the volume of the star where neutrinos are coupled with matter, that is, the matter is opaque to neutrinos.

$$\begin{pmatrix} \nu_e \\ \nu_\mu \end{pmatrix} = \begin{pmatrix} \cos(\tilde{\theta}) & \text{sen}(\tilde{\theta}) \\ \text{sen}(\tilde{\theta}) & \cos(\tilde{\theta}) \end{pmatrix} \begin{pmatrix} \tilde{\nu}_1 \\ \tilde{\nu}_2 \end{pmatrix}, \tag{3.8}$$

where, $\tilde{\nu}$ is the energy eigenstate in matter and the cosines and sines of $\tilde{\theta}$ are given by

$$\cos(2\tilde{\theta}) = \frac{-A/\Delta m^2 + \cos(2\theta)}{\sqrt{[A/\Delta m^2 - \cos(2\theta)]^2 + \text{sen}^2(2\theta)}}, \tag{3.9}$$

$$\text{sen}(2\tilde{\theta}) = \frac{\text{sen}(2\theta)}{\sqrt{[A/\Delta m^2 - \cos(2\theta)]^2 + \text{sen}^2(2\theta)}}, \tag{3.10}$$

being $A = 2\sqrt{2}EG_FN_e$. With the matrix diagonalized, we find the mass eigenstates to be

$$\tilde{m}^2_{1,2} = \frac{A}{2} \mp \frac{1}{2}\sqrt{[A - \Delta m^2 \cos(2\theta)]^2 + (\Delta m^2)^2 \text{sen}^2(2\theta)}. \tag{3.11}$$

This solution implies on a eigenvalue crossing, or resonance, at the point where $A/\Delta^2_m = \cos(2\theta)$ (Figura 9). This implies the existence of a flavor transition resonance in the region where the electron density of matter reaches

$$N_{\text{crit}} = \frac{\Delta m^2}{2E\sqrt{2}G_F} \cos(2\theta). \tag{3.12}$$

If a ν_e is produced in the region where $N_e > N_{\text{crit}}$ and propagates through matter to the region where $N_e < N_{\text{crit}}$ (as we will see, this is the case of supernovae), than it is fully converted in a ν_μ, given a sufficiently smooth electron density change, i. e. a adiabatic transition. This adiabaticity may be stated as the following relation

$$\delta E \times \delta t \gg \hbar,$$

where the energy gap δE is given by

$$\delta E = \frac{1}{2E}\Delta m^2 \text{sen}(2\theta), \tag{3.13}$$

and the transition time δt is

$$\delta t = \frac{\delta r}{v} \approx \frac{\delta r}{c} = \left(\frac{1}{N_e}\frac{\text{d}N_e}{\text{d}r}\right)^{-1} \frac{\delta N_e}{N_e} = \left(\frac{1}{N_e}\frac{\text{d}N_e}{\text{d}r}\right)^{-1} \frac{\delta A}{A}. \tag{3.14}$$

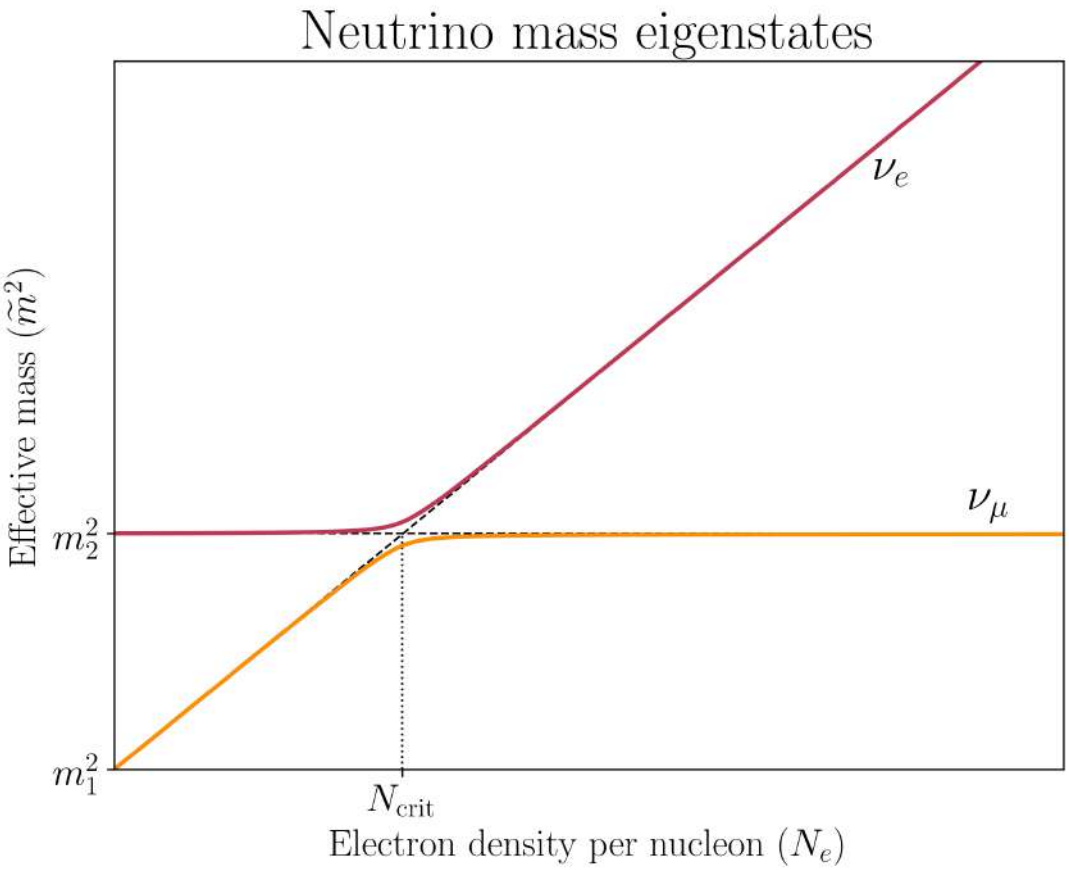

Figure 9 – Effective neutrino mass as a function of N_e. If a ν_e neutrino is produced in the region where $N_e > N_{\text{crit}}$ and propagates to the region $N_e < N_{\text{crit}}$, the state follows the superior path (red wine) and the states ν_e fully convert into ν_μ, supposing that the change in N_e is subtle enough so that the transition occurs adiabaticaly.

Since the resonance happens at $A = \Delta m^2 \cos(2\theta)$ and its width is $\delta A \approx \Delta m^2 \text{sen}(2\theta)$, we observe that the adiabaticity is satisfied if

$$\frac{1}{N_e}\frac{\mathrm{d}N_e}{\mathrm{d}r} \ll \frac{\Delta m^2}{2E}\frac{\text{sen}^2(2\theta)}{\cos(2\theta)}. \tag{3.15}$$

In a three neutrino scenario, we have two terms of the type Δm^2, giving rise to two resonance regions. The survival probability $\nu_e \to \nu_e$ is computed by taking the average over the time-varying part

$$\begin{aligned} P_{\nu_e \to \nu_e} &= \text{sen}^2(\theta)\text{sen}^2(\widetilde{\theta}) + \cos^2(\theta)\cos^2(\widetilde{\theta}) = \\ &= \frac{1}{2}[1 + \cos(2\theta)\cos(2\widetilde{\theta})], \end{aligned} \tag{3.16}$$

where $\widetilde{\theta}$ is the mixing angle at the initial position. However, if the adiabatic condition is

not satisfied, there is a transition probability between the upper eigenstate to the lower eigenstate that is given by [63, 64, 65]

$$P_f = e^{-\frac{\pi}{2}\gamma} = \exp\left[-\frac{\pi}{2}\frac{\Delta m^2 \text{sen}^2(2\theta) N_e}{2E\cos(2\theta)(\text{d}N_e/\text{d}r)}\right], \tag{3.17}$$

where the γ factor is the ratio between both sides of inequality (3.15). Taking into account the possibility of non adiabatic transition, the survival probability of an electron neutrino produced and propagating through matter is given by

$$\begin{aligned} P_{\nu_e\to\nu_e} &= \left[\text{sen}^2(\theta)\text{sen}^2(\widetilde{\theta}) + \cos^2(\theta)\cos^2(\widetilde{\theta})\right](1-P_f) + \\ &+ \left[\text{sen}^2(\theta)\cos^2(\widetilde{\theta}) + \cos^2(\theta)\text{sen}^2(\widetilde{\theta})\right]P_f \\ &= \frac{1}{2} + \left(\frac{1}{2} - P_f\right)\cos(2\theta)\cos(2\widetilde{\theta}). \end{aligned} \tag{3.18}$$

In the limit where $\text{d}N_e/\text{d}r \to 0$, $P_t \to \infty$ and equation (3.18) reduces to (3.16), and in the second limit where $N_e \to 0$, we approach the vacuum solution $A \to 0$ and $\cos(2\widetilde{\theta}) = \cos(2\theta) \Rightarrow P_{\nu_e\to\nu_e} = \frac{1}{2}\left[1+\cos^2(2\theta)\right]$. This solution fits well solar neutrino data and was proposed to solve the solar neutrino problem. Since the whole derivation of (3.18) depends only on θ and Δm^2, measurements of solar ν_e fluxes provides constraints to both $\Delta m^2_\odot$ and θ_{12}.

3.3 Emission Flux

In a supernova, the flavor transition occurs in two resonance layers, each associated with one square mass difference. Where the resonance layer is defined using equation (3.12)

$$\rho_{\text{res}} = \frac{\Delta m^2\cos(2\theta)}{2E\sqrt{2}G_F}\frac{m_N}{Y_e}, \tag{3.19}$$

where m_N is the nucleon mass and Y_e is the electron fraction. The higher density (H) resonance layer is associated with Δm^2_{atm} while de lower density (L) layer is associated with $\Delta m_\odot$. Both regions are outside the core of the collapsing star, therefore the MSW effect does not affect the cooling or the collapse. The transition dynamics in each layer is determined by the adiabaticity parameter γ [66]. For a density profile of the form $\rho = Ar^{-n}$[5] the adiabadicity parameter is given by

[5] Simulations of core collapse supernovae show that a for regions of density $\rho > 1$ g/cm^3 the density profile is well approximated by $\rho \approx Ar^{-3}$ [67, 68].

$$\gamma = \frac{1}{2n}\left(\frac{\Delta m^2}{E}\right)^{1-1/n} \frac{\text{sen}^2(2\theta)}{[\cos(2\theta)]^{1+1/n}} \left(\frac{2\sqrt{2}G_F Y_e A}{m_N}\right)^{1/n}. \tag{3.20}$$

Therefore, the flip probability of neutrino mass eigenstates is written as

$$P_f = \exp\left[-\frac{\pi}{12}\left(\frac{\Delta m^2 \text{sen}^3(2\theta)}{\cos^2(2\theta)E}\right)^{2/3}\left(\frac{2\sqrt{2}G_F Y_e A}{m_N}\right)^{1/3}\right] = \exp\left[-\left(\frac{E_{\text{na}}}{E}\right)^{2/3}\right], \tag{3.21}$$

where E_{na} is a non adiabaticity constant, the lower E_{na}, the higher the flip probability. Higher neutrinos energies E increase the flip probability.

As previously discussed, on a medium with high electron density, the effective neutrino Halmitonian in the medium assumes the form $\mathcal{H} \approx \text{Diag}\left(V, m^2_{\mu'\mu'}, m^2_{\tau'\tau'}\right)$. From this point on, we need to clarify the exact mass hierarchy adopted.

3.3.1 Normal mass hierarchy

If we consider the normal mass hierarchy, where $m_1 > m_2 > m_3$, the neutrino production on the supernova results in $\nu_{\mu'} = \nu_1$, $\nu_{\tau'} = \nu_2$ and $\nu_e = \nu_3$. Thus, the original fluxes coincide with the matter eigenstate fluxes. Since both resonances in the stellar medium act independently, we may write the flavor transition probabilities according to the flavor transition probabilities at both resonance regions, that is, the final flux that is emitted from the supernova depends on the transition probability at the L and H regions (3.17), denoted by P_L and P_H.

Looking at ν_1 first, the probability that $\nu_e = \nu_3$ reaches the surface as ν_1 is simply $P_H P_L$, since this eigenstate has to flip in both resonances. Similarly, the fraction of the original $\nu_{\mu'}$ flux and the other $\nu_2 = \nu_{\tau'}$ flux, which are equal since both neutrinos are only produced in neutral-current interactions, are given by $(1 - P_L)\mathcal{F}^0_x$ and $P_L(1 - P_H)\mathcal{F}^0_x$, respectively. At the surface, the final ν_1 flux is

$$\mathcal{F}_1 = P_H P_L \mathcal{F}^0_e + (1 - P_H P_L)\mathcal{F}^0_x. \tag{3.22}$$

In a similar way, the fluxes of ν_2 and ν_3 that arrive at the stellar surface are

$$\mathcal{F}_2 = (P_H - P_H P_L)\mathcal{F}^0_e + (1 - P_H + P_H P_L)\mathcal{F}^0_x \tag{3.23}$$

$$\mathcal{F}_3 = (1 - P_H)\mathcal{F}^0_e + P_H \mathcal{F}^0_x. \tag{3.24}$$

We may then write the electron neutrino flux emitted from the supernova as

$$\begin{aligned}\mathcal{F}_e &= \left(|U_{e1}|^2 P_H P_L + |U_{e2}|^2 P_H(1-P_L) + |U_{e3}|^2 (1-P_H)\right)\mathcal{F}_e^0 + \\ &+ \left(1 - |U_{e1}|^2 P_H P_L + |U_{e2}|^2 P_H(1-P_L) + |U_{e3}|^2 (1-P_H)\right)\mathcal{F}_x^0 = \\ &= \mathcal{F}_e^0 \sum_i |U_{ei}|^2 a_i + \mathcal{F}_x^0 \left(1 - \sum_i |U_{ei}|^2 a_i\right),\end{aligned} \tag{3.25}$$

where $a_1 = P_H P_L$, $a_2 = P_H(1-P_L)$ and $a_3 = 1 - P_H$. By the conservation of the initial flux $\mathcal{F}_e^0 + 2\mathcal{F}_{\mu,\tau}^0$, the non-electron neutrino flux is simply

$$2\mathcal{F}_{\mu,\tau} = \left(1 - \sum_i |U_{ei}|^2 a_i\right)\mathcal{F}_e^0 + \left(1 + \sum_i |U_{ei}|^2 a_i\right)\mathcal{F}_x^0. \tag{3.26}$$

On the case of normal mass hierarchy, the initial antineutrino fluxes are $\overline{\nu}_1 = \overline{\nu}_e$, $\overline{\nu}_2 = \overline{\nu}_\mu$ and $\overline{\nu}_3 = \overline{\nu}_\tau$. The U_{e3} term in the mixing matrix is suppressed on the medium and therefore $\overline{\nu}_e \to \overline{\nu}_3$ transitions are negligible. In the same way as described for neutrinos, except for the fact that antineutrinos don't participate in the H resonance, the final antineutrino fluxes are

$$\mathcal{F}_{\overline{e}} = \left[|U_{e1}|^2 (1-\overline{P}_L) + |U_{e2}|^2 \overline{P}_L\right]\mathcal{F}_{\overline{e}}^0 + \left[1 - |U_{e1}|^2 (1-\overline{P}_L) - |U_{e2}|^2 \overline{P}_L\right]\mathcal{F}_x^0 \tag{3.27}$$

$$\begin{aligned}2\mathcal{F}_{\overline{\mu},\overline{\tau}} &= \left[1 - |U_{e1}|^2 (1-\overline{P}_L) - |U_{e2}|^2 \overline{P}_L\right]\mathcal{F}_{\overline{e}}^0 + \\ &+ \left[1 + |U_{e1}|^2 (1-\overline{P}_L) + |U_{e2}|^2 \overline{P}_L\right]\mathcal{F}_x^0.\end{aligned} \tag{3.28}$$

Therefore, the final non electron neutrino flux is written as

$$\begin{aligned}4\mathcal{F}_x &= \left(1 - \sum_i |U_{ei}|^2 a_i\right)\mathcal{F}_e^0 + \left[2 + \sum_i |U_{ei}|^2 a_i + |U_{e1}|^2 (1-\overline{P}_L) + |U_{e2}|^2 \overline{P}_L\right]\mathcal{F}_x^0 + \\ &+ \left[1 - |U_{e1}|^2 (1-\overline{P}_L) - |U_{e2}|^2 \overline{P}_L\right]\mathcal{F}_{\overline{e}}^0.\end{aligned} \tag{3.29}$$

If the propagation is completely adiabatic, than $\overline{P}_L = 0$. Calling $p = \sum_i |U_{ei}|^2 a_i$ and $\overline{p} = \left[|U_{e1}|^2 (1-\overline{P}_L) + |U_{e2}|^2 \overline{P}_L\right]$ the electron neutrino survival probability and the electron antineutrino survival probability, respectively, we may rewrite the final fluxes in terms of the initial fluxes in a compact way

$$\begin{pmatrix} \mathcal{F}_e \\ \mathcal{F}_{\overline{e}} \\ 4\mathcal{F}_x \end{pmatrix} = \begin{pmatrix} p & 0 & 1-p \\ 0 & \overline{p} & 1-\overline{p} \\ 1-p & 1-\overline{p} & 2+p+\overline{p} \end{pmatrix} \begin{pmatrix} \mathcal{F}_e^0 \\ \mathcal{F}_{\overline{e}}^0 \\ \mathcal{F}_x^0 \end{pmatrix}. \tag{3.30}$$

Considering an adiabatic propagation for antineutrinos [69], the electron antineutrino survival probability $\overline{p}$ assumes the value $\overline{p} \approx |U_{e1}|^2$. For neutrinos, the L resonance is adiabatic, therefore $P_L \approx 0$ and the electron neutrino survival probability is written as $p \approx |U_{e2}|^2 P_H$. Thus, on the normal mass hierarchy, the final neutrino fluxes emitted from the supernova are[6]

$$\mathcal{F}_e = |U_{e2}|^2 P_H \mathcal{F}_e^0 + (1 - P_H |U_{e2}|^2)\mathcal{F}_x^0 \tag{3.31}$$

$$\mathcal{F}_{\overline{e}} = |U_{e1}|^2 \mathcal{F}_{\overline{e}}^0 + |U_{e2}|^2 \mathcal{F}_x^0 \tag{3.32}$$

$$4\mathcal{F}_x = (1 - |U_{e2}|^2)P_H \mathcal{F}_e^0 + |U_{e2}|^2 \mathcal{F}_{\overline{e}}^0 + (3 - |U_{e2}|^2 + |U_{e2}|^2 P_H)\mathcal{F}_x^0. \tag{3.33}$$

It is worth while to remember that this expression for the electron neutrino survival probability holds only on the scenario where the electron density profile of matter is adiabatic, that is, it does not have sudden changes in matter density. The survival probability depends on the value for $\Delta m^2_{\text{atm}} = \Delta m^2_{32}$ and $|U_{e3}|^2 = \text{sen}^2(\theta_{13})$, considering the CP phase violation to be zero or very small. According to current experimental data, $\Delta m^2_{\text{atm}} = |2.453 \pm 0.033| \times 10^{-3}$ and $|U_{e3}|^2 = (2.18 \pm 0.07) \times 10^{-2}$ [47][7].

3.3.2 Inverted mass hierarchy

Since we do not know the actual mass hierarchy, we now develop the same calculations considering the inverted mass hierarchy scenario, where $m_2 > m_1 > m_3$. With inverted mass hierarchy, the H resonance lies in the antineutrino channel, contrary to the normal mass hierarchy. In the same way as the normal mass hierarchy, we may construct the fluxes in terms of the survival probabilities p and $\overline{p}$. The original neutrino flavors are given by the mass eigenstates as $\nu_1 = \nu_\mu$, $\nu_2 = \nu_e$ and $\nu_3 = \nu_\tau$, while the antineutrino flavor states are $\overline{\nu}_1 = \overline{\nu}_\tau$, $\overline{\nu}_2 = \overline{\nu}_\mu$ and $\overline{\nu}_3 = \overline{\nu}_e$.

The ν_e neutrino crosses the H and L resonances adiabatically, thus the electron neutrino survival probability p is written as

$$p = |U_{e2}|^2 . \tag{3.34}$$

[6] Here I will not take into account decoherence effects or $\nu - \nu$ interactions.

[7] All experimental values related to neutrino physics may be found in https://pdg.lbl.gov/

Now the $\overline{\nu}_e$ neutrino starts as $\overline{\nu}_3$ and may suffer a transition to the $\overline{\nu}_1$ state at the H resonance with probability $\overline{P}_H$ and the crossing of the L resonance is adiabatic, as a result the survival probability for the electron antineutrino is

$$\overline{p} = |U_{e1}|^2 \overline{P}_H + |U_{e3}|^2 (1 - \overline{P}_H). \tag{3.35}$$

The final fluxes emitted from the supernova, in this scenario are

$$\mathcal{F}_e = |U_{e2}|^2 \mathcal{F}_e^0 + |U_{e1}|^2 \mathcal{F}_x^0 \tag{3.36}$$
$$\mathcal{F}_{\overline{e}} = |U_{e1} P_H|^2 \mathcal{F}_{\overline{e}}^0 + (1 - P_H |U_{e2}|^2) \mathcal{F}_x^0 \tag{3.37}$$
$$4\mathcal{F}_x = \mathcal{F}_T^0 - \mathcal{F}_e - \mathcal{F}_{\overline{e}}, \tag{3.38}$$

where $\mathcal{F}_T^0$ refers to the total produced spectrum. Since the total flux emitted and produced is the same, one may only compute the transformations in the electron and antielectron fluxes, and use the constraint $\mathcal{F}_e^0 + \mathcal{F}_{\overline{e}}^0 + 4\mathcal{F}_x^0 = \mathcal{F}_e + \mathcal{F}_{\overline{e}} + 4\mathcal{F}_x = \mathcal{F}_T^0$ to compute $\mathcal{F}_x$.

3.4 Neutrino Oscillation on Earth

Although neutrinos don't oscillate between the supernova and Earth due the fact that neutrinos in high density mediums are created as mass eigenstates, suppressing the oscillation [8], when encountering a flavor non-symmetric matter like Earth, the eigenstates change and flavor oscillation occurs once again. This effect has already been observed in the case of solar neutrinos, provoking a increase in electron neutrinos when they cross Earth before reaching the detector [70]. For water Cherenkov detectors, mainly sensitive to electron antineutrinos like Super-Kamiokande, the sun appears brighter at night. Throughout this work, we will consider an Earth density model with two constant density layers: the mantle extends to 2,888 km in depth, and the core which comprises both the inner and outer cores of Earth, with a radius of 3,483 km.

Due to the distance of the burst and the spherical symmetry of Earth, the length $L_\odot$ of the neutrino trajectories inside Earth can be fully described by the nadir angle of the detector and the supernova[9]. If $-\pi \leqslant \theta_\mathrm{n} \leqslant 0$, than neutrinos do not cross Earth before reaching the detector, however for $\pi > \theta_\mathrm{n} > 0$ neutrinos cross either the mantle of both the mantle and the core of the planet. Due to the spherical symmetry, the problem can be studied considering θ_n varying from 0 to $\pi/2$. The nadir angle depends

[8] Even if neutrinos were created in a coherent state and oscillate, the distance between the supernova and Earth would provoke decoherence of wave packages [49, 50].

[9] Some detectors such as Super/Hyper-Kamiokande use the zenith angle in order to parametrize neutrino direction, the nadir angle can be easly transformed into the zenith angle by making $\theta_\mathrm{z} = \theta_\mathrm{n} + \pi/2$.

of 3 main factors: (1) the location of the supernova, (2) the time of the day at which the detection occurs and (3) the location of the detector on Earth's surface. Figure 15 shows the schematic scenario of a neutrino burst passing through Earth with nadir angle $\theta_{\rm n}$ before reaching the detector. If $\theta_{\rm n} > 56.9^{\circ}$, than the neutrinos will go through both Earth's mantle and the core. The total radius of Earth is $R_{\oplus} = 6{,}731$ km and Earth's outer core radius is $R^{c}_{\oplus} = 3{,}483$ km. The total length of the neutrino path through the planet is given as a function of the nadir angle by

$$L_{\oplus} = R_{\oplus}\sqrt{2[1-\cos(\theta_{\rm n})]} \quad \text{if} \ , \ 90^{\circ} \geqslant \theta_{\rm n} \geqslant 0, \tag{3.39}$$

which has a maximum $L_{\oplus} = 2R_{\oplus}$ when $\theta_{\rm n} = 90^{\circ}$. Due to Earth layer structure (Figure 10), most models divide Earth in two or three constant density layers, usually separating the Mantle and the Core, or the Mantle, the Outer Core and the Inner Core. However, aiming at a more precise description, here we will compute numerically the whole neutrino state time-evolution inside Earth (3.5) using the numerical result of the Preliminary Reference Earth Model (PREM) [71], derived from seismological data. We compute the transition probability from mass eigenstates ν_1, ν_2, ν_3 ($\overline{\nu}_1$, $\overline{\nu}_2$, $\overline{\nu}_3$) into the flavor eigenstates ν_e, ν_μ, ν_τ ($\overline{\nu}_e$, $\overline{\nu}_\mu$, $\overline{\nu}_\tau$) in both normal and inverted hierarchy schemes.

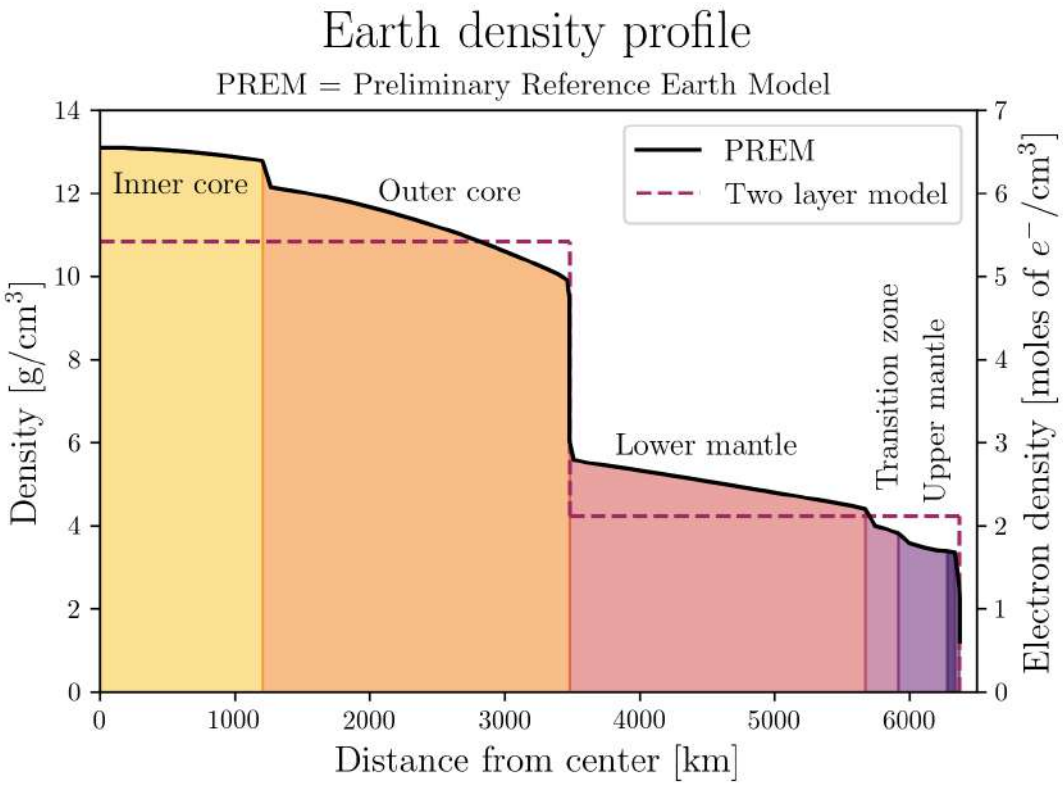

Figure 10 – Earth density profile according to the PREM model. Dashed lines represent the usual two layer model considered in many studies such as [4]. Electron density profile is calculated from the density matter profile.

In order to properly numerically compute the Earth matter effect in neutrino propagation, we compute the matter density profile that a neutrino crosses, given a nadir angle θ_{n} by computing the distance from the center in each point of the neutrino trajectory $L_{\odot}$ using the cosines law

$$d_c = \sqrt{R_{\odot}^2 + l^2 - 2R_{\odot} l \cos(\pi/2 - \theta_{\mathrm{n}}}, \tag{3.40}$$

where l is a given length in $L_{\odot}$, with origin on the neutrino entrance point and d_c is the distance to Earth's center. This allows us to compute the density profile for an arbitrary neutrino nadir angle. Figure 11 shows both the length of the neutrino path through Earth, given by (3.39), and the matter density profile experienced by the neutrino, given by (3.40), with respect to the nadir angle.

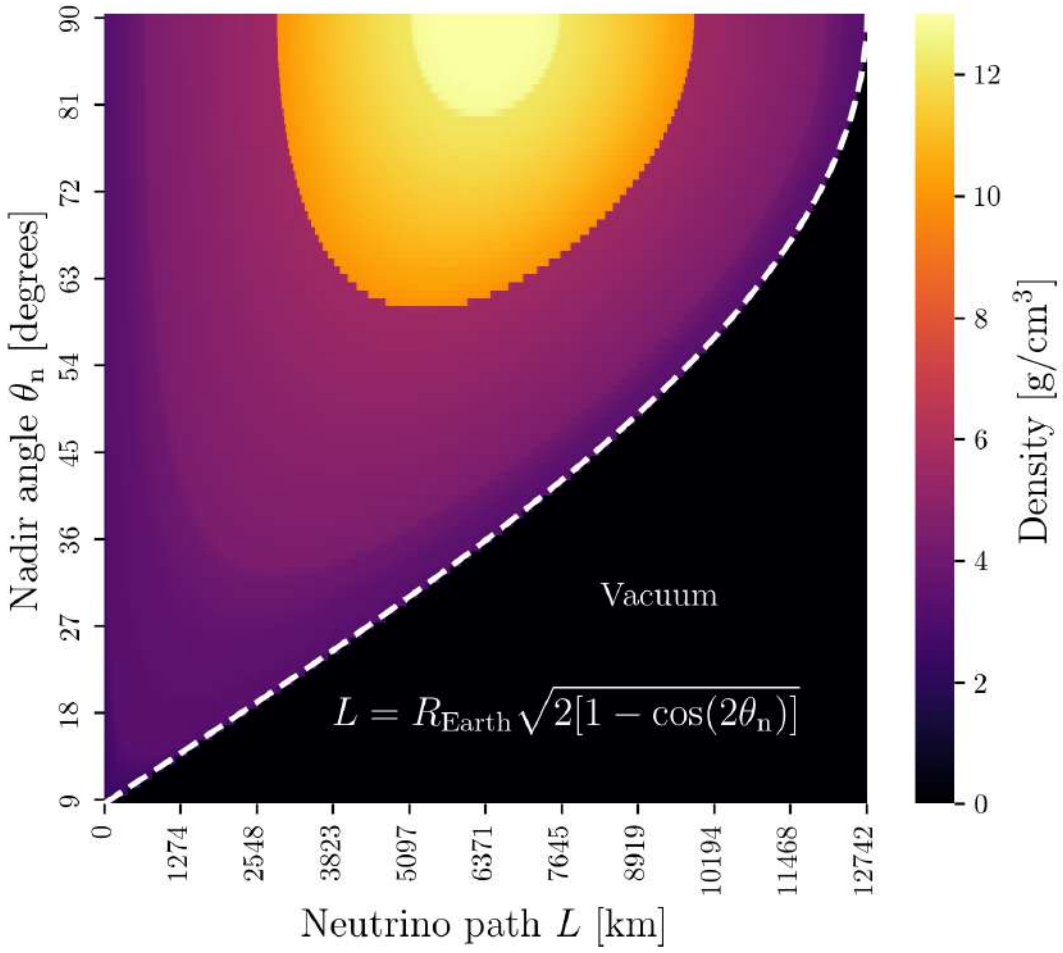

Figure 11 – Relation between neutrino path length, nadir angle and matter density.

Finally, to determine a nadir angle from a supernova location we use the right ascension and declination of a supernova event from the equatorial coordinate systems, and a specific date in which the neutrino is detected. By knowing the right ascension (RA)

and declination (DEC) of a supernova, the geographical coordinates of a given detector on Earth, and the arbitrary date of detection, we can directly compute the nadir angle and thus, the matter density profile (Figure 12). In the arbitrary date and location chosen (the date of writing of this piece of text), we can see that the neutrino comes with a nadir angle of 60.61° with respect to the Super-Kamiokande detector, crossing both Earth's mantle and outer core.

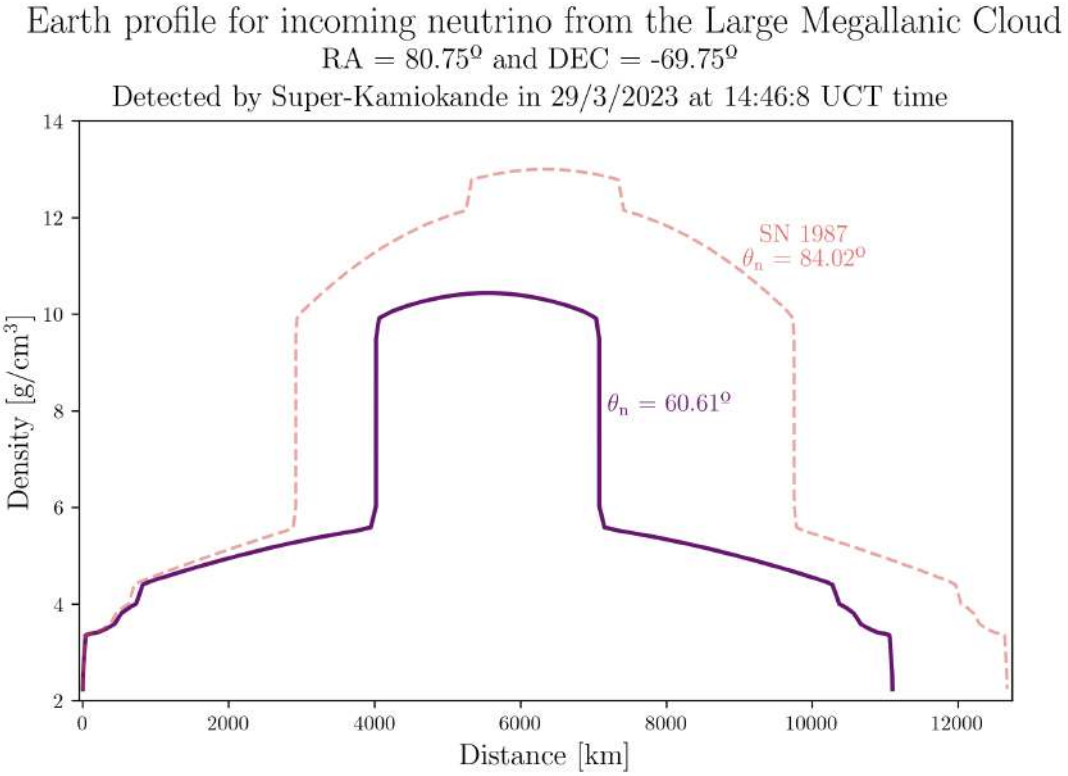

Figure 12 – Matter density profile experienced by a incoming neutrino from an arbitrary date, at the same location as SN1987A, in the Large Megallanic Cloud. The dashed curve shows the matter density profile experienced by neutrinos detected from SN1987A 23-02-1987 at 23:00:00.

Using the results shown in Figure 11 we may compute transition the probabilities $P_{\nu_i \to \nu_e}$, where $i = 1, 2, 3$ for both neutrinos and antineutrinos, in normal and inverted hierarchy. Figures 13 and 14 shows the result of this computation for neutrino energies from 0.5 to 100 MeV and θ_n from 0.9 to 90 degrees. Note that in normal hierarchy $\nu_e = \nu_3$ and $\nu_x = \nu_1 + \nu_2$, that is, the electron neutrino leaves the star as the mass eigenstate 3, while the other flavors μ, τ leave as mass eigenstates 1 and 2, so the total ν_x is the sum $\nu_1 + \nu_2$, similarly $\overline{\nu}_e = \overline{\nu}_1$ and $\overline{\nu}_x = \overline{\nu}_2 + \overline{\nu}_3$. In inverted mass hierarchy $\nu_e = \nu_2$ and $\nu_x = \nu_1 + \nu_3$, and for antineutrinos $\overline{\nu}_e = \overline{\nu}_3$, $\overline{\nu}_x = \overline{\nu}_1 + \overline{\nu}_2$. This means that in normal hierarchy, the electron neutrino spectrum is almost entirely converted in ν_x neutrino spectrum, while electron antineutrinos are partially converted to $\overline{\nu}_x$. In contrast, supposing an inverted mass hierarchy, the electron neutrino is partially converted to ν_x and electron

antineutrinos is almost fully converted to $\overline{\nu}_x$. One may note from figures 13 and 14 that the energy dependence of the transition probability is almost negligible, since the sum $P_{\nu_1 \to \nu_e} + P_{\nu_2 \to \nu_e}$ is almost constant for all energies, despite oscillations in each term and the behavior change when $\theta_{\mathrm{n}} \geqslant 56.9^{\circ}$ due to Earth's core effect.

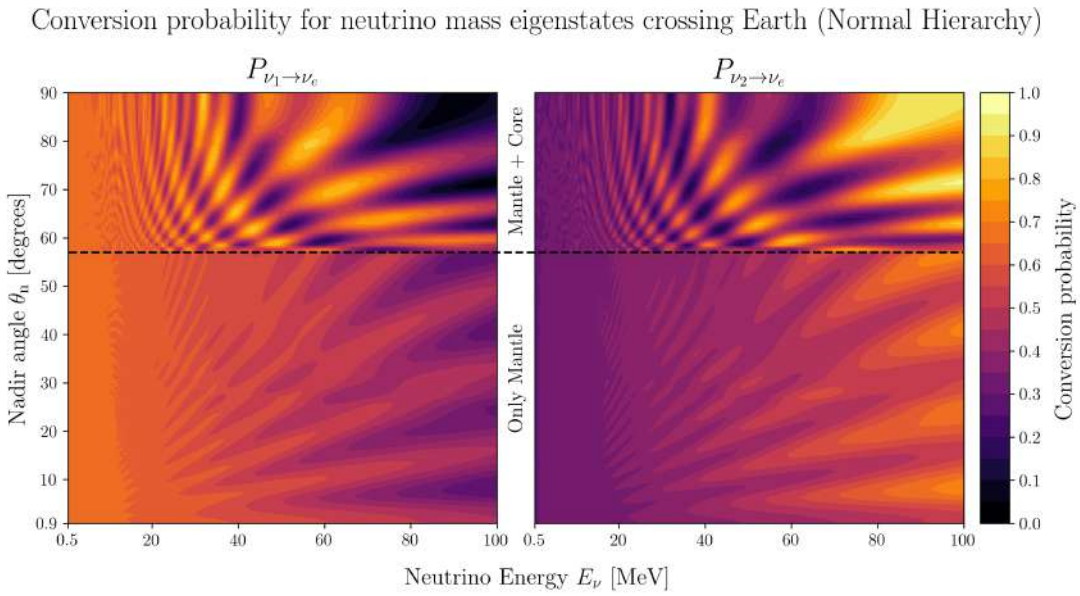

((a))

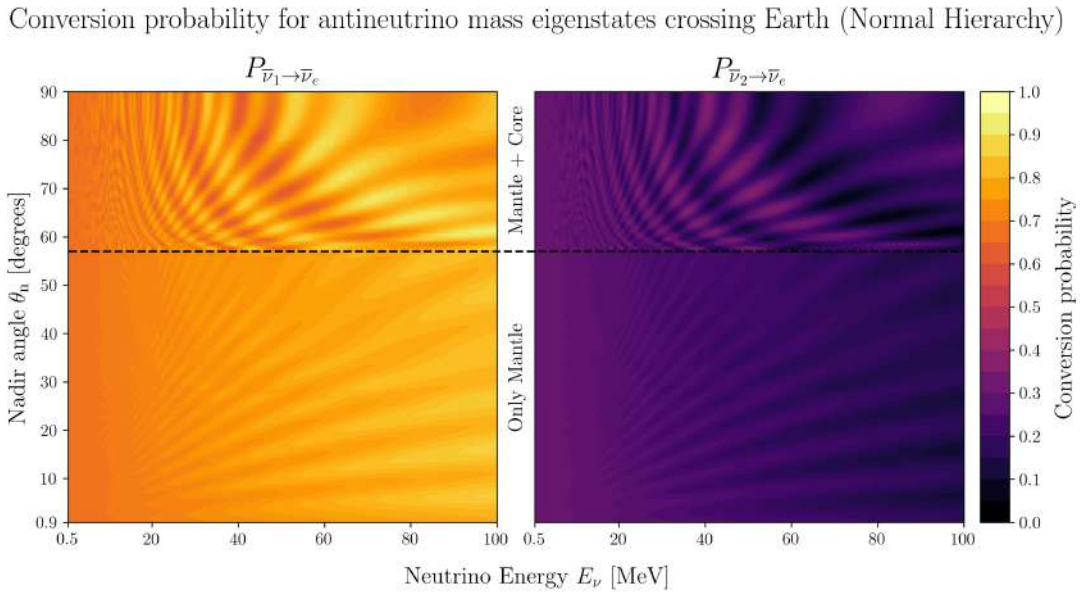

((b))

Figure 13 – Transition probabilities for neutrino (a) and antineutrinos (b) in normal mass hierarchy. A sharp change in oscillatory behavior of the probability is observed when the nadir angle is larger than 56.9° due to the earth core crossing. This scenario supports a two layer treatment of Earth's interior, when studying the matter effect in neutrino oscillations.

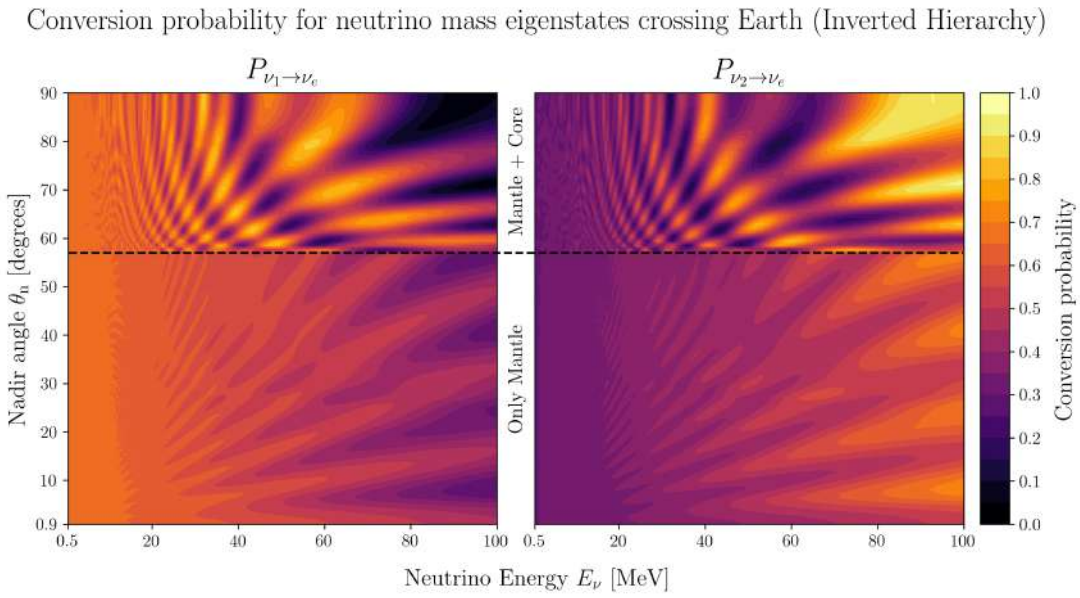

((a))

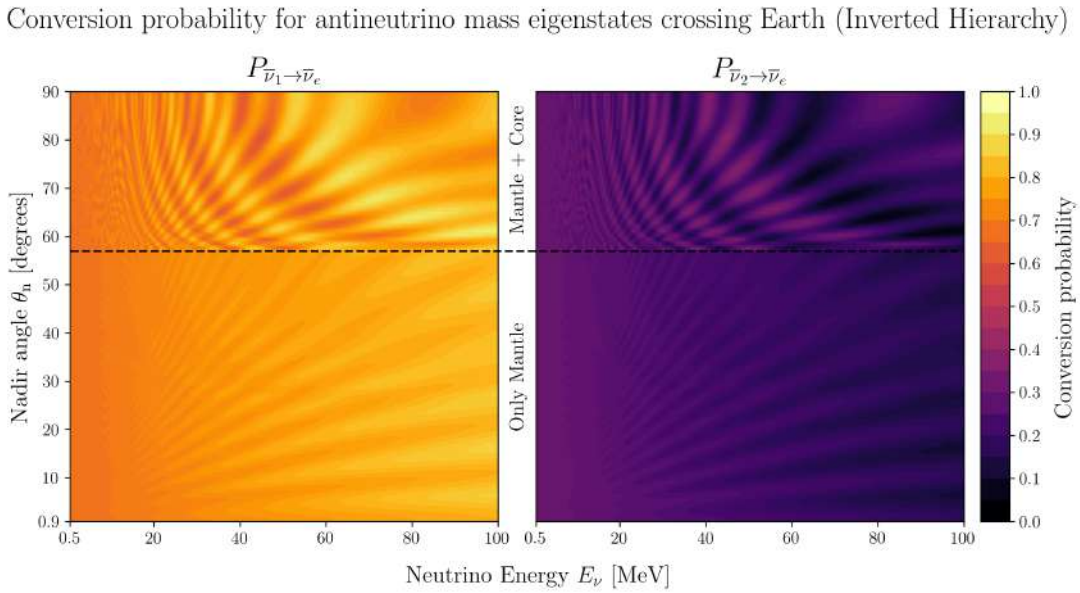

((b))

Figure 14 – Transition probabilities for neutrino (a) and antineutrinos (b) in inverted mass hierarchy. A sharp change in oscillatory behavior of the probability is observed when the nadir angle is larger than 56.9° due to the earth core crossing. This scenario supports a two layer treatment of Earth's interior, when studying the matter effect in neutrino oscillations.

In all simulations, the Earth matter effect is considered using the results from figures 13 and 14. Given a input value for RA and DEC, and a arbitrary input for a detection date, the nadir angle is computed along with the transitions probabilities for all neutrino energies that compose the supernova spectrum, resulting in

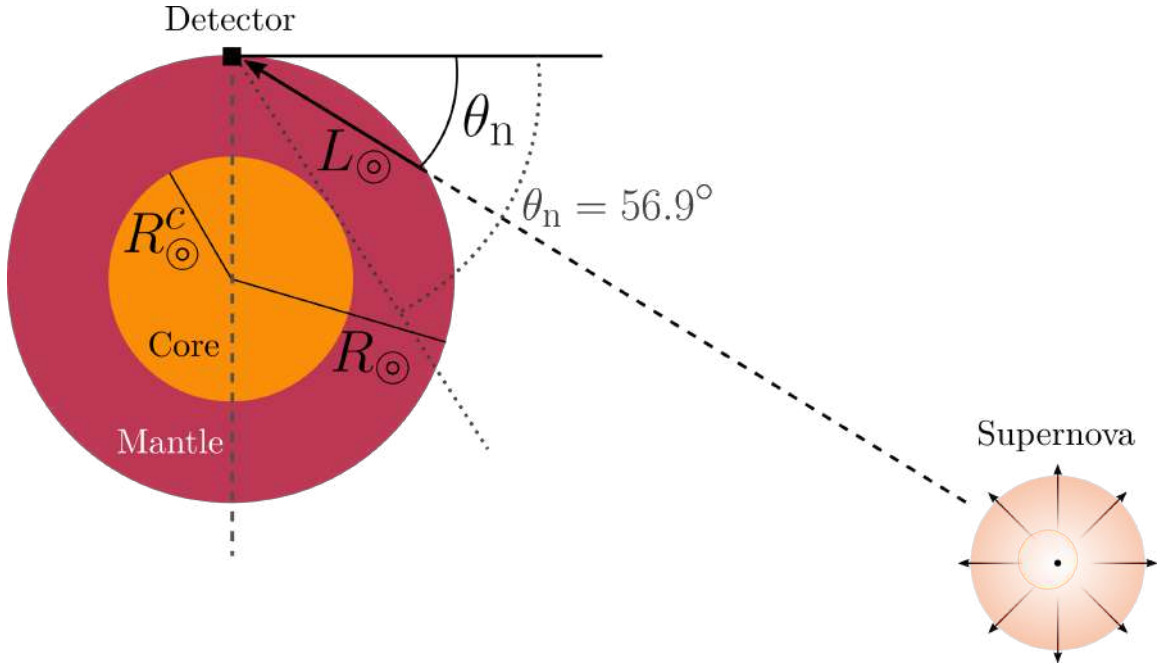

Figure 15 – Earth matter effect in neutrinos from supernovae. Neutrinos might reach a detector with a nadir angle $\theta_{\rm n} > 0$, resulting in a passage through Earth's mantle or mantle + core (if $\theta_{\rm n} > 56.9°$).

$$\mathcal{F}_e^\odot = p^\odot \mathcal{F}_e + (1 - p^\odot)\mathcal{F}_x, \tag{3.41}$$

$$\mathcal{F}_{\bar{e}}^\odot = \overline{p}^\odot \mathcal{F}_{\bar{e}} + (1 - \overline{p}^\odot)\mathcal{F}_x, \tag{3.42}$$

$$\mathcal{F}_x^\odot = \frac{1 - p^\odot}{2}\mathcal{F}_e + \frac{2 + p^\odot + \overline{p}^\odot}{2}\mathcal{F}_x + \frac{1 - \overline{p}^\odot}{2}\mathcal{F}_{\bar{e}}, \tag{3.43}$$

where $p^\odot$ and $\overline{p}^\odot$ are given computing the transition probabilities for mass eigenstates and the electron flavor state shown in figures 13 and 14. One may notice that although Earth's interior is composed of several layers with different densities, the flavor oscillation only changes behavior when the neutrino passes through the core, allowing us to conclude that from the perspective of neutrino flavor oscillations, Earth is like a bi-layer planet, thus many works simplify Earth to a two layer sphere where analytical equations for the probabilities using a sum of sines and cosines are allowed [4, 72].

Part II

Neutrino Detection

4 Neutrino Detectors

This chapter describes the current and next generations of neutrino detectors, as well as their unique features relevant to the detection and the simulations.

> Theoretical and experimental physicists are now studying nothing at all—the vacuum. But that nothingness contains all of being.
>
> *Heinz R. Pagels*

Having the neutrino emission and propagation physics in our hands, it is time to investigate the detection process. The first detection of neutrinos was performed near the Savannah River nuclear reactor in 1956 by Clyde Cowan and Frederick Reines using a scintillation detector [31]. Since then, neutrinos detectors have evolved drastically in their detection ability and methods. Throughout this work, we will study the detection process in four different detectors. The first is part of the current generation of neutrino detectors, the Super-Kamiokande. The other three are all part of the future generation, the Hyper-Kamiokande, DUNE and JUNO.

4.1 Super-Kamiokande

The Super-Kamioka Neutrino Detector (Super-Kamiokande, or Super-K) is a large water Cherenkov detector located 1,000 meters underground in mount Ikeno. Originally designed to search for the proton decay, the detector became a valuable asset in the observation of neutrinos, being crucial in the discovery of neutrino oscillations and providing a solution to the solar neutrino problem [39]. The detection chamber is a cylindrical pool holding 50 ktons of ultrapure water, with a inner detector mass of 32 ktons, surrounded by 13,000 photomultiplier tubes (PMTs) capable of observing Cherenkov photons from charged particles produced as a result of a neutrino interaction.

The use of water as target for neutrino interactions results in some possible interaction channels:

- **Inverse Beta Decay (IBD):** Electron antineutrinos may interact with a proton on a water molecule and convert it into a neutron, releasing a positron that emits Cherenkov radiation, triggering the PMTs. The minimum neutrino energy necessary for this reaction to occur is 1.806 MeV. The outgoing positron energy E_{e^+} distribution has a width $\mathcal{O}(2E_\nu/m_p)$ due to the nucleon recoil which becomes larger than the

detector's resolution for the higher energy tail of the neutrino spectrum; therefore we take in our simulations the total IBD cross-sections that is integrated over the nucleon recoil energy, as shown in [73]. In 2020, 13 tons of gadolinium sulfate octahydrate ($Gd_2(SO_4)_3 \cdot 8H_2O$) were added to the detector pool in order to increase the neutron capture efficiency and distinguish the inverse beta decay channel from other channels that do not result in free neutrons, resulting in a Gd concentration of 111 ± 2 ppm (or 0.02% of the detector mass) [74]. Gd captures neutrons by thermal neutron capture, emitting a γ-ray cascade of energy around 8 MeV, which is captured by PMTs and together with the Cherenkov light signal indicates the IBD interaction. This technique allows a 50% efficiency of neutron tagging, that is, identification of IBD events. Future development will increase the Gd concentration to 0.2% of the detector volume, increasing the neutron tagging efficiency to 90% [75]. Therefore, since this work is concerned with the detection of future supernova events, we assume that neutron tagging will be already on its full capacity of 90% efficiency.

$$\overline{\nu}_e + p \rightarrow n + e^+ \tag{4.1}$$

- **Neutrino-Electron Elastic Scattering (νeES):** In this interaction, a neutrino, or antineutrino, of any flavor exchanges a neutral boson (Z^0) with a valence electron on the water molecule. The electron absorbs some of the neutrino energy, releasing itself from the molecule and moving through the medium emitting Cherenkov radiation. In water, Cherenkov radiation is emitted by an electron if its energy is above 0.26 MeV. Therefore, a neutrino with energy less than 0.26 MeV is not capable of producing a detectable elastic scattering event.

$$\nu + e^- \rightarrow \nu + e^- \tag{4.2}$$

  Here ν denotes a neutrino or antineutrino of any flavor.

- **Neutrino-Nucleus Charged Interaction (ν^{16}OCC):** The third possible interactions involves the exchange of a charged boson ($W^{\pm}$) between the neutrino and the proton (or neutron) inside the oxygen nucleus of water. This process may occur via electron neutrinos (W^+) or antineutrinos (W^-). The exchange of a charged boson by the neutrino results in the production of a charged lepton that travels the medium emitting Cherenkov light. At the end of this interaction, the oxygen nucleus is converted into a fluorine isotope in the case of a neutrino and a nitrogen isotope in the case of an antineutrino. In both cases the nucleus is found in an excited state, releasing a de-excitation photon.

$$\nu_e + {}^{16}\mathrm{O} \rightarrow e^- + {}^{16}\mathrm{F}^* \tag{4.3}$$

$$\overline{\nu}_e + {}^{16}\mathrm{O} \rightarrow e^+ + {}^{16}\mathrm{N}^*. \tag{4.4}$$

Figure 16 shows the value for the cross section of each interaction channel as a function of the incoming neutrino energy. One may notice that at the most relevant energy range for supernova neutrinos $E_\nu < 50$ MeV, the dominant interaction channel is the inverse beta decay. As a result, Super-Kamiokande is mainly sensitive to electron antineutrinos.

Once Cherenkov light is captured by PMTs, the energy and direction of the incoming particle is determined. However, low energy particles have their signals mixed with background signal from other sources, such as natural radiation. Thus, Super-K detection threshold is 4.5 MeV, meaning that any incoming neutrino of less than 4.5 MeV generates a signal that cannot be distinguished from background noise.

On the case of supernova neutrinos, in the energy range of a few MeV, the energy resolution of Super-K lies around 14% at 10 MeV, ranging from 20% to 12% at ≈ 5 MeV and 16 MeV, respectively [76, 77], a analytic expression for the energy resolution of Super-K is given by $0.5\sqrt{E[\text{MeV}]}$ [78], which is going to be implemented in all simulations.

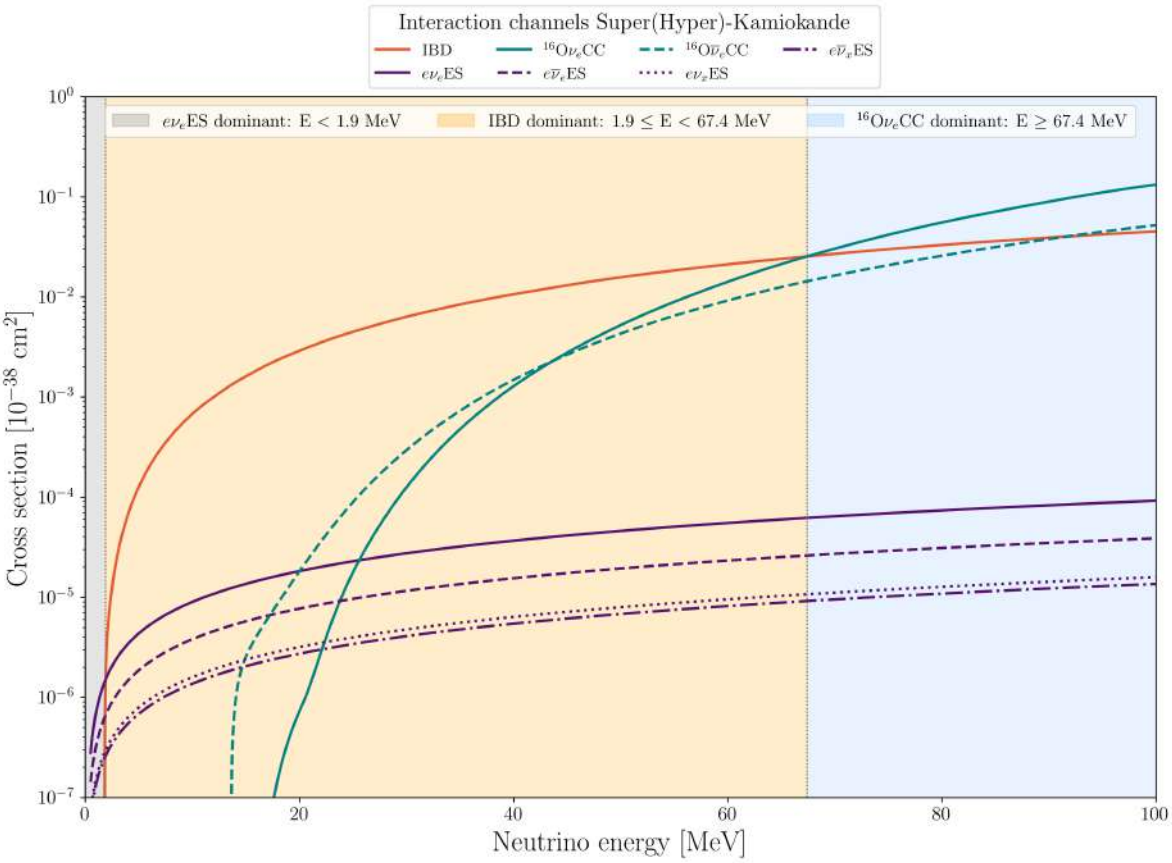

Figure 16 – All relevant cross sections for interaction channels in Super-K and Hyper-K. Regions are colored based on the dominant interaction. Numerical values for cross sections shown here and used in the simulations were retrieved from the SnowGlobes software [5].

Apart from the determination of a neutrino interaction and its energy, Super-

K possesses the ability of reconstructing the neutrino direction, although with a lower resolution, by using the photon arrival time at each PMT to determine the angle of the Cherenkov cone. Even though possible, it is not an easy task to reconstruct the direction of the incoming neutrino, for CC-ν^{16}O the eletron/positron emission is nearly isotropical, saving little information about the original neutrino direction, νeES interactions save some of the directional information depending on the neutrino energy (see figure 17), and IBD events show a slight anisotropy for the scattered positron, with the probability P of a given scattering angle θ after the interaction being almost uniform $P(\theta) \sim 1 - 0.102\cos(\theta)$, although this anisotropy is only observable when a large number of events is observed [79]. Therefore, in water Cherenkov detectors the main contribution for the directional information is the νeES interaction channel. On top of that, the angular resolution of Super-K is around 26 degrees for 10 MeV electrons [1] [77, 80], this results in a large background noise and a dispersed reconstruction even for events that conserve the overall direction of the incoming neutrino. There is also a possibility of separating, at least partially, the neutrino and antineutrino events due to the angular distributions [81], however since this possibility is not well discussed or explored as a feasible data analysis method by the Super-Kamiokande collaboration, we will not include this possibility in our work. In chapter 7 we will explore a technique to reconstruct the neutrino direction based on the angle distribution for a CCSN.

[1] Since the peak of neutrino energy spectrum is close to 10 MeV and given the lack of a phenomenological expression for the angular resolution in function of the neutrino energy, the value of 26° will be used in all simulations.

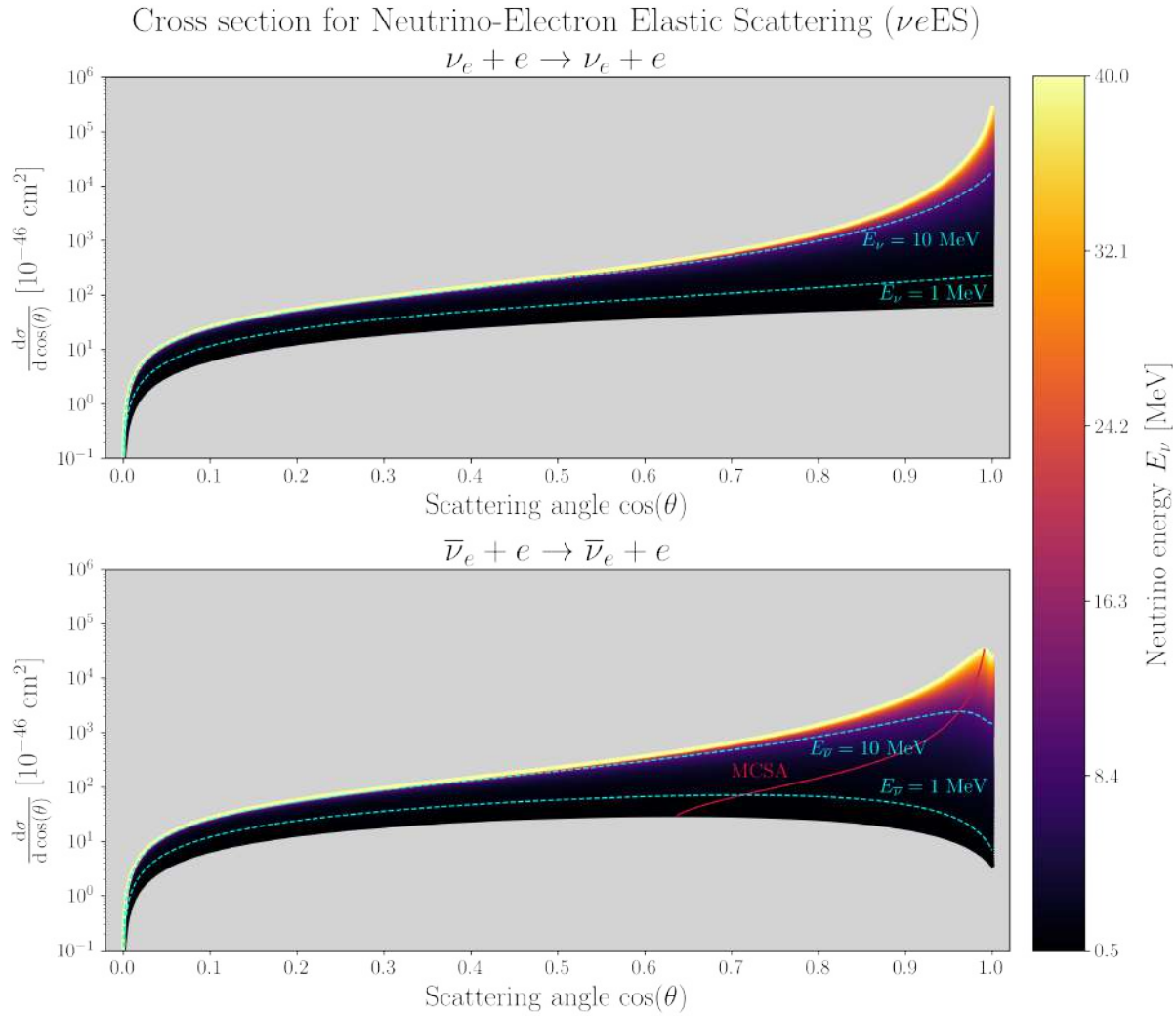

Figure 17 – Neutrino-Electron Elastic Scattering angular cross sections. In both panels, the color scheme indicates the energy of the incoming neutrino, two specific energies are marked in cyan for better visualization of the evolution of the cross section with neutrino energy. *Top panel:* Electron neutrino cross section. *Bottom panel:* Electron antineutrino cross section. The red curve indicates the peak of the angular cross section for each energy, named Maximum Cross Section Angle (MCSA). In the case of neutrinos, the peak is at $\cos(\theta) = 1$, or $\theta = 0$, for any energy. Both figures were done considering the νeES angular cross section shown in chapter 5 of [6].

4.1.1 Hyper-Kamiokande

Super-Kamiokande is planned to be upgraded into a new detector of 258 ktons, with a fiducial volume of 187 ktons. This new detector will be named Hyper-Kamiokande and will be part of the future generation of neutrino detectors. The inner detector, that now has $\approx$ 11 thousand PMTs, will be covered in 40 thousand PMTs of 50 cm in diameter. The increase of one order of magnitude in the detector volume will make Hyper-K the biggest CCSN neutrino detector. Since the detector's material will be the same, the detection channels are the same as Super-K.

As for it's predecessor, Hyper-K will be able to detect neutrinos from supernova events with a energy threshold of 4.5 MeV [82]. However, the energy resolution is still unclear. In Super-Kamiokande, an electron linear accelerator (LINAC) with known beam characteristics was used to calibrate the energy reconstruction methods and to quantify the energy resolution. Since Hyper-K has a much larger volume, the operation of the LINAC system carries a heavier burden, thus other options for calibration are still under development. Due to this lack of available data on the energy resolution of Hyper-K, throughout this work we will assume the same energy resolution of Super-K.

4.2 DUNE

The Deep Underground Neutrino Experiment (DUNE) is a future generation detector based on the technology of Liquid Argon Time Projection Chamber (LArTPC). Located 1.5 km below the surface at the Sanford Underground Research Facility (SURF) and coordinated by Fermilab[2], the detector is composed of 4 detection LarTPCs summing a total of 40 ktons of liquid argon [83].

Argon is a noble gas, which ensures that electrons generated by any interactions will not be captured back, being instead deviated by the electric field inside the detector until they hit one of the anodes, generating an electric signal [84]. Also, argon possess the property of scintillating upon the passage of ionizing radiation, for this reason photon detectors fill the chamber to capture scintillation photons of wavelength 127 nm [85]. The detection of both electrons/positrons emitted from the interactions and the de-excitation photons allows a better reconstruction of the neutrino energy

As a result of the choice of argon as the detector material, the interaction channels of DUNE are

- **Neutrino-Nucleus Charged Interaction (CC-ν^{40}Ar):** Just as for the case for Super-K, the neutrino might exchange a charged boson ($W^{\pm}$) with a nucleon inside the argon nucleus, producing a electron or positron and converting the argon nucleus in a potassium isotope (in the case of an electron neutrino interaction) or a chlorine (in the case of an electron antineutrino). In both situations the signal is generated by the track left by the electron/positron and the de-excitation photon from the resulting isotope.

$$\nu_e + {}^{40}\text{Ar} \rightarrow e^- + {}^{40}\text{K}^* \tag{4.5}$$

$$\overline{\nu}_e + {}^{40}\text{Ar} \rightarrow e^+ + {}^{40}\text{Cl}^*. \tag{4.6}$$

[2] Fermilab has an active YouTube channel with several videos and animations about its experiments. The interested reader may check The Science of the Deep Underground Neutrino Experiment (DUNE) and also How to Detect a Neutrino by Matt O'Dowd, host of the YouTube channel PBS Spacetime

- **Neutrino-Electron Elastic Scattering (νeES):** As for the case of Super-K, a neutrino, or antineutrino, of any flavor exchanges a neutral boson (Z^0) with a valence electron on argon. The electron absorbs some of the neutrino energy, releasing itself from the atom and moving through the medium. However, instead of being detected by the emission of Cherenkov light, the electron is detected by the track left inside the LArTPC as it drifts inside the chamber and indues ionization charges in the anodes.

$$\nu + e^- \rightarrow \nu + e^- \tag{4.7}$$

  Here ν denotes a neutrino or antineutrino of any flavor.

- **Neutrino-Nucleus Neutral Interaction (NC-ν^{40}Ar):** Since one of the detection methods consists of the capture of de-excitation photons, another type of interaction becomes possible. The exchange of a neutral boson between the neutrino and the argon nucleus induces a M1 transition, resulting in a spin-flip of the nucleus and releasing a de-excitation cascade of photons of energy 9.8 MeV [85]. At this energy, the production of e^-e^+ pairs offers a possible way of tagging neutral-current interactions, although this process is still under investigation.

$$\nu + {}^{40}\text{Ar} \rightarrow \nu + {}^{40}\text{Ar}^*. \tag{4.8}$$

Figure 18 shows the cross sectional dependence with the neutrino energy for all possible interactions inside the detector. The main cross section is the ν^{40}ArCC, making DUNE main sensitivity towards electron neutrinos. This represents a unique opportunity, as DUNE will be the only detector sensitive to electron neutrinos, to investigate physics at the neutronization peak and neutrino mass hierarchy [85].

Liquid argon has a small concentration of ^{39}Ar, which suffer beta decay, emitting charged particles and producing a background signal that reaches 0.57 MeV [86, 87]. However, radioactive backgrounds creates low rates of relevant noise at the timescale of a supernova burst detection and the detection threshold energy is dependent almost entirely of the interaction energy threshold for each interaction channel, so conservatively, we consider a detection threshold of 5 MeV [85][3].

[3] Three simulations for the detection efficiency are presented in the design report of DUNE. They assume a reconstruction power of at least 1, 3 and 5 MeV. Since the efficiency rapidly approaches 100% in all simulations, after 10 MeV and drop rapidly close to 5 MeV, we set 5 MeV as a detection energy threshold

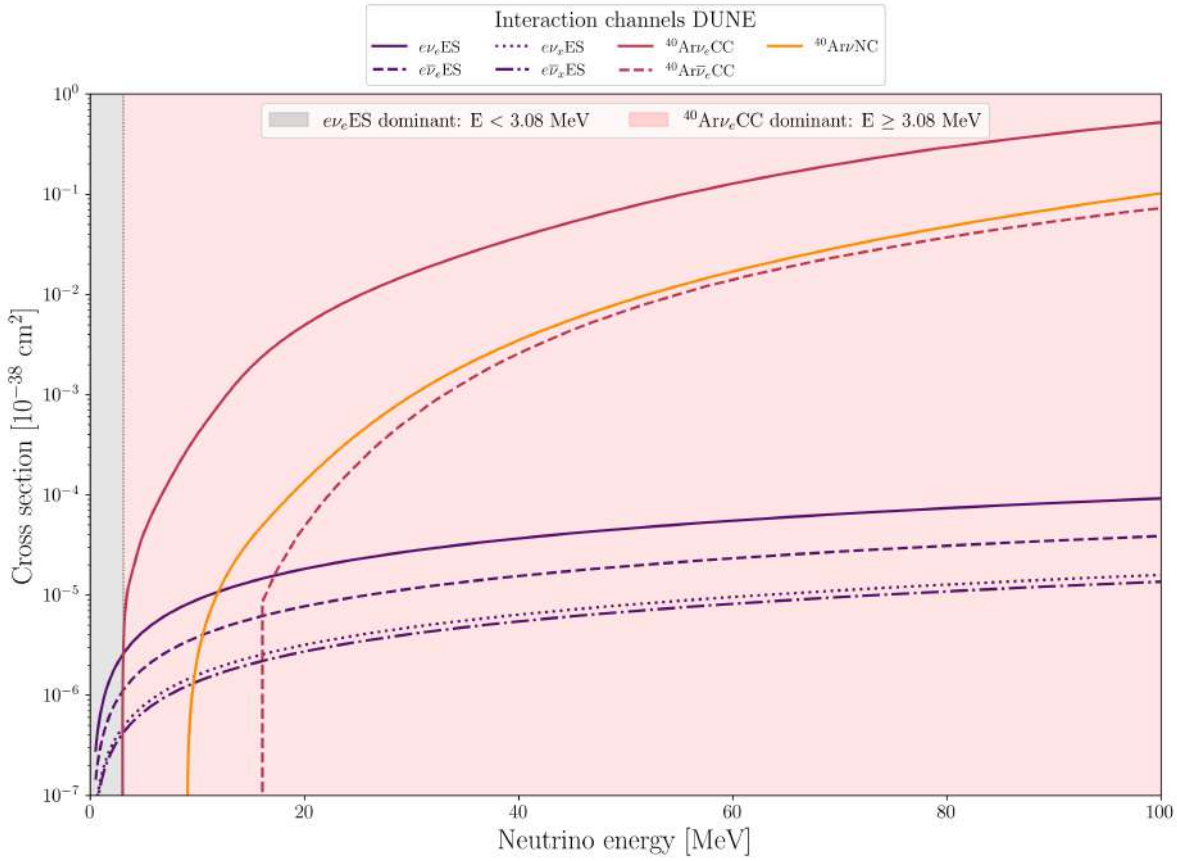

Figure 18 – All relevant cross sections for interaction channels in DUNE. Regions are colored based on the dominant interaction. Numerical values for cross sections shown here and used in the simulations were retrieved from the SnowGlobes software [5].

The reconstructed neutrino energy is the sum of the reconstructed energies for all the final state particles. In DUNE, only the photons and electrons/positrons are observable, since the nuclear recoil is not measured. This introduces errors to the reconstruction of the neutrino energy, associated with the measured energy for both the electron/positron and the photon, and the uncertainty around the recoil energy of the nucleus. As a result, the expected energy resolution in DUNE is $0.11\sqrt{E[\text{MeV}]} + 0.02(E[\text{MeV}])$ [78]. Note however that since both electrons/positrons emitted from the interactions and the de-excitation photons are captured, DUNE has a greater power to reconstruct the neutrino energy than Super/Hyper-K. The different de-excitation energies of the photons from neutrino and antineutrino CC interactions also provide a way to partially separate the neutrino and antineutrino signal, which is essential to study the neutrino mass hierarchy, although due to the lack of a detailed study on the matter, we choose to ignore this possibility.

4.3 JUNO

The fourth detector explored is the Jiangmen Underground Neutrino Observatory (JUNO), a liquid scintillation and a Cherenkov detector underground in China, also part of the future generation. JUNO's central detector is the scintillator of 20 ktons of fiducial mass. The central detector is submerged on a water pool to provide shielding from natural radioactivity and cosmic rays, the Cherenkov detector is inside the pool to provide characterization of background noise. The detector's material consists of a linear alkylbenzene of 10 to 13 carbons attached to a benzene ring. The material provides carbon atoms as targets to neutrino interactions, as well as excellent transparency, low chemical reactivity, and good light yield [88].

Four main detection channels are possible for JUNO:

- **Inverse Beta Decay (IBD):** Just as Super-K, electron antineutrinos may interact with a proton on alkylbenzene molecule and convert it into a neutron, releasing a positron that is annihilated with a electron on the medium, giving of a signal of photons with energy 0.511 MeV. In addition, the free neutron is captured by a proton, producing a 2.2 MeV photon. The coincidence of the prompt and delayed signals provide a tagging method for recognition of a IBD event. In this work we assume 95% tagging efficiency for IBD events.

$$\overline{\nu}_e + p \rightarrow n + e^+. \tag{4.9}$$

- **Neutrino-Electron Elastic Scattering (νeES):** Again, in the same manner as described in Super-K and DUNE, neutrinos, or antineutrinos, of any flavor exchanges a neutral boson (Z^0) with a valence electrons on the alkylbenzene molecule.

$$\nu + e^- \rightarrow \nu + e^-. \tag{4.10}$$

  Here ν denotes a neutrino or antineutrino of any flavor.

- **Neutrino-Nucleus Charged Interaction (ν^{12}CCC):** Since carbon is the interaction material, charged current interactions via electron neutrinos (W^+) or antineutrinos (W^-) also provide a valuable detection channel. In this case, the carbon nucleus is converted into a nitrogen isotope in the case of a neutrino and a boron isotope in the case of an antineutrino. The minimum energy for this reaction to occur is 17.34 MeV and 14.39 MeV, for the neutrino and antineutrino, respectively. Both resulting isotopes undergo beta decay with a lifetime of a few milliseconds after formation (20.2 ms for ^{12}B and 11 ms for ^{12}N). The delay difference between the prompt signal generated by the electron or positron and the beta decay signal may

provide a way of differentiating between ν_e and $\overline{\nu}_e$ [89].

$$\nu_e + {}^{12}\mathrm{C} \rightarrow e^- + {}^{12}\mathrm{N} \tag{4.11}$$

$$\overline{\nu}_e + {}^{12}\mathrm{C} \rightarrow e^+ + {}^{12}\mathrm{B}. \tag{4.12}$$

- **Neutrino-Nucleus Neutral Interaction (ν^{12}CNC):** As the case for DUNE LArTPC, liquid scintillators also may observe de-excitation photons from an excited nucleus resulting from neutral current interactions. The resulting de-excitation photon carries an energy of 15.11 MeV.

$$\nu + {}^{12}\mathrm{C} \rightarrow \nu + {}^{12}\mathrm{C}^*. \tag{4.13}$$

Figure 19 shows all JUNO interaction cross sections considered in this work. Another interaction channel proposed for the detector is the neutrino-proton elastic scattering, which may provide 2800 detection events above 0.1 MeV for a galactic supernova. A large benefit of this cross section is its main sensitivity to the tail of the neutrino energy spectrum and a larger sensitivity to μ and τ neutrinos, given their higher energy. However, the characteristics of the PMTs impose a minimum energy threshold of 0.3 MeV, lowering the number of events to 1,000. A more conservative threshold of 0.7 MeV as required by reactor neutrino physics lowers the number of events to 300. There are also uncertainties regarding the feasibility of detecting the proton recoil due to the proton quenching factor, which is not yet known in JUNO.

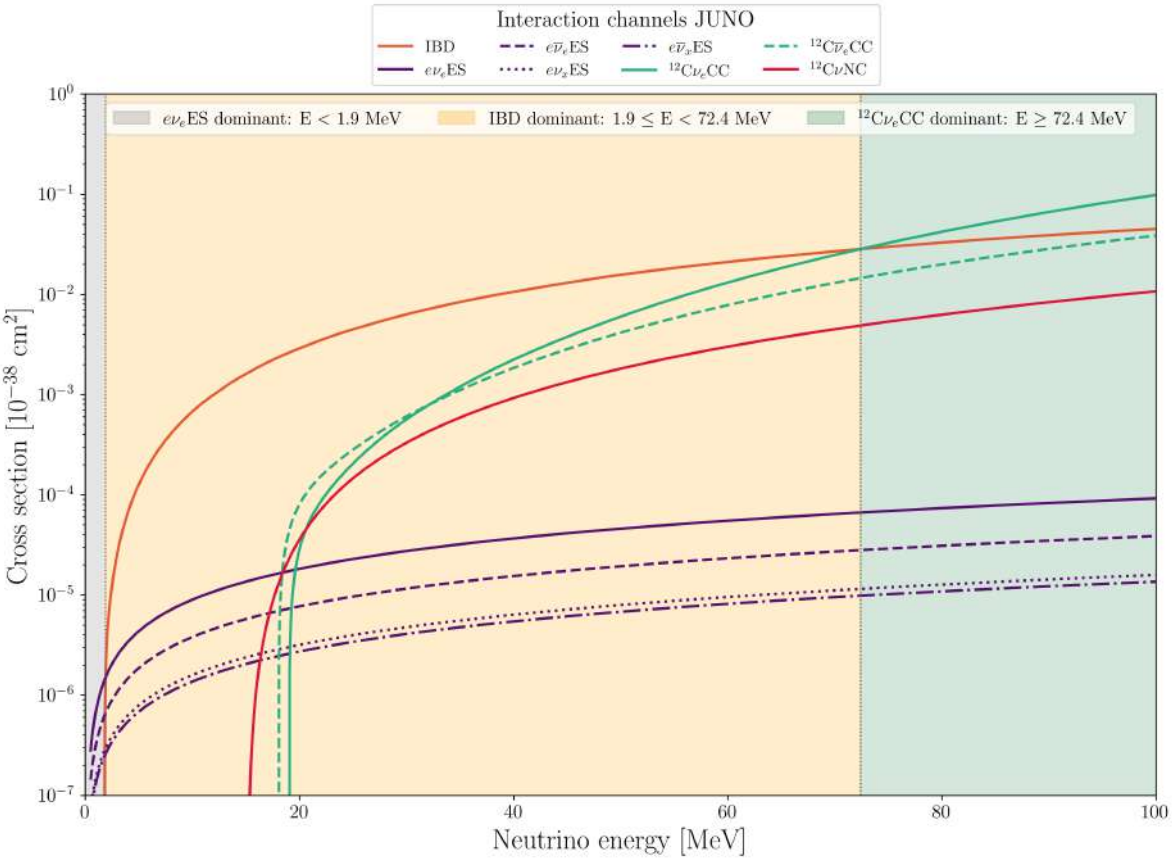

Figure 19 – All relevant cross sections for interaction channels in JUNO. Regions are colored based on the dominant interaction. Numerical values for cross sections shown here and used in the simulations were retrieved from the SnowGlobes software [5].

Regarding the energy resolution, JUNO is expected to achieve an error in neutrino energy reconstruction of $0.03\sqrt{E[\text{MeV}]}$, resulting in 3.1% at 10 MeV, 4.5x smaller than Super-K, this is a result of the detection process which allows the capture of both ionization photons and electron-positron annihilation photons. Hence, in IBD events for example, the full kinetic and rest energies of the positron are reconstructed and since $E_{e^+} \approx E_\nu - (m_n - m_p)$, the neutrino energy is reconstructed with better precision.

Figure 20 shows the energy dependence of the reconstruction resolution of all detectors as a function of the incoming neutrino energy, JUNO presents the lowest increase with increasing energy, granting it a finer energy distribution for a detected supernova.

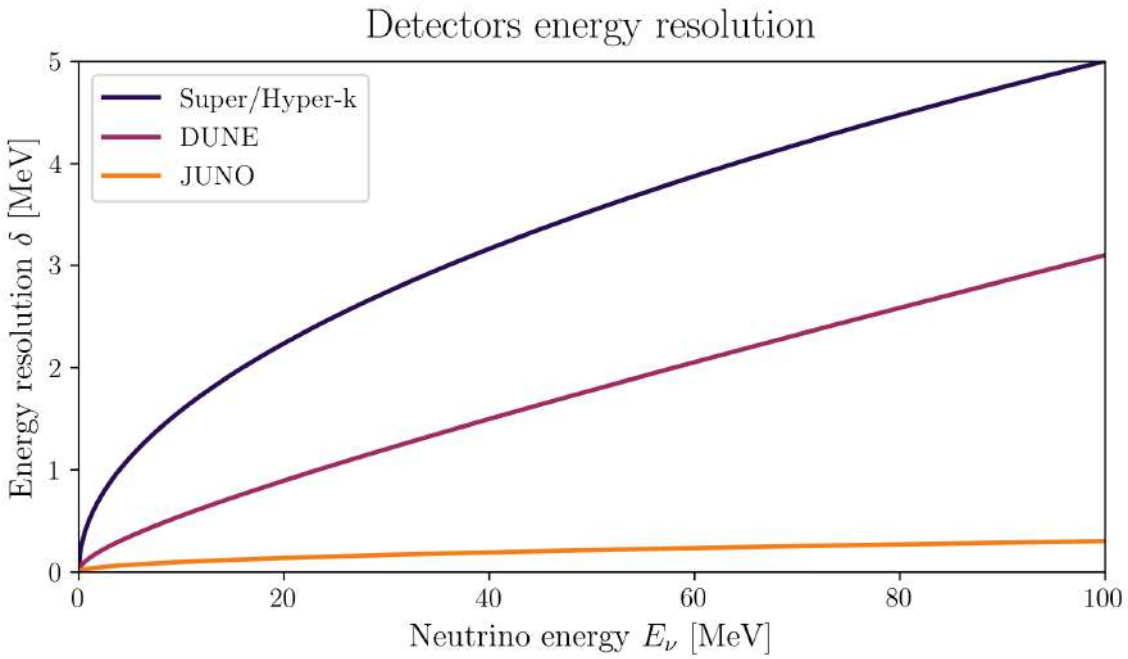

Figure 20 – Energy resolution in all four detectors as a function of the incoming neutrino energy. Super-K and Hyper-K have the same resolution and so are shown as the same curve. Larger resolutions imply in larger uncertainties in the neutrino energy reconstruction process after detection.

5 Neutrino Detection on Earth

Here the effects of Earth matter and detector's characteristics are used to explore the relevant variables concerning the detection of neutrinos from supernovae.

> Eight solid light-years of lead ... is the thickness of that metal in which you would need to encase yourself if you wanted to keep from being touched by neutrinos. I guess the little f*ckers are everywhere.
>
> *Michael Chabon*

We are now in position to begin the description of the simulations implemented trough this work. In this chapter we will describe the methods for simulating the neutrino energy spectrum that should be detected in each of the four detectors described in the previous section.

5.1 Production and Emission Spectra

As discussed previously, the neutrino energy flux of a given flavor β is parameterized by an almost Fermi-Dirac distribution with two main parameters, the average neutrino energy $\langle E_\beta \rangle$ and the pinch parameter α_β. At the same time, the luminosity L_β indicates the height of the energy flux distribution at a given instant t.

$$\mathcal{F}^0_\beta(E,t) = \frac{\mathrm{d}N_\beta(t)}{\mathrm{d}E} = \frac{L_\beta(t)(1+\alpha_\beta(t))^{1+\alpha_\beta(t)}}{\Gamma(1+\alpha_\beta(t))\,\langle E_\beta(t)\rangle^{2+\alpha_\beta(t)}} E^{\alpha_\beta(t)} \exp\left(-\frac{(\alpha_\beta(t)+1)E}{\langle E_\beta(t)\rangle}\right). \tag{5.1}$$

In our work, we extract the values of $\langle E_\beta(t)\rangle$, $\alpha_\beta(t)$ and $L_\beta(t)$ as functions of the time after the core bounce from numerical simulations provided by the Garching group [3]. Simulations span about 10 seconds (post bounce) of neutrino dynamics and production during the core collapse supernova (CCSN). In order to obtain the final neutrino energy spectrum, the flux is integrated over time. After the integration, a simple curve fitting process of (5.1) is performed using least squares method to obtain $\langle E_\beta \rangle$, α_β and L_β for the whole energy spectrum.

One may wonder if performing a curve fit of (5.1) on a sum of three other functions described according to (5.1) but with different parameters is actually reasonable. Much like a sum of sine functions does not yield a function that can be fully described by

single other sine function (if the frequencies are different), the sum of these time-integrated fluxes might not follow the same distribution that each one does separately.

In order to evaluate the acceptability of this assumption we computed both the difference between the total time-integrated flux and the fitted curve $\left|\mathcal{F}^0(E) - \mathcal{F}^{0,\text{fitted}}(E)\right|$ and the fractional difference between both curves, with respect to the fitted curve $(\mathcal{F}^0(E) - \mathcal{F}^{0,\text{fitted}}(E))/\mathcal{F}^{0,\text{fitted}}(E))$.

Figure 21 shows the result of the fitting and the difference comparison. It is clear that although the difference reaches an order of magnitude of $10^9\text{MeV}^{-1}\text{cm}^{-2}$, this order is two orders of magnitude below the actual range of the flux. This effect is even more diminished when we take into account the low interaction cross-section of neutrinos. The bottom left graph of the figure shows as that the biggest fractional difference between the adjustment and the numerical result is when $E \to 0$ and for larger values of E. The difference in low energy does not affect the detection process due to the low cross-section value for all interactions at lower energies and the detectors efficiency thresholds. The larger energies are concentrated at the tail of the energy spectrum and therefore imply in low probability of neutrinos in that tail contributing to the total amount detected. Furthermore the integral of $\mathcal{F}^0(E)$ and $\mathcal{F}^{0,\text{fitted}}(E)$, in the energy, differ by $\Delta_{\text{num}-\text{fit}} = 0.83\%$ (we will see that the integral of the spectrum is an essential quantity for our analysis). Considering a scenario where 10 thousand neutrinos are detected, the use of the fitted curve would yield 83 neutrinos less, which is below the statistical fluctuation range when considering the stochastic nature of the detection. This can be shown by considering that the number of detected neutrinos is given by a Poisson distribution (more details further) which for a mean value of 10,000 has a variance σ^2 of 10,000 and a standard deviation of 100. Thus $\sigma^2_{\text{Stochastic}} \gg \Delta_{\text{num}-\text{fit}}$. In light of these arguments, we consider that equation (5.1) is well suited to describe the shape of the total energy spectrum emitted in neutrinos by a core collapse supernova.

Table 1 contains the resulting parameters for each flavor in four CCSN simulations with two different stellar masses and two different equations of state (EoS). These are the values assumed in the simulations of the neutrino production spectrum.

EoS	Mass $M_\odot$	α (ν_e, $\overline{\nu}_e$, ν_x)	$\langle E_e \rangle$ (ν_e, $\overline{\nu}_e$, ν_x) [MeV]	L_e $\times 10^{52}$ [ergs]
LS220	11.2	2.96, 2.55, 2.12	10.31, 12.90, 12.86	3.50, 3.09, 3.01
LS220	27.0	2.76, 2.47, 2.07	11.06, 13.82, 13.76	5.70, 5.40, 5.06
Shen	11.2	2.95, 2.37, 2.00	9.77, 12.01, 11.65	3.21, 2.83, 2.54
Shen	27.0	2.72, 2.25, 1.92	10.31, 12.67, 12.17	5.27, 5.00, 4.27

Table 1 – Results of all parameters that describe the energy spectrum in each neutrino type, in all four simulations implemented.

In order to account for the MSW effect, we work with two possibilities in our simulations: normal mass hierarchy and inverted mass hierarchy. The final emission

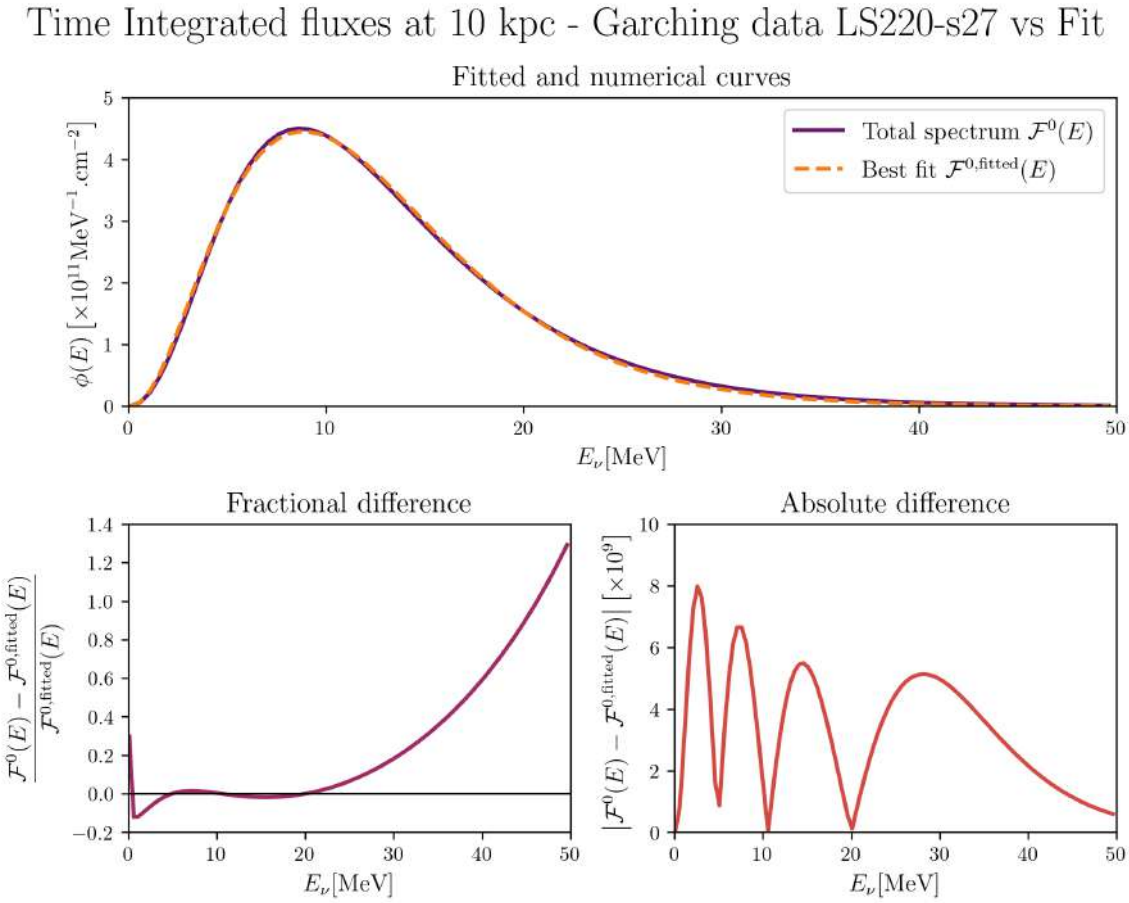

Figure 21 – Simulated results for the total spectrum, represented as the time-integrated flux, of neutrinos from a 27 $M_\odot$ core collapse supernova at 10 kiloparsecs away and fitted curve with equation (5.1). Top graph shows both curves, while the bottom two show their absolute (right) and fractional (left) differences.

neutrino spectrum in the normal mass hierarchy is given by

$$\mathcal{F}_e = |U_{e2}|^2 P_H \mathcal{F}_e^0 + (1 - P_H |U_{e2}|^2)\mathcal{F}_x^0, \tag{5.2}$$

$$\mathcal{F}_{\bar{e}} = |U_{e1}|^2 \mathcal{F}_{\bar{e}}^0 + |U_{e2}|^2 \mathcal{F}_x^0, \tag{5.3}$$

$$4\mathcal{F}_x = (1 - |U_{e2}|^2)P_H \mathcal{F}_e^0 + |U_{e2}|^2 \mathcal{F}_{\bar{e}}^0 + (3 - |U_{e2}|^2 + |U_{e2}|^2 P_H)\mathcal{F}_x^0, \tag{5.4}$$

while the emission spectrum in the inverted mass hierarchy is

$$\mathcal{F}_e = |U_{e2}|^2 \mathcal{F}_e^0 + |U_{e1}|^2 \mathcal{F}_x^0, \tag{5.5}$$

$$\mathcal{F}_{\bar{e}} = |U_{e1}P_H|^2 \mathcal{F}_{\bar{e}}^0 + (1 - P_H |U_{e2}|^2)\mathcal{F}_x^0, \tag{5.6}$$

In both cases, P_H is given by (3.21), with $Y_e = 0.5$, $A = 10^{10}$ and $m_N = 938$. These values were chosen to represent well the matter density of a collapsing star for $\rho > 1$ g/cm^3. Since the resonance layer is above this density, the exact details of the composition

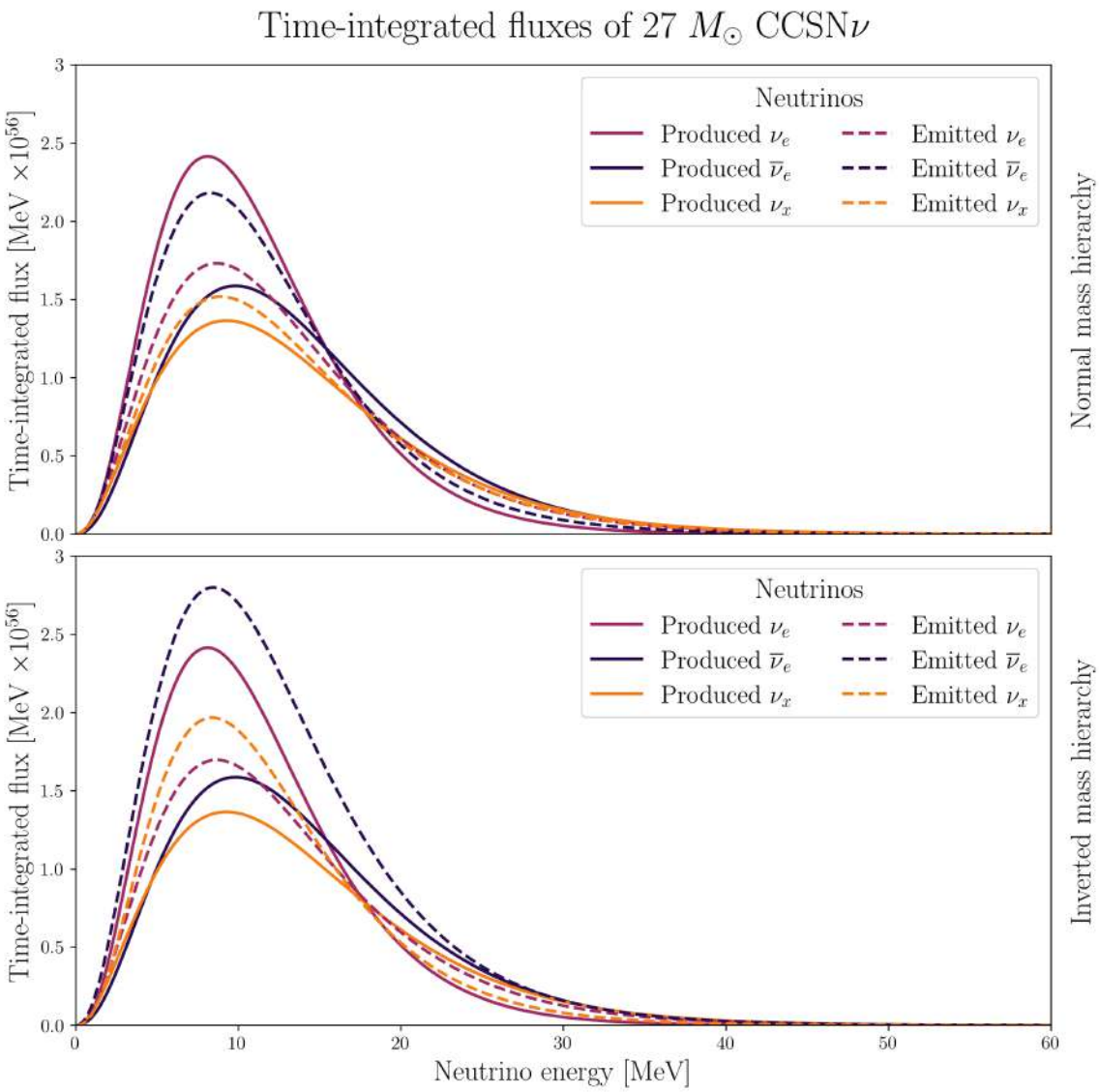

Figure 22 – Time integrated fluxes of ν_e, $\overline{\nu}_e$ and ν_x that are produced (continuous lines) and emitted (dashed lines) from the supernova after the flavor transition induced by the MSW effect. Top graph shows the result for a normal mass hierarchy scenario and the bottom for inverted mass hierarchy.

of the star that changes the density profile for $\rho < 1$ g/cm^3 do not impact the flavor transition [68, 67]. Figure 22 shows the result for the final emission neutrino spectrum, represented by the time-integrated flux, in the scenario of 27 solar masses, with LS220 EoS. In both scenarios, ν_e has the highest peak for the production; however due to the MSW effect $\overline{\nu}_e$ is the neutrino flavor mostly emitted from the supernova.

5.2 Earth Matter Effect

On top of the MSW oscillation inside the collapsing star, supernovae neutrinos might undergo flavor oscillation when crossing Earth. This phenomenon depends on the traveled distance inside Earth and due to non adiabatic transitions between Earth layers.

It also depends on whether the neutrinos crossed only Earth's mantle or both the mantle and the core.

As previously discussed, this effect, our method involves the numerical solution of the MSW effect inside Earth, for a given supernova location in the sky and detection date. The numerical solution yields the transition probabilities $p^{\odot}$ and $\overline{p}^{\odot}$ for neutrinos and antineutrinos, respectively. Which then are used to compute the neutrino energy spectra, in each flavor, that reaches the detector, using equations (3.41) to (3.43).

5.3 Detected Spectra

The expected detected spectrum is a result of the spectrum that arrives at the detector, combined with the characteristics of the detection such as the distance, the total cross section for a neutrino interaction, the energy resolution of the detector, the energy threshold and the size of the detector, as well as its material.

$$\mathcal{F}_{\beta}^{d}\left(E^{\text{obs}}\right) = \int \frac{N_T}{4\pi D^2}\mathcal{F}_{\beta}(E)\sigma_{\beta}(E)\varepsilon(E)\mathcal{R}(E^{\text{obs}}; E, \delta)\mathrm{d}E, \tag{5.7}$$

where $\mathcal{F}_{\beta}^{d}(E)$ is the detection neutrino spectrum of flavor β, N_T is the total number of target particles, that depends on the detector's size and material, $\sigma_{\beta}(E)$ is the total interaction cross section for the neutrino flavor β and $\varepsilon(E)$ is the detector's efficiency curve. In our simulations, $\varepsilon(E)$ is given by a step function

$$\varepsilon(E) = \begin{cases} 0 & \text{if } E < E_{\text{th}} \\ 1 & \text{if } E \geqslant E_{\text{th}} \end{cases}, \tag{5.8}$$

that is, we are considering 100% efficiency in detecting neutrinos above the detection threshold E_{th}, and $\mathcal{R}(E^{\text{obs}}; E, \delta)$ is the resolution function of the detector (more details in chapter 6). The total neutrino spectrum is given by the sum of all flavors

$$\mathcal{F}^{d}\left(E^{\text{obs}}\right) = \sum_{\beta\in\{e,\overline{e},x\}} \mathcal{F}_{\beta}^{d}\left(E^{\text{obs}}\right). \tag{5.9}$$

By performing the integration in energy of the spectrum, we obtain the total number of expected events at the detector N_{ν}^{0}. Figure 23 shows the normalized production neutrino spectrum for LS220-27.0 and the normalized detection spectrum for DUNE and Super-K.

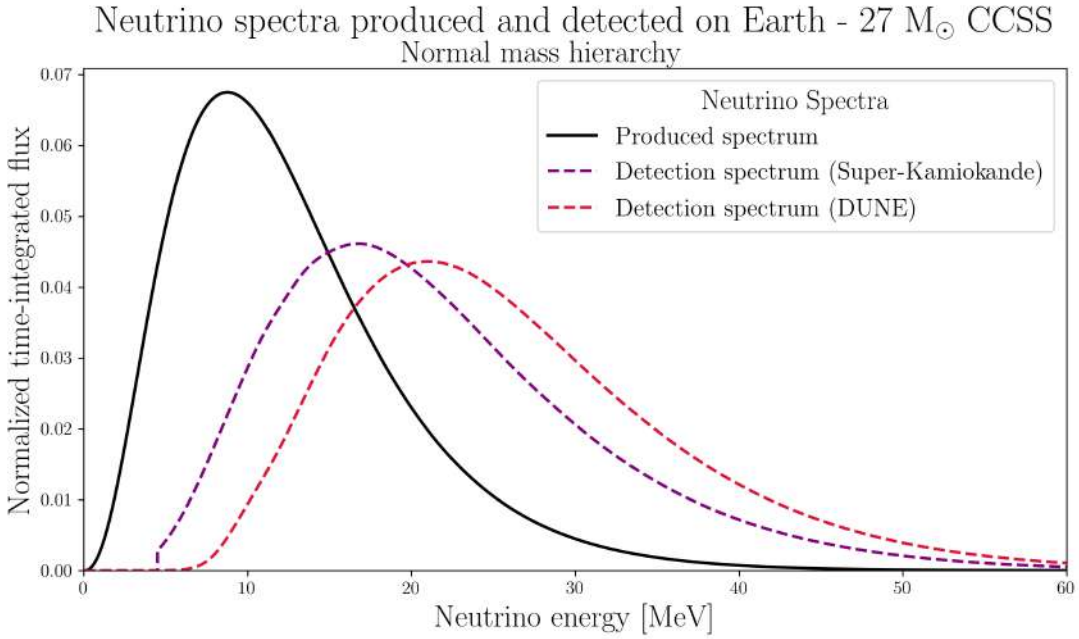

Figure 23 – Normalized production and detection neutrino spectra from a 27 $M_\odot$ CCSN (model LS220-27.0) in normal mass hierarchy. The detected spectra is shown for Super-Kamiokande and DUNE. Hyper-Kamiokande is not shown since the shape of the detected spectrum is the same as for Super-K once the only difference between detectors is the total number of target particles. JUNO is also not shown in order to avoid visual confusion, since it spectrum has a shape that is also very similar to Super-K's shape.

However, due to the stochastic nature of particle interactions and the detector's imperfections, the true detection spectrum is not given simply in terms of (5.9). One must proceed to introducing the relevant statistical fluctuations in order to simulate a real detection.

The process starts as following, the expected detection spectrum is used as a probability distribution for detecting a neutrino with a given energy E. The true number of detected neutrinos is given by a random number, sampled from a Poisson distribution with parameter $N_\nu^{0,\beta}$

$$N_\nu^\beta \sim \text{Poisson}(n; N_\nu^{0,\beta}) = \frac{\left(N_\nu^{0,\beta}\right)^n e^{-N_\nu^{0,\beta}}}{n!} \text{ where,} \qquad (5.10)$$
$$N_\nu^{0,\beta} = \int_0^\infty \mathcal{F}_\beta^d(E)\mathrm{d}E,$$

where n is the integer variable of the distribution. In practice, the integral is not evaluated from 0 to ∞; numerically we integrate $\mathcal{F}_\beta^d(E)$ from 0 to 100 MeV. The effect of this step is the introduction of a fluctuation in the number of detected neutrinos in each flavor, as a result of the probabilistic nature of particle interactions. The choice of a Poisson distribution is due to the binary nature of the detection, it either occurs or not. The Poisson

distribution expresses the probability of a given number of discrete events occurring in a fixed interval of time, in this case the supernova burst of a few seconds, if these events occur with a known constant mean rate and independently of the time since the last event, which is exactly the statistical nature of particle detection [90].

Once N_ν^β is defined, we sample N_ν^β energies from $\mathcal{F}_\beta^d(E)$, representing the energies of all neutrinos that interacted and produced a detectable signal. The second process for the introduction of errors is the errors associated to the detector. For each sampled energy E_i (the true energy), we re-sample a new energy value (the reconstructed energy) from a normal distribution with mean E_i and standard deviation equal to the detectors resolution δ

$$E_i^{\text{obs}} \sim \text{Normal}(E_i, \delta) = \frac{1}{\delta\sqrt{2\pi}} \exp\left[-\frac{1}{2}\left(\frac{E - E_i}{\delta}\right)^2\right]. \tag{5.11}$$

The use of a normal distribution relies on the assumption that the probability of observing an energy above and below the true value is the same. This is a valid assumption in most cases where the neutrino energy is in the order of a few GeVs [91]. For MeV neutrinos, in the low energy limit $E < 10$ MeV, the resolution function tends to yield a larger probability of reconstructing a neutrino energy lower than the actual value [92]. However, this effect is small compared to a gaussian distribution and the low energy events are usually scarce; thus we proceed to use a normal distribution regardless of the true neutrino energy[1]. Figure 24 shows the smearing matrix constructed from (5.11) with $\delta = 0.5\sqrt{E}$ (Super/Hyper-K), from a given input energy E, there is a probability distribution around E^{obs} from which a new value is sampled.

After both steps were taken, we obtain the final detected spectrum given as a distribution of observed energies for all detected events. As a simplification, for each detector, the bin width of the final histogram of the detected events is defined in terms of twice the largest error for the resolution width at 50 MeV. Therefore, for Super/Hyper-K, the bin widths are 7 MeV, DUNE has bin width of size 3.5 MeV, and finally JUNO has a width of 1 MeV.

All relevant information presented in the last chapters that must be used to obtain the neutrino spectrum that should be detected at a given detector is presented in table 2.

[1] In the future, for building the Python library for simulating supernova detection through neutrinos, we will apply more realistic forms of the resolution function, such as the Lognormal distribution, for low energies.

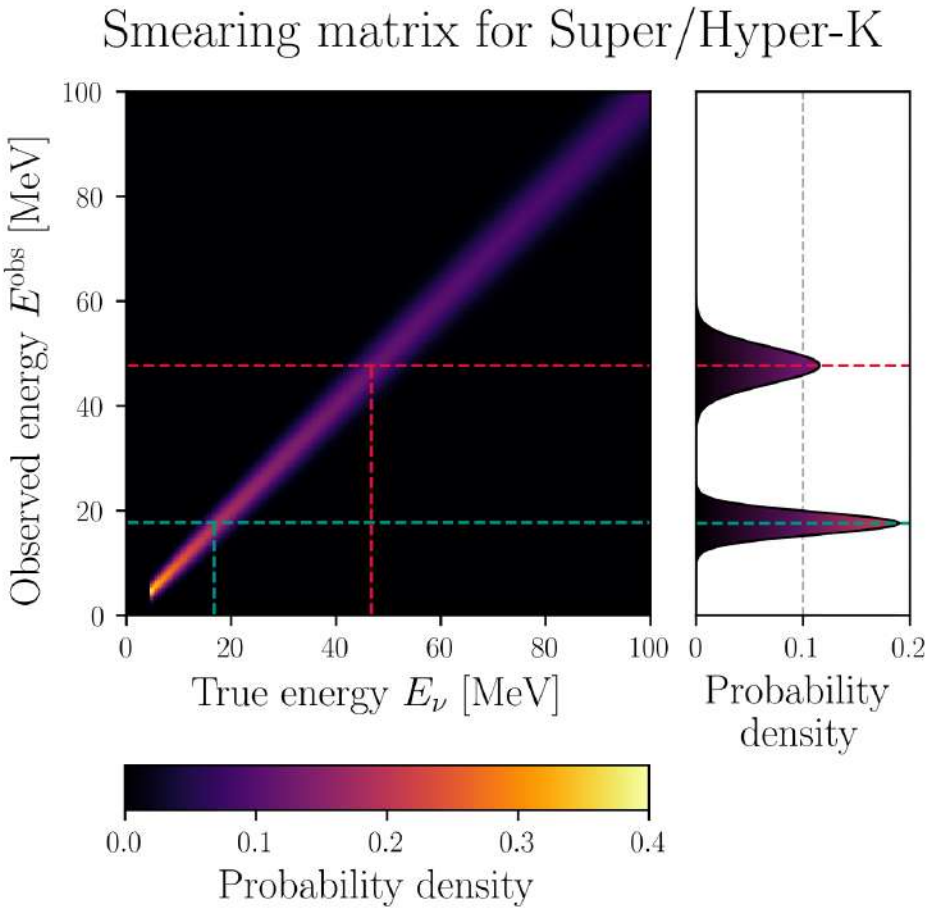

Figure 24 – Smearing matrix relating the true neutrino energy E_ν with the observed E^{obs}. The probability distribution for a reconstructed energy widens with a larger incoming E_ν.

Detector	N_T	σ	E_{th} (MeV)	δ (MeV)
Super-K	$\approx 2.14 \times 10^{33}$	IBD + νeES + ν^{16}OCC	4.5	$0.5\sqrt{E}$
Hyper-K	$\approx 1.44 \times 10^{34}$	IBD + νeES + ν^{16}OCC	4.5	$0.5\sqrt{E}$
DUNE	$\approx 6.03 \times 10^{32}$	ν^{40}Ar(CC + NC)+ νeES	5	$0.11\sqrt{E} + 0.02(E)$
JUNO	$\approx 1.50 \times 10^{33}$	IBD + νeES + ν^{12}C(CC + NC)	0.7	$0.03\sqrt{E}$

Table 2 – Detector's characteristics used for all simulations.

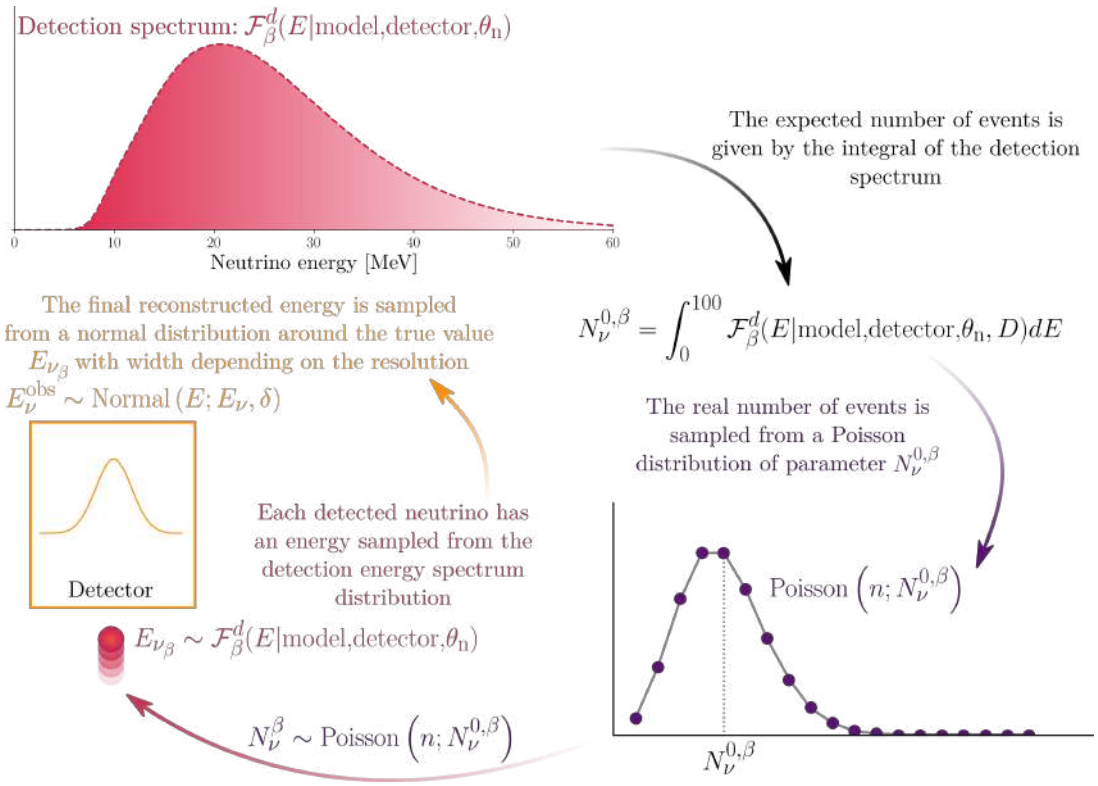

Figure 25 – Schematic view of the neutrino energy sampling process. From the expected detection energy spectrum the total expected number of events is used as a parameter to sample a true number of detected neutrinos from a Poisson distribution. For each detection event, a neutrino energy is sampled from the normalized expected detection spectrum. The final reconstructed energy for the neutrino is sampled from a normal distribution around the true energy, with width depending on the detector's resolution.

5.4 Angular distribution

As discussed in chapter , supernova neutrinos in water Cherenkov detectors that interact via ^{16}O charged/neutral current or inverse beta decay release charged particles and photons nearly isotropically, losing all information regarding the neutrino direction. However, elastic scattering events tend to statistically preserve the direction of the incoming neutrino and may offer a way for pinpointing the direction of a supernova. In Liquid Scintillators, the released neutron from IBD events is also a possible proxy for determining the direction of supernovae [79]. Other methods for pinpoint of supernovae directions in the sky using neutrinos is the triangulation of the supernova using the locations and detection times of at least three detectors on Earth's surface [93, 94].

The neutrino scattering process is schematized in figure 26. A neutrino with a incident angle θ_ν, with respect to the detector's frame of reference, scatters a electron with a angle θ, assuming a direction described by the angle $\beta = \theta_\nu + \theta$. The detector observes the Cherenkov cone from the outgoing electron and reconstruct it angle with a resolution δ_θ.

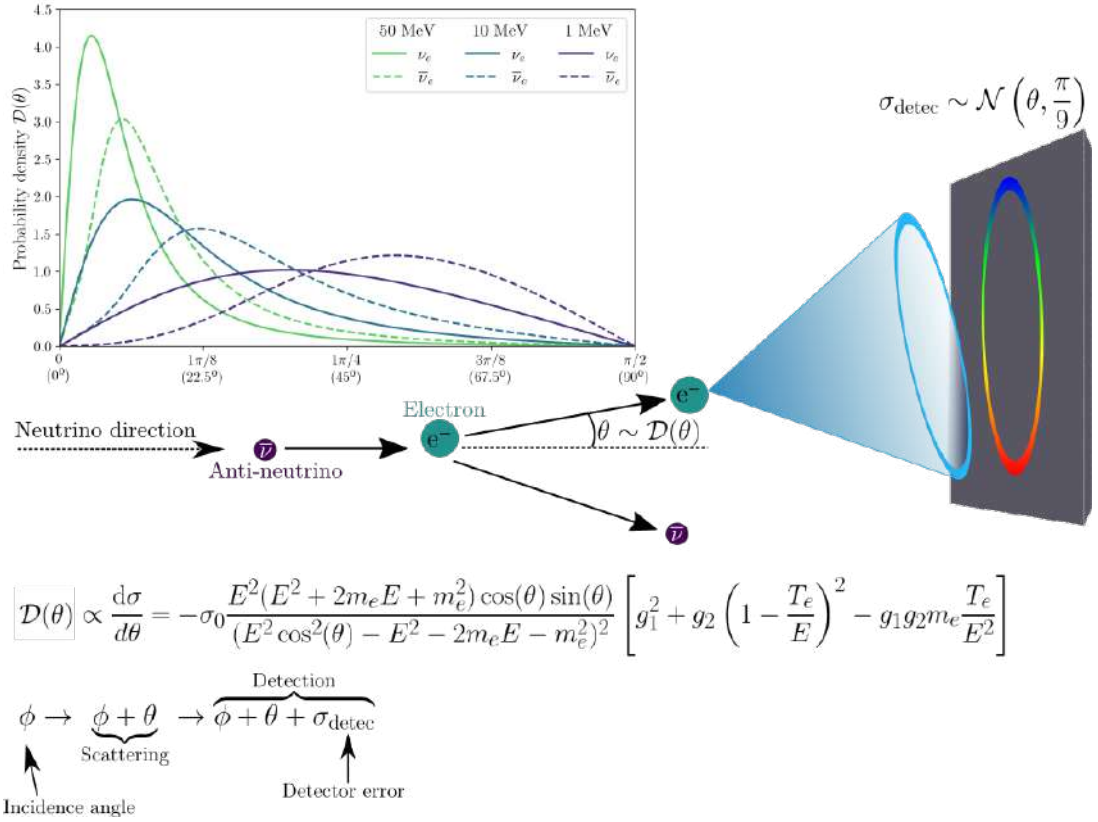

Figure 26 – Neutrino-electron scattering process and simulation. The electron scattering angle is a function of the neutrino energy and the probability distribution for the scattering angle is proportional to the angular cross section, shown in the top left corner. The detectors resolution is given by a normal distribution centered in the electron angle $\beta = \theta_\nu + \theta$ and has a standard deviation δ_θ that depends on the detector's resolution. The electron incoming angle is measured from the time delay observed in the projection of the Cherenkov cone on the detectors wall, depicted here in a color scheme similar to the one used by Super-K.

In our simulations of the angular spectrum in both water Cherenkov detectors (Super-K and Hyper-K) we use the sampled true neutrino energy to produce a probability distribution for a scattering angle θ that is given by the differential angular cross section

$$\mathcal{D}(\theta|E) = \frac{1}{N}\left|\frac{d\sigma}{d\theta}\right| = \frac{1}{N}\sigma_0 \frac{4E^2(m_e + E)^2\cos(\theta)\text{sen}(\theta)}{[(E(\cos(\theta) - 1) - m_e)^2(E(\cos(\theta) + 1) + m_e)^2]} \times \tag{5.12}$$
$$\times \left[g_1^2 + g_2^2\left(1 - \frac{T_e}{E}\right)^2 - g_1 g_2 m_e \frac{T_e}{E^2}\right],$$

where N is the normalization constant, $\sigma_0 = 88.06 \times 10^{-46}$ cm^2, g_1 and g_2 are dependent on the neutrino flavor (see table 3) and T_e is the electron recoil energy given in terms of the cosine of the scattering angle θ

$$T_e = \frac{2m_e E^2 \cos^2(\theta)}{(m_e + E)^2 - E^2 \cos(\theta)^2}. \tag{5.13}$$

Flavor	g_1	g_2
ν_e	$1/2 + \text{sen}(\theta_W)$	$\text{sen}(\theta_W)$
$\overline{\nu}_e$	$\text{sen}(\theta_W)$	$1/2 + \text{sen}(\theta_W)$
ν_x	$-1/2 + \text{sen}(\theta_W)$	$\text{sen}(\theta_W)$
$\overline{\nu}_x$	$\text{sen}(\theta_W)$	$-1/2 + \text{sen}(\theta_W)$

Table 3 – g_1 and g_2 values for neutrino-electron elastic scattering cross-sections with different neutrino flavors. $\text{sen}(\theta_W) = 0.2229$.

Since this probability distribution only states the magnitude of the scattering angle, not if it is positive or negative with respect to the neutrino direction, we add another random variable sampled from a uniform distribution from 0 to 1. If rand > 0.5 than $\beta = \theta_\nu + \theta$, where ϕ is the original neutrino incoming azimuth angle[2], and if rand < 0.5 than $\beta = \phi + (-\theta)$. On top of this, we include the detector's angular resolution again following a similar procedure to the one described in the energy sampling, we re-sample a new angle θ^{obs} from a normal distribution centered in β with standard deviation equal to Super-K's resolution of 26°

$$\theta^{\text{obs}} \sim \text{Normal}(\beta, \delta_\theta), \tag{5.14}$$

this process is squematically shown in figure 17.

With respect to all other channels we simply sample an azimuthal angle for the observed signal. Since the signal of these interactions is nearly isotropically, the addition of the detector's uncertainty does not affect the final angular distribution, thus we skip this step. One may guess that we need only sample a angle uniformly from 0 to π, yet this is not correct. The angular distribution is spherically uniform, thus a infinitesimal unit of area $\text{d}\Omega$ on the surface must include the same expected number of points, since $\text{d}\Omega = \text{sen}(\theta)\text{d}\theta\text{d}\varphi$, the probability that a point sampled lies on the infinitesimal solid angle defined by the area $\text{d}\Omega$ is $P(\Omega)\text{d}\Omega = P(\theta, \varphi)\text{d}\theta\text{d}\varphi$, following the normalization

$$\int_0^{2\pi} \int_0^{\pi} P(\Omega)\text{d}\Omega\text{d}\theta\text{d}\varphi = 1.$$

Since the surface of a unit sphere has area 4π, then $P(\Omega) = 1/4\pi$, then

[2] Super Kamiokande measures the neutrino direction using the azimuth as the origin axis. The nadir angle is directly mapped to the azimuthal angle $\theta_{\text{n}} = \theta_{\text{z}} - \pi/2$.

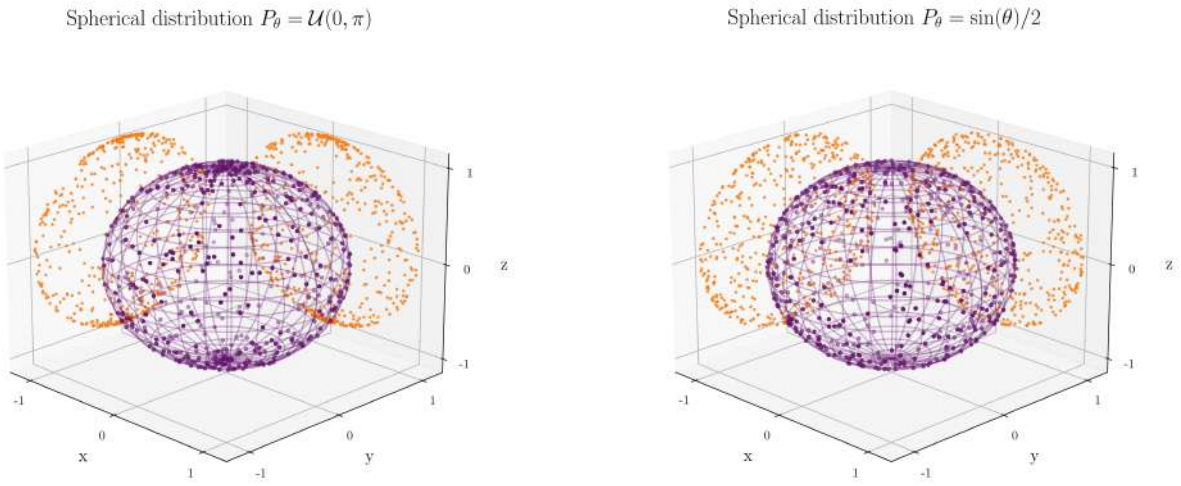

Figure 27 – Spherical distribution of points sampled following a uniform (left) and sinusoidal (right) distribution.

$$\frac{1}{4\pi}\text{sen}(\theta)\text{d}\Omega\text{d}\theta\text{d}\varphi = P(\theta,\varphi)\text{d}\theta\text{d}\varphi \Rightarrow P(\theta,\varphi) = \frac{\text{sen}(\theta)}{4\pi}, \tag{5.15}$$

and the probability distribution for θ uniformly distributed on the surface of a sphere is

$$P_\theta(\theta) = \int_0^{2\pi} P(\theta,\varphi)\text{d}\varphi = \frac{\text{sen}(\theta)}{2}. \tag{5.16}$$

We can visually see this result by comparing the spherical distribution of points sampled following $\theta \sim \mathcal{U}(0,\pi)$ and $\theta \sim \text{sen}(\theta)/2$ (figure 27), where we notice that if points are sampled from a uniform distribution in θ there is a higher concentration on the poles of the sphere.

The final angular spectrum is composed of events sampled from the isotropic interactions that can be considered a background and others that conserve the direction of the neutrino.

5.4.1 Super-Kamiokande

Considering all relevant statistical fluctuations in both the particle interaction process and the energy reconstruction, the final neutrino energy spectrum of a core collapse supernova, 10 kpc away, in Super-Kamiokande is shown in figure 28. The spectrum is displayed as a histogram with bin width equivalent to 2 times the width of the energy resolution at 50 MeV. The inverted mass hierarchy leads to an increase of electron antineutrino flux, resulting in a larger number of detected neutrinos by Super-K.

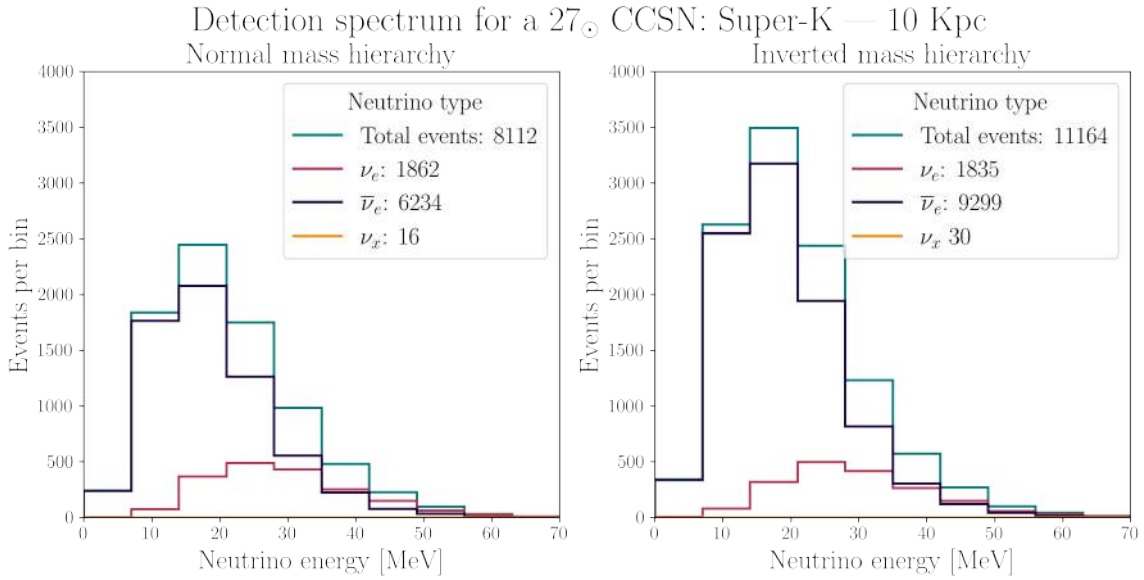

Figure 28 – Detected spectrum in Super-Kamiokande considering both normal (*left*) and inverted (*right*) mass hierarchies originated from a 27 $M_\odot$ CCSN near the galactic center, 10 kpc from Earth. For both cases we used the model LS220-27.0 of the Garching group.

5.4.2 Hyper-Kamiokande

Hyper-K has the same characteristics as its predecessor, therefore the spectrum assumes the same shape, although with less fluctuations due to the larger volume that allows a much higher number of events (Figure 29).

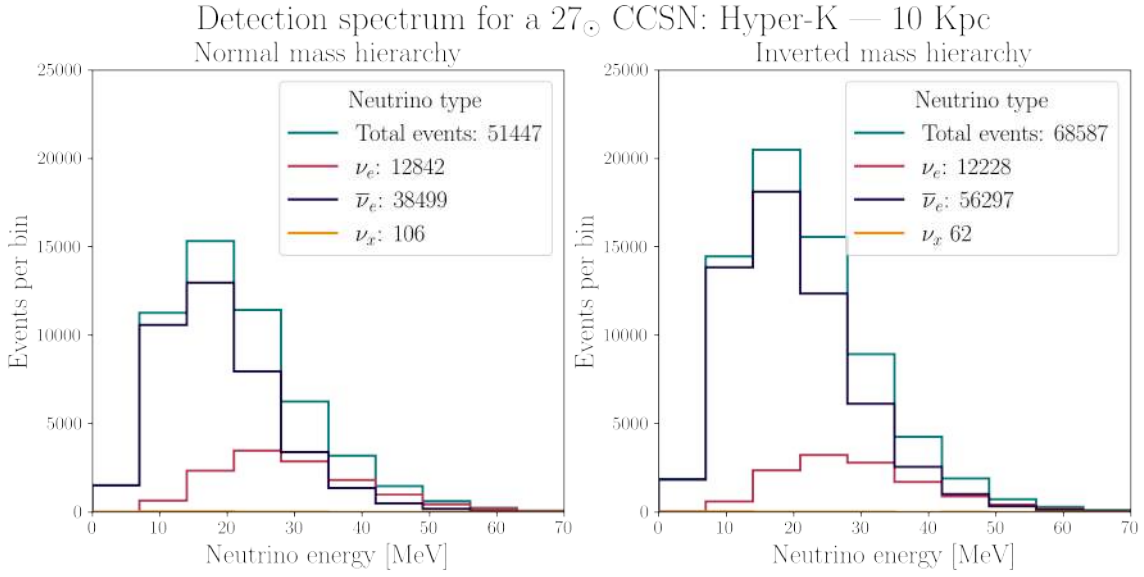

Figure 29 – Detected spectrum in Hyper-Kamiokande considering both normal (*left*) and inverted (*right*) mass hierarchies originated from a 27 $M_\odot$ CCSN near the galactic center, 10 kpc from Earth. For both cases we used the model LS220-27.0 of the Garching group.

5.4.3 DUNE

Regarding DUNE the energy spectrum is dominated by electron neutrinos, with a thinner bin width as a reflect to its larger energy resolution (Figure 30). The spectrum shape is not very affected by the neutrino mass hierarchy.

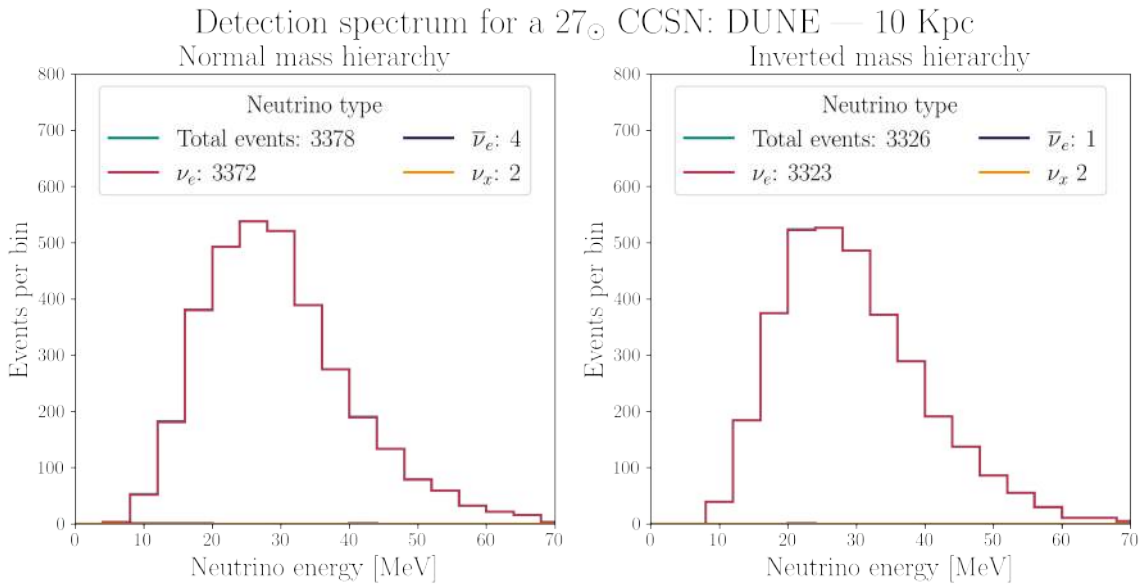

Figure 30 – Detected spectrum in DUNE considering both normal (*left*) and inverted (*right*) mass hierarchies originated from a 27 $M_\odot$ CCSN near the galactic center, 10 kpc from Earth. For both cases we used the model LS220-27.0 of the Garching group.

5.4.4 JUNO

Finally, JUNO is also dominated by electron antineutrinos, therefore it is also affected by neutrino mass hierarchy in the same way as Super/Hyper-K, it also has the thinner bin width among all detectors. However, due to its size, it is more subjected to stochastic fluctuations (31).

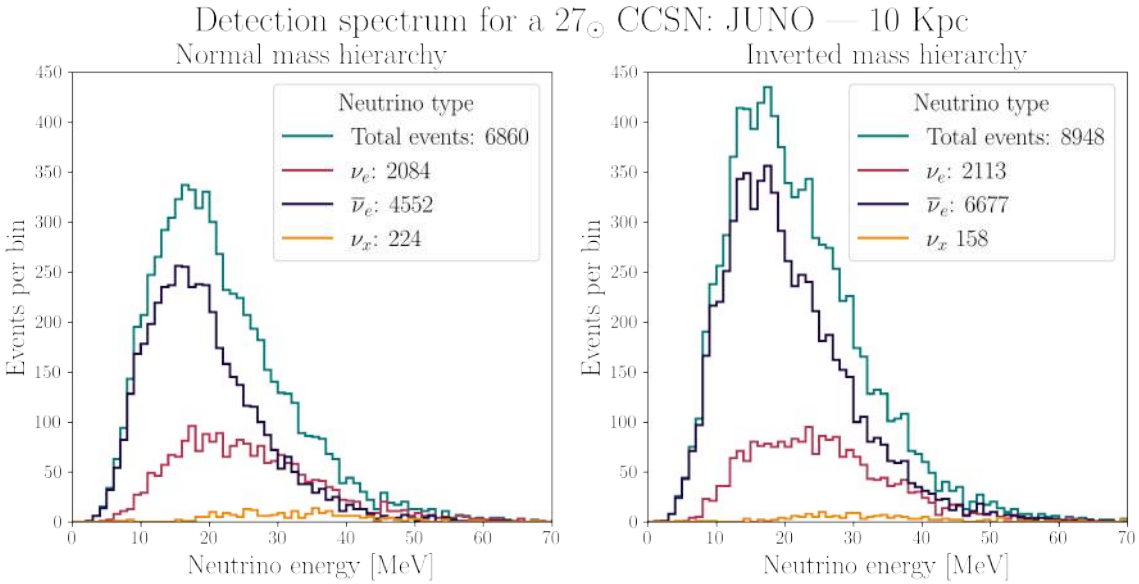

Figure 31 – Detected spectrum in JUNO considering both normal (*left*) and inverted (*right*) mass hierarchies originated from a 27 $M_\odot$ CCSN near the galactic center, 10 kpc from Earth. For both cases we used the model LS220-27.0 of the Garching group.

Part III

Simulation and Results

6 Supernova Distance

Here we present the simulation results concerning the reconstruction of the supernova distance from the detected spectrum of neutrinos.

What's another name for a supernova?
A POPstar.

Although many different aspects related to core collapse supernovae (CCSN) may be investigated from the detection of neutrinos, in this work we are particularly interested in trying to reconstruct the supernova distance and its direction in the sky. We now will focus first on the reconstruction of the distance.

As a way of investigating the method and the results in more detail, and providing a benchmark test, we first consider the case of a CCSN near the galactic center 10 kiloparsecs (kpc) away from Earth being detected by DUNE, assuming perfect resolution in neutrino energy reconstruction, that is the case where the width δ of the Gaussian around the energy E_ν is zero, thus neutrino energies are perfectly reconstructed from the detection of photons and charged leptons from interactions. We later address the effect of varying the distance on the reconstruction accuracy and the inclusion of a real resolution function.

6.1 Perfect resolution 10 kpc CCSN

For a 10 kpc CCSN, more than 3 thousand neutrinos are detected in a few seconds for the smallest detector (JUNO) and around 500 thousand for the largest one (Hyper-K). The time integrated flux, or energy spectrum, of the neutrinos detected are similar to the ones shown in figures 28 to 31 for all detectors. Once the data is obtained, the determination of the supernova distance from Earth requires three steps: First the parameters of pinch α and mean energy $\langle E_\nu \rangle$ must be determined, then the ratio L/D^2 is determined based on the integral of equations (5.7) and (5.9), given α and $\langle E_\nu \rangle$ known, and finally the distance D is achieved when considering constrains upon the luminosity L. Each of these steps will be carefully explained in the next paragraphs.

In order to obtain α and $\langle E_\nu \rangle$, it is necessary to fit the energy spectrum with equations (5.7) and (5.9) leaving α and $\langle E_\nu \rangle$ as free parameters to be fitted to the data. However, one may notice that this fit is not possible given that L and D are also unknowns. Therefore, we first normalize equations (5.7) and (5.9), and the energy spectrum, in order

to get rid of constants related to the scale of the spectrum, leaving α and $\langle E_\nu \rangle$ as the only unknown parameters. It is important to note that due to the smearing of the energy resolution, the observed spectrum is distorted accordingly to the resolution width δ of the detector, however as mentioned before, we will first consider the case where $\delta = 0$. Under this considerations, the equation for fitting the normalized energy spectrum is

$$\mathcal{F}^{\text{fit}}(E) = \frac{1}{N}\left(\frac{E}{\langle E \rangle}\right)^{\alpha} \exp\left(-\frac{(\alpha+1)E}{\langle E \rangle}\right)\sigma(E)\varepsilon(E)\mathrm{d}E, \tag{6.1}$$

where N is the normalization constant equal to the integral of $\mathcal{F}^{\text{fit}}$. In this equation, α and $\langle E \rangle$ are effective values that arise from the sum of all flavors, weighted by their luminosities and flavor mixing. Since we are dealing with the DUNE detector, $\sigma(E)$ is the sum of all cross-sections shown in figure 18.

Figure 32 shows the result of the fitting process after one sampling of detected energies following the procedure of 25, without the last step due to the perfect resolution assumption. The true values for α and $\langle E \rangle$ are 1.778 ± 0.002 and 12.667 ± 0.006[1], while fitted values were $\approx 1.8 \pm 0.2$ and 12.9 ± 0.5, yielding a excellent agreement between the parameters from a purely theoretical and continuous spectrum (True) and a more realistic binned spectrum with noise around the number of events.

[1] In order to estimate the true values for the pinch and the mean energy for each neutrino spectra, we considered a perfect detector ($\delta = 0$) and $D \approx 0.5$ kpc. This way, the statistical fluctuations became irrelevant compared to the sample size and $E^{\text{obs}} = E^{\text{True}}$. Thus, the shape of the neutrino spectrum is conserved.

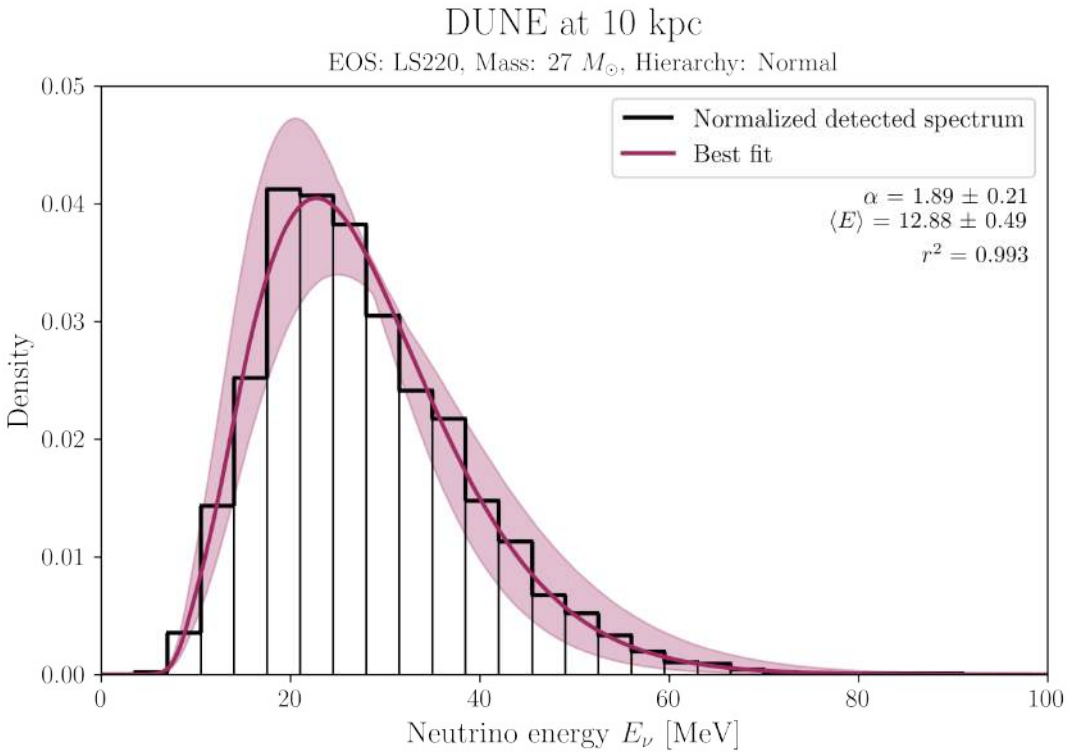

Figure 32 – Normalized detected neutrino spectrum in DUNE, assuming perfect resolution, and fitted curve from (6.1). Shaded area represent 95% confidence interval of the fitted curve, taken from the standard deviations in both parameters fitted.

With both parameters on hand, we proceed to determine the supernova distance. One may notice that it is not possible to extract the distance directly due to the L/D^2 factor that appears on the full description of the detection spectrum. However, L is directly related to the gravitational biding energy released by the supernova, which is related to the final size and mass of the neutron star [19].

$$L - \frac{GM_{\rm NS}^2}{R_{\rm NS}} \approx 3.6 \times 10^{53} \left(\frac{M_{\rm NS}}{1.5 M_\odot}\right)^2 \left(\frac{10{\rm km}}{R_{\rm NS}}\right) \text{ ergs.} \tag{6.2}$$

This relation implies in a tight constraint in the total luminosity of the supernova, given constraints in the neutron star mass and size. Rewriting the spectrum fitting equation, (explicitly stating N) we may isolate D

$$D = \sqrt{\frac{n_{\rm tot} L}{N_\nu^{\rm tot}} \int_0^\infty \left(\frac{E}{\langle E \rangle}\right)^\alpha \exp\left(-\frac{(\alpha+1)E}{\langle E \rangle}\right) \sigma(E)\varepsilon(E) dE}. \tag{6.3}$$

Our approach is then to build a probability distribution for L and use it alongside the fitted values of α and $\langle E \rangle$, and the observed number of detected neutrinos $N_\nu^{\rm tot}$ to achieve a probability distribution for D.

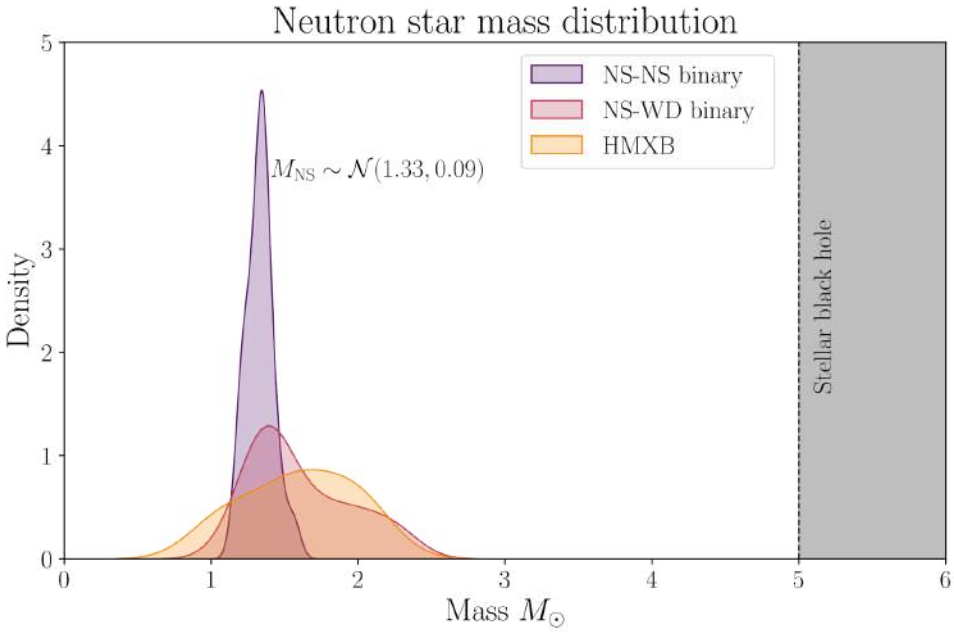

Figure 33 – Neutron star mass distribution according to binary type. Neutron Star-Neutron Star (NS-NS), Neutron Star-White Dwarf (NS-WD), High-Mass X-ray Binary (HMXB). This distribution was constructed using the dataset provided by ref [7].

Our task resumes to constructing L from M_{NS} and R_{NS}. The distribution of masses from neutron stars depends on the system in which they are found (figure 33), however neutron stars in NS-WD binary systems are typically in close orbit of their white dwarf companion, resulting in accretion of mass, inducing a larger mass in the neutron star as time progresses which would provoke biases to our estimation of the mass distribution right after birth (notice the long tail of the distribution in Figure 33). Neutron stars in high-mass X-ray binaries undergo a similar process and are also not useful for our purposes. The most precise distribution to characterize the mass of neutron stars right after birth is NS-NS binary systems, where it is expected that the neutron stars experience little to no accretion [95]. This type of binary has a mass distribution well described by a normal with $\mu = 1.33 M_\odot$ and $\sigma = 0.09 M_\odot$.

An alternative hypothesis is that slow spinning pulsars and recycled neutron stars have different mass distributions due to different mechanisms of explosion in the supernova, recent observations of the neutron star merge by LIGO seems to favor this hypothesis, although more data is needed to confirm it. Under this hypothesis, the best description is that recycled neutron[2] stars follow a two-gaussian distribution of the form

$$\pi(m|\{\mu_1, \sigma_1, \mu_2, \sigma_2, \alpha\}) = \frac{\alpha}{\sigma_1\sqrt{2\pi}} e^{-\frac{(m-\mu_1)^2}{2\sigma_1^2}} + \frac{1-\alpha}{\sigma_2\sqrt{2\pi}} e^{-\frac{(m-\mu_2)^2}{2\sigma_2^2}},$$

[2] More information the recycling of neutron stars during supernovae explosions may be found in ref [96].

where $\pi(m|\{\dots\})$ denotes the "probability distribution of m with parameters given by $\{\dots\}$", and $\mu_1 = 1.34M_\odot$, $\sigma_1 = 0.02M_\odot$, $\mu_2 = 1.47M_\odot$, $\sigma_2 = 0.15M_\odot$ and $\alpha = 0.68$. While slow spinning neutron stars follow a uniform distribution between 1.16 $M_\odot$ and 1.42 $M_\odot$ [97]. The full neutron star population is characterized by a bimodal mass distribution, ref [98] found Gaussian peaks at $\mu_1 = 1.35M_\odot$ (95% CI: 1.32 - 1.39) and $\mu_2 = 1.8M_\odot$ (95% CI: 1.6 - 2.4), with respective widths $\sigma_1 = 0.08$ (0.05 - 0.11) and $\sigma_2 = 0.3$ (0.2 - 0.6), and $\alpha = 0.7$ (0.5 - 0.8).

The mass distribution of gravitational wave neutron star or black hole-neutron star mergers from extragalatic sources appears to be inconsistent with the galactic neutron star distribution, with more high mass population [99]. To best of our knowledge this fact remains unexplained.

Since both descriptions (single and bimodal normal) result in distributions very similar and around the same intervals, we proceed by supposing that neutron stars distributions after birth assumes a normal distribution with $\mu = 1.33M_\odot$ and $\sigma = 0.09M_\odot$ as presented by ref [95]. Our next step is to find the correct size distribution for neutron stars after birth. Although measuring the radius of NS is a highly difficult task, with only a few measurements made, most with large uncertainties, there are limits to how big or how small the radius can be. Too small and the star becomes black hole or it's rotation violates causality, too big and the gravitational force is no longer capable of sustaining the star due to it's rotation and it falls apart. Thus, given a mass $M_{\rm NS}$, the radius of a neutron star must be confined to [100]

$$\frac{2.9GM_{\rm NS}}{c^2} \leqslant R_{\rm NS} \leqslant 10.4\left(\frac{1000}{716}\right)^{2/3} M_{\rm NS}^{1/3}, \tag{6.4}$$

thus we assume that the NS radius distribution is given in terms of the mass uniformly between $R_{\rm min}$ and $R_{\rm max}$, where

$$R_{\rm NS} \sim \mathcal{U}\left(R_{\rm min}, R_{\rm max}\right) = \mathcal{U}\left(\frac{2.9GM_{\rm NS}}{c^2}, 10.4\left(\frac{1000}{716}\right)^{2/3} M_{\rm NS}^{1/3}\right). \tag{6.5}$$

From these relations we may set approximate[3] constraints to the total luminosity distribution for the supernova $1\times10^{53} \leqslant L \leqslant 6\times10^{53}$ ergs, the distribution falls within the range of energies used in all four different simulations available in this work. We therefore assume a distribution for luminosity following equation (6.2), where the radii distribution follows and the mass distribution is given by $\mathcal{N}(1.33M_\odot, 0.09M_\odot)$. Thus

[3] The term approximate is used because (6.2) is a rough approximation for the total energy emitted in a supernova, considering both the progenitor star and the neutron star as hard spheres.

$$L \sim 3.6 \times 10^{53} \left(\frac{\mathcal{N}(1.33, 0.09)}{1.5} \right)^2 \left(\frac{10}{\mathcal{U}(R_{\min}, R_{\max}} \right). \tag{6.6}$$

Numerical simulations show a correlation between the progenitor mass and the total luminosity (Figure 34). Thus we may expect to achieve a better distribution if prior knowledge on the progenitor mass is known. If we assume that the supernova occurs for a well cataloged star, whose mass is already known, we may then use the correlation found in numerical simulations to determine a luminosity distribution following a normal with mean around the mean value of the linear regression between progenitor mass and L and standard deviation arbitrary chosen to be 0.3×10^{53} ergs, based on qualitative observations in the difference in total luminosity between the available simulations with different equations of state and progenitor masses.

The final scenario is the one where perfect knowledge around the value for the supernova total luminosity is acquired. Although not realistically possible, this approach serves as a benchmark to check if the resulting distribution for D will fall close to the true value D^{True}. This scenario also allows the investigation of the impact of α and $\langle E \rangle$ uncertainties on the final uncertainty in D, given that they are the only parameters affecting the resulting distribution for D under this assumption.

Using both approaches we finally achieve a probability distribution for the supernova distance (Figure 35) resulting in the value $D = 10$ kpc (95% CI: 8.8 - 11.3) supposing a perfect knowledge of the total luminosity, $D = 10.1$ kpc (95% CI: 7.3 - 12.5) in the scenario where the mass of the progenitor star is known and finally $D = 9.0$ kpc (95% CI: 7.4 - 12.8) while $D^{\text{True}} = 10$ kiloparsecs. Further replications of the same procedure reveals that, although the results for D vary due to the probabilistic nature of neutrino interactions, they always stay around the true value of 10 kpc.

These results might seem well expected since the only noise introduced in the data is in the number of events and the sampling process of neutrino energies, which results in a energy spectrum that resembles the theoretical prediction but discretized and with small fluctuations. However this is not so simple. α and $\langle E \rangle$ are indeed expected to be close to the true values. Still, D is not so. The true luminosity in simulations are a result of complex numerical methods, while we applied here the approximation of hard spheres for comparing the gravitational binding energy of the star and the NS remnant. This could very well prove to be a poor approximation in this scenario and yield a value for D with a big discrepancy. In order to investigate the robustness of this method, we will vary the true distance of the event and introduce the effects of a imperfect resolution in detectors. In the next session we explore both of this effects for all four detectors studied.

From figure 35 becomes clear that the distribution for L is the main source of uncertainty on estimating the distance from Earth to the supernova. Furthermore,

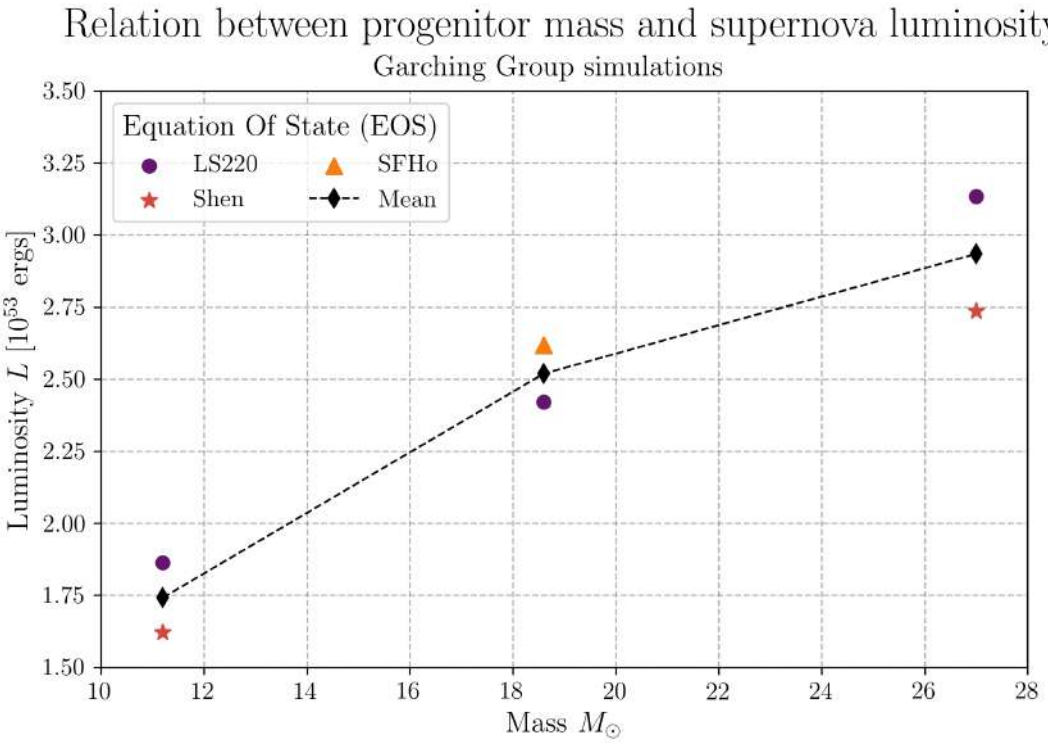

Figure 34 – Core collapse supernova progenitor mass and total luminosity in Garching group simulations. Note however that neither of the simulations in 18.6 $M_\odot$ were not considered in this study for now due to time schedule. The results of these simulations were recently obtained by request to the Graching group and thus these cases have not yet been included in the code for supernova detection and distance reconstruction.

knowledge of the progenitor star mass decreases little the width of the CI region, providing not much certainty. The impact of the knowledge on the progenitor star mass is in the point estimate for the distance, which becomes closer to D^{True}. From this point on, we will assume that this is always the case. This assumption is well justified given the long list of supernova candidates, such as Antares (11 - 14.3 $M_\odot$ [101]) and Betelgeuse (16.5 - 19 $M_\odot$ [102]), which provides information regarding the mass, location in celestial coordinates and sometimes even the distance of stars expected to become supernova[4]. If a star on this list goes through the CCSN process, the prior information in distance, mass and location may even provide ways of testing and ruling out models for equations of state using the neutrino signal. Even in the case where the star's mass is not previously known, multi-messenger observation including gravitational waves is capable of setting estimates for the progenitor mass, which are correlated to the gravitational waves amplitude [103, 104, 105].

[4] See https://en.wikipedia.org/wiki/List_of_supernova_candidates for a list of more than 30 supernova candidates.

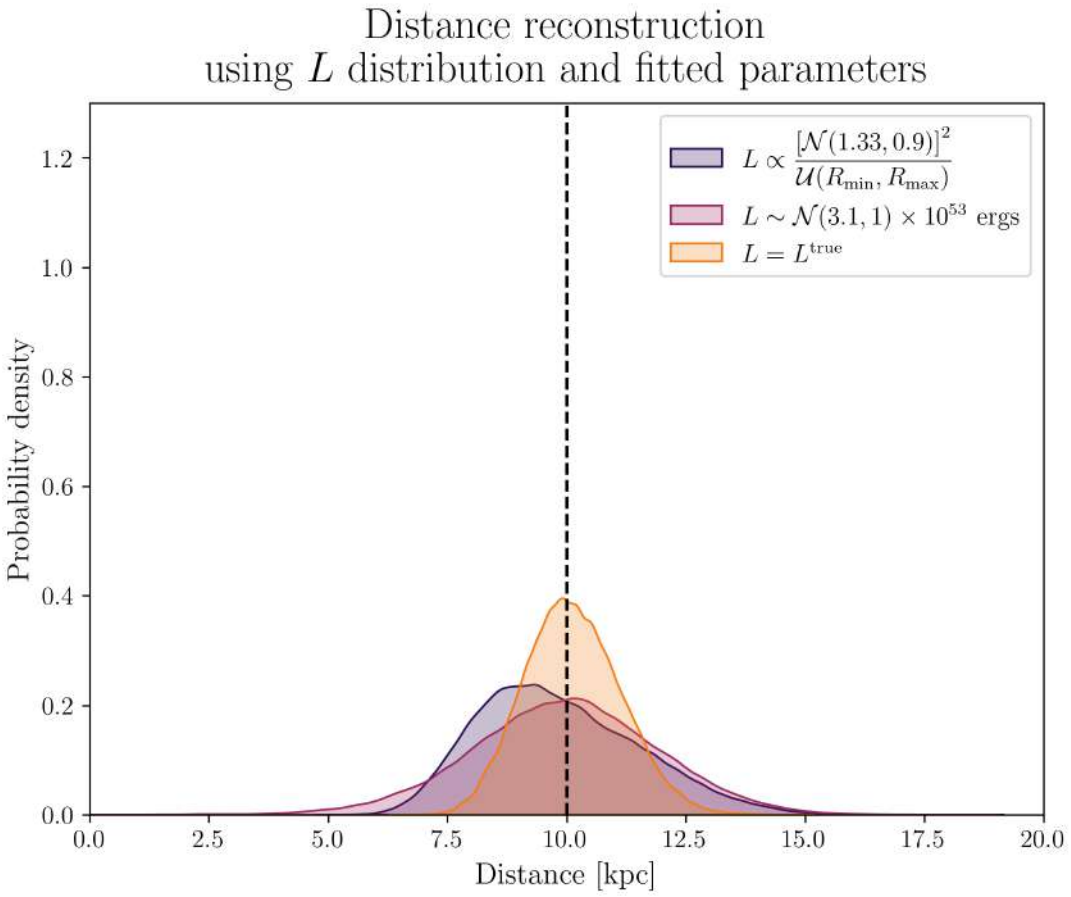

Figure 35 – Probability distributions for the distance between CCSN and Earth. The higher orange distribution considers perfect knowledge of the luminosity of the event, the width of the probability distribution arises purely from uncertainties in α and $\langle E \rangle$. The middle pink distribution considers that the progenitor mass is known and thus the luminosity distribution follows a normal around the expected value for a CCSN of this mass. The largest purple distribution assumes to prior knowledge of the progenitor star and uses the uniform distribution limited by the approximate constraints given by neutron star masses and radii.

6.2 Varying distance and real resolution

Sadly the world is not perfect and particle detectors have a limited capability for reconstructing the energy of incident particle that interacted and produced a signal. As discussed in chapter 5.4, the neutrino energy reconstructed falls within a region of probability given by a gaussian with mean around the true value of energy and standard deviation proportional to the resolution width of each detector. Such uncertainty means, in terms of simulations, that now we must produce the spectrum taking all steps discussed before and shown in 25. Figure 36 shows the effect of the resolution for the Super-Kamiokande observed energy spectrum with increasing width. In order to account for this effect when fitting the data, the spectrum should not be described by the neutrino true energy, but instead of the observed energy. This change of variables is represented as

$$\mathcal{F}^{\text{fit}}(E^{\text{obs}}) = \frac{1}{N}\int \left(\frac{E}{\langle E\rangle}\right)^{\alpha} \exp\left(-\frac{(\alpha+1)E}{\langle E\rangle}\right)\sigma(E)\varepsilon(E)\mathcal{R}(E^{\text{obs}};E,\delta)\mathrm{d}E, \tag{6.7}$$

where N is the normalization constant equal to the integral of $\mathcal{F}^{\text{fit}}$, in order get rid of the unnecessary constants mentioned above, and $\mathcal{R}(E^{\text{obs}};E,\delta)$ is the resolution function

$$\mathcal{R}(E^{\text{obs}};E,\delta) = \frac{1}{\delta\sqrt{2\pi}}\exp\left[-\frac{1}{2}\left(\frac{E^{\text{obs}}-E}{\delta}\right)^2\right]. \tag{6.8}$$

Given that the detector's resolution is known, this procedure does not change the number of free parameters to be fitted. In this equation, α and $\langle E\rangle$ are effective values that arise from the sum of all flavors, weighted by their luminosities and flavor mixing. Nonetheless, as one may observe in figure 36, for the distortion to be pronounced the width of the resolution must be much higher than the actual values for all detectors considered here. The detector with the largest width is Super/Hyper-K, which is represented by the darker histogram in figure 36, barely resembling difference than to the perfect detector scenario (dashed black line).

Both spectrum parameters were fitted using ordinary Least-Squares method and considering a 27 solar mass supernova with normal mass hierarchy while varying the distance D between the supernova and Earth (see figures 41 and 42 in appendix A). For each D, 5 samplings of the detection spectrum were made, in each of them the fitted values for α and $\langle E\rangle$ yield a best fit and a standard deviation, the final confidence intervals of 1, 2 and 3 sigmas are built from the combined distribution using the best fits and standard deviations of all 5 attempts. The true values were computed using the theoretical spectrum and fitting it with equation (6.7).

For JUNO, the pinch uncertainty stays within a 20% variation of the true value at a 2σ level up to 10 kpc, while 3σ level is achieved up to 7 kpc and 1σ up to 30 kpc. The mean energy is better determined, with a 20% deviation from the true value falling inside the 3σ region up until $D \approx 32$ kpc, and 2σ until close to 50 kpc. In contrast DUNE presents a far more increasing uncertainty as distance increases, already passing 20% of the true value for α at 1 kpc at the 2σ level, and passing this threshold in $\langle E\rangle$ when $D \gtrsim 12$ kpc at the 2σ level and $D \gtrsim 7$ kpc at 3σ. Similarly to DUNE, Super-K passes the 20% threshold from the true value at the 2σ level already in $D = 1$ kpc, however its uncertainty does not increase as much as DUNE's does with larger distances. On the other hand, the average energy fitting performs much better, crossing the 20% threshold at 3σ close to 20 kpc and at 2σ close to 30 kpc. Finally, Hyper-K performed better than all other detectors for $\langle E\rangle$ and had a similar result to JUNO in α at 1σ level, but its uncertainty quickly grew to more than 20% of the true value at 2 and 3 σs. Table 4 shows the summary of

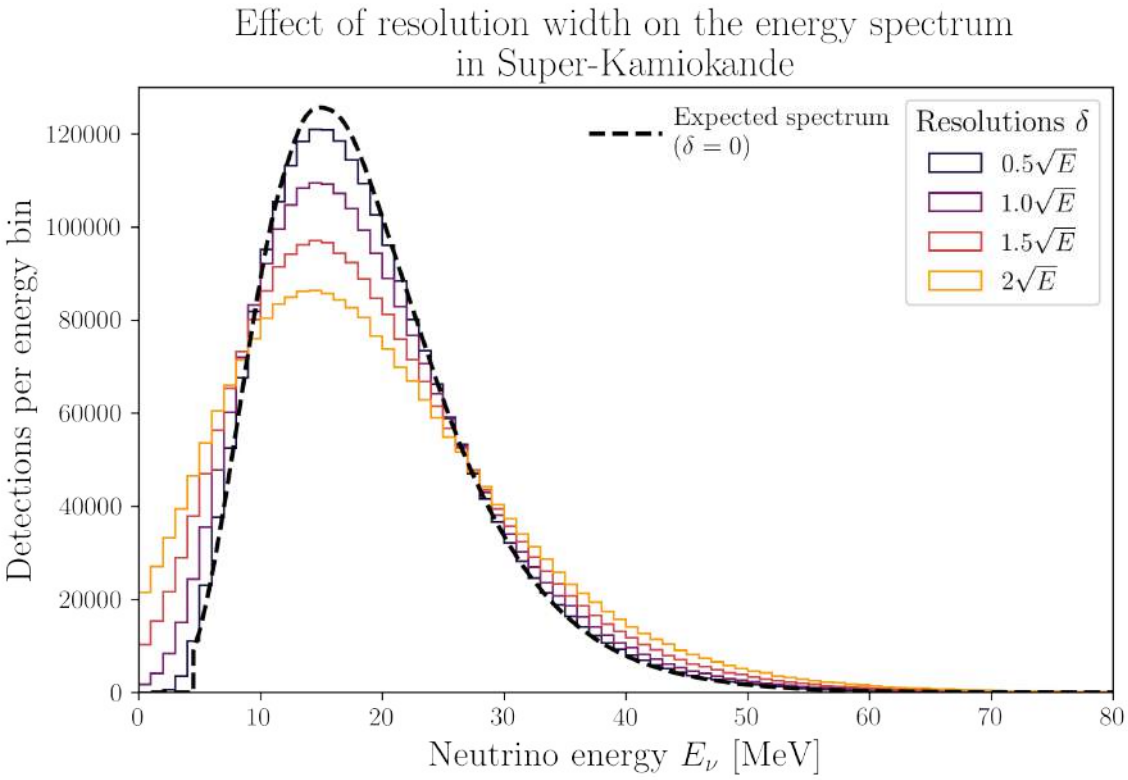

Figure 36 – Effect of the resolution width in the detected spectrum shape. Larger resolutions yield a higher kurtosis for the spectra due to the gaussian smearing effect.

these results, depicting the maximum distance in which the confidence levels of 1, 2 and 3 σ falls within 20% variation from the true value for each parameter.

Pinch α	1σ	2σ	3σ
DUNE	4 kpc	1 kpc	1 kpc
JUNO	20 kpc	12 kpc	10 kpc
Super-K	14 kpc	1 kpc	1 kpc
Hyper-K	22 kpc	1 kpc	1 kpc
Average Energy $\langle E \rangle$	1σ	2σ	3σ
DUNE	20 kpc	8 kpc	8 kpc
JUNO	48 kpc	42 kpc	32 kpc
Super-K	28 kpc	20 kpc	16 kpc
Hyper-K	70 kpc	64 kpc	36 kpc

Table 4 – Maximum distance until parameters distributions confidence levels reach more than 20% variation from the true value. Top three rows shows these maximum distances for the pinch parameter α and the lower three are related to the average energy $\langle E \rangle$.

Following the procedure described in the last section, we then compute the distance probability distribution for each of the five samplings and build a final distribution composed of all 5 probability distributions, in order to access the width of the uncertainty

behavior as the true distance increases D^{True}. Figure 37 shows the reconstructed distance probability distribution for each detector, with the true CCSN distance varying from 1 to 100 kpc. Due to its lower mass and large vulnerability to statistical fluctuations, aligned with a thin bin width, DUNE presents the largest increase in uncertainty as distance increases, for a supernova located at the galactic center at 8 kpc, the distance reconstructed by DUNE using the binned spectrum and a least-squares fitting algorithm for finding α and $\langle E \rangle$ is $D^{\text{rec}} = 8.5^{11.9}_{4.9}$ kpc at a 2σ confidence interval (CI). The CI increases largely with distance, for the same supernova located at the edge of the galaxy diametrically opposed to Earth, at 18 kpc, $D^{\text{rec}} = 18.3^{28.5}_{10.3}$. In the first scenario the 2σ CI band extends to approximately 40% of the estimated value[5], while in the second case the band extends to 50%. The precise analysis for all other detectors may be found in table 5. Super-K, although not much larger than DUNE or JUNO, have a much wider bin width (due to its poorer resolution) which diminishes the statistical fluctuation effect and more consistent estimates for the distance. Hyper-K, being the largest of all, provides the best reconstruction ability for CCSN distances, specially the ones outside galactic domain such as the Large Megallanic Cloud and other satellite galaxies.

Galactic center (8 kpc)	median (kpc)	1σ (kpc)	2σ (kpc)	3σ (kpc)
DUNE	8.5	6.2 - 10.3	4.9 - 11.9	4.2 - 13.7
JUNO	8.4	6.3 - 10.2	5.1 - 11.1	4.6 - 11.7
Super-K	8.4	6.3 - 10.2	5.1 - 11.3	4.6 - 11.9
Hyper-K	8.3	6.1 - 10.1	5.0 - 11.2	4.6 - 118
Galaxy edge (18 kpc)	median (kpc)	1σ (kpc)	2σ (kpc)	3σ (kpc)
DUNE	18.3	13.3 - 23.4	10.3 - 28.5	7.4 - 36.1
JUNO	18.9	14.1 - 22.7	11.4 - 25.0	10.2 - 26.2
Super-K	18.9	14.1 - 23.0	11.5 - 25.6	10.2 - 27.2
Hyper-K	19	14.0 - 22.9	11.4 - 25.0	10.3 - 26.8
LMC (48 kpc)	median (kpc)	1σ (kpc)	2σ (kpc)	3σ (kpc)
DUNE	55.0	34.5 - 78.1	11.2 - 128.4	4.0 - 697.9
JUNO	52.4	38.7 - 63.6	31.5 - 71.9	26.6 - 78.8
Super-K	49.7	36.3 - 62.7	27.7 - 72.4	20.0 - 96.9
Hyper-K	50.3	37 - 60.9	30.2 - 67.1	27.4 - 72.7

Table 5 – Confidence intervals at 1, 2 and 3 σ levels for D^{red} in each detector in cases of two galactic CCSN and one extra galactic CCSN (Large Megallanic Cloud [LMC]).

[5] $|8.5 - 4.9|/8.5 \approx |8.5 - 11.9|/8.5 \approx 0.4$

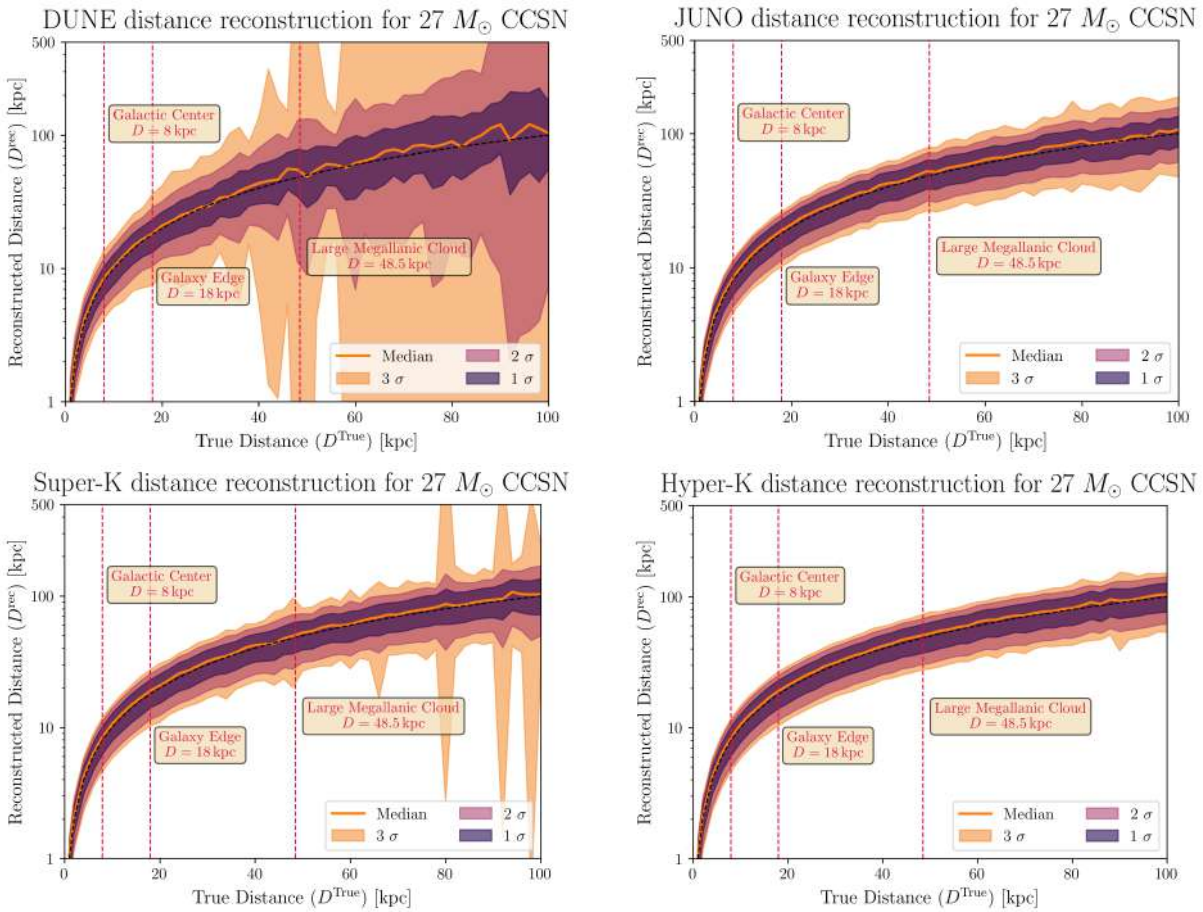

Figure 37 – Distance reconstruction from detection spectrum and knowledge on the progenitor mass for all four detectors (DUNE - *top left*, JUNO - *top right*, Super-Kamiokande - *bottom left* and Hyper-Kamiokande - *bottom right*). Each dashed red line serves as an indication for a "landmark" to provide a sense for how far are the distances.

7 Supernova Direction

In this chapter we show the simulation results concerning the reconstruction of the supernova direction from the detected neutrinos.

A neutrino walks into a bar . . .
and keeps right on going.

In the previous chapter we assessed the ability for neutrino detectors to recover the supernova distance purely from the energy spectrum and previous knowledge on the total luminosity of the event. Now we turn our attention to the direction of this event. Since the neutrino signal precedes the photons in some hours or even days, they become the first source of assessment of a core collapse supernova direction. Even more, the light interacts with matter much more commonly than neutrinos, so astronomical objects such as stars, and dust might cover the supernova behind it, diminishing the light signal or maybe even covering it completely depending on size and distance.

In this chapter we will use Hyper-Kamiokande as a study object to create the angular spectrum of neutrinos[1]. However, the methods shown here are applicable to any detector in which the direction of neutrinos may be inferred, such as DUNE. Following the same format of the previous chapter, we begin with a simplification of the system to dive more deeply and provide a benchmark of the method, therefore we start assuming again a perfect detector in energy and angle reconstruction, meaning that δ_θ and δ are both zero. We also begin the explanation of the method by considering only electron-neutrino elastic scattering events, then we add IBD and ^{16}O interactions that produce an almost isotropic background and finally consider the effect of distance and resolution on the results.

7.1 Perfect resolution 10 kpc CCSN

In the case of a 10 kpc core collapse supernova detected by Hyper-Kamiokande, we expect 39664 neutrinos by inverse beta decay, 13083 neutrinos by ν^{16}OCC and 645 neutrino-electron elastic scattering events. Therefore, most of the events detected compose the isotropical noise.

The neutrino interaction and scattering process follows the procedure indicated in figure 26 and section 5.4. The final likelihood for the scattering angle θ, given a neutrino interaction with energy E_ν is written as

[1] The spectrum between Hyper-K and Super-K are expected to be the same, since both use the same technology and differ only in size. Given that we will vary the distance of the supernova and the detector, we will already include variations in the total number of events, thus we only work with Hyper-K in this part to avoid redundancy.

$$F_\theta(\theta|E_\nu) = P_{\text{ES}}(E_\nu)\mathcal{D}(\theta, E_\nu) + [1 - P_{\text{ES}}(E_\nu)]\, F_u(\theta), \tag{7.1}$$

where $F_u(\theta) = \text{sen}(\theta)/2$ and P_{ES} is the probability of the interaction occurring via νeES. This probability may be found by comparing the νeES cross section with the total interaction cross section. Therefore,

$$P_{\text{ES}}(E_\nu) = \frac{\sigma_{\text{ES}}(E_\nu)}{\sigma_T(E_\nu)} = \frac{\sigma_{\text{ES}}(E_\nu)}{\sum_{i=1}^{K} \sigma_i(E_\nu)}.$$

Since the neutrino incoming angle $\phi = \theta_\nu$[2] and the scattering angle θ are related by $\beta = \theta + \phi$ we may directly compute the likelihood probability for the neutrino incoming azimuthal angle ϕ by

$$P_\phi(\phi) = \int \delta(\phi - \beta + \theta) F_\beta(\beta|E\nu) F_\theta(\theta|E\nu) P_{E_\nu}(E_\nu) \mathrm{d}\beta \mathrm{d}\theta \mathrm{d}E_\nu = \tag{7.2}$$

$$= \int F_\beta(\beta|E_\nu) F_\theta(\beta - \phi|E_\nu) P_{E_\nu}(E_\nu) \mathrm{d}E_\nu \mathrm{d}\beta. \tag{7.3}$$

In this case, we have the distribution $F_\beta(\beta|E)$ from the final data and we marginalize the distribution by the energy in order to achieve dependence only on the angle ϕ.

Under this framework, we investigate four possibilities:

- In the first one we assume that from all detections, we can perfectly separate the elastic scattering events (thus $P_{\text{ES}} = 1$, $\forall E$) and we use only events with detected energy around 10 MeV. This procedure is a way of having a fairly monoenergetic dataset, removing the necessity for the integral in energy in equation (7.3).
- The second approach still relies on the assumption of perfect separation between ES events and non-ES events, but using the totality of the data.
- The third approach uses both ES and non-ES events, but excludes IBD events that were able to be tagged ($\approx 90\%$) and truncates the dataset at energies below 20 MeV in order to eliminate the region where $P_{\text{ES}} \approx 0$ (see figure 16, notice how for larger E, the higher other cross sections get compared to ES).
- Finally, the final case does not implement the energy truncation, but still exclude the tagged IBD events.

[2] From now on we will denote ϕ for the neutrino incoming angle, instead of θ_ν, to avoid the confusion with the scattering angle θ in the equations that follow.

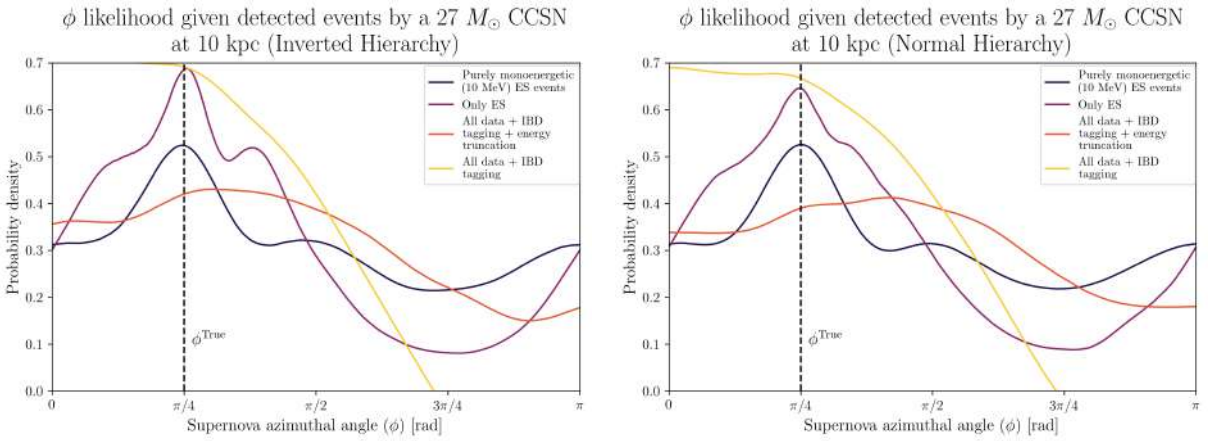

Figure 38 – Likelihood for the supernova direction given by ϕ. *Left*: Inverted mass hierarchy. *Right*: Normal mass hierarchy.

Figure 38 displays the result for $P_\phi(\phi)$, from 0 to π, for all four scenarios, considering a 10 kpc CCSN, both in normal and inverted hierarchy. The results are not dramatically affected by neutrino mass hierarchy. In both of them we observe that the use of the full dataset of detection events yields a probability distribution for ϕ that presents no clear peak. By using ES events only, there is a pronounced peak at the true zenith angle, however the distribution still have long tails, yielding large confidence intervals.

This is further observed in the skymap of the supernova direction reconstruction (Figure 39) where we simulated a supernova coming from the direction of the Large Megallanic Cloud, although closer, being detected at the same day SN1987 was. Although the best-fit region is tightly located containing the true location the 68% CI already covers half of the sky, and 95% and 99% fills almost the whole skymap, except for the region in the opposite direction as the one indicated by the best-fit. According to these results, Hyper-K would be at 68% confidence be able to distinguish a hemisphere where the supernova could have happened, and at 95% and 99% confidence it would at best be able to tell where the supernova did not come from.

Although this is a poor resolution for a galactic supernova, in a scenario where neutrinos arrive before photons, any information provided is useful for observatories that rely on light. Furthermore, the process of pinpoiting the supernova location may be farther improved by using the position of multiple detectors and their detection time to triangulate the supernova position in the sky, as shown in [106].

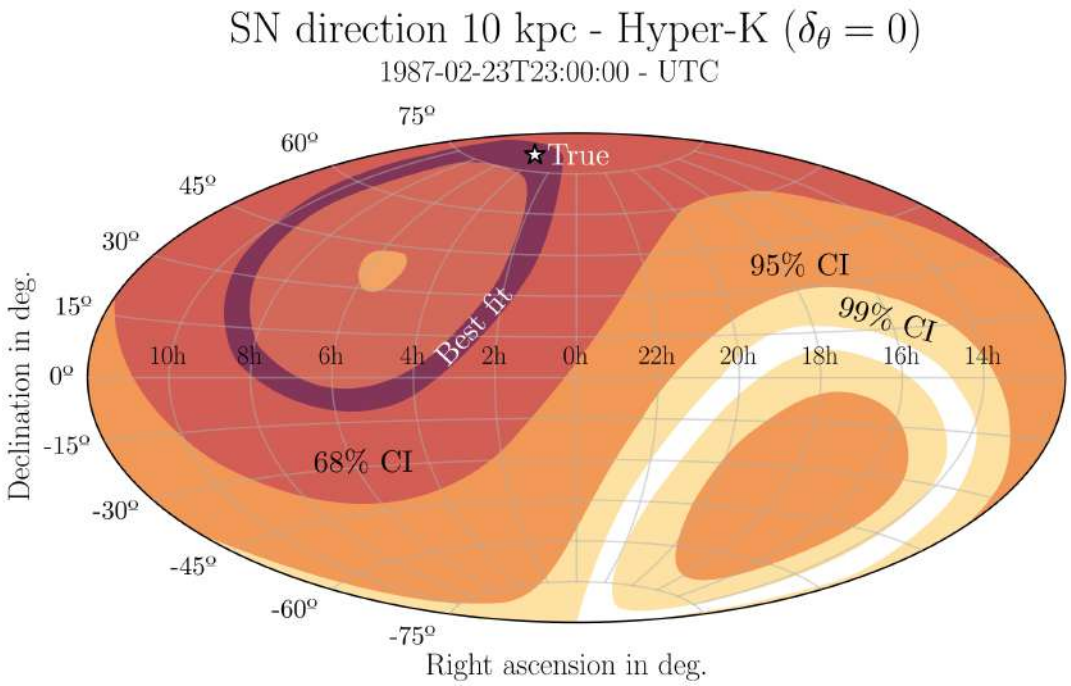

Figure 39 – Skymap in celestial coordinates for the reconstructed supernova direction using the dataset described in scenario 2 (only ES events) and normal mass hierarchy. $\delta_\theta = 0$ means that the width of the resolution function is zero, which implies in the direction of the charged lepton resulting from an interaction being determined with 100% accuracy.

7.2 Varying distance

Again, as in chapter 6 we consider the case where the distance from the supernova varies. One might notice that we are not presenting results for when the detectors energy and angular resolution is not perfect. We decide not to include these results as a way of isolating the effect of distance in the probability distribution for ϕ.

In order to evaluate the isolate effect of the distance, we built the probability distribution for ϕ under the second assumption of perfect separation between ES and non-ES events. The probability distribution is not considerably changed when the supernova distance is below 20 kpc (Figure 40), thus we can expect that the supernova direction is not better reconstructed by this method even if the supernova occurs in distances closer to Earth. The noise introduced by the large uncertainty on the energy of each incoming neutrino by Hyper-K and the variability in the scattering angles due as a result of the angular cross-section, seems to be larger than the fluctuations introduced by the events sample size.

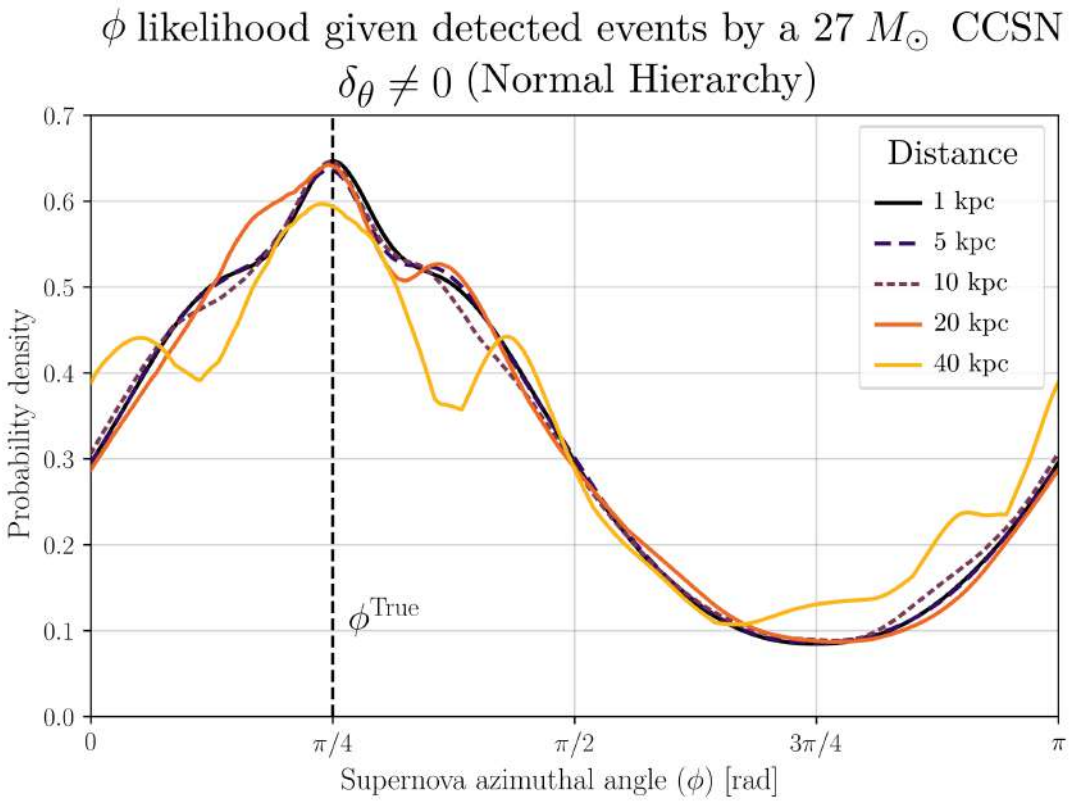

Figure 40 – Likelihood for ϕ under the assumption of perfect separation of ES and non-ES events (scenario 2). In this case $\delta_\theta \neq 0$.

8 Conclusions

In this work, we studied the process of supernova detection using neutrinos. We show the distance and direction of the explosion event might be reconstructed by both current and next generation detectors, and assessed the ability to reconstruct the direction of a supernova using only elastic-scattering events in a water Cherenkov detector.

According to our simulations, the neutrino energy spectra that reaches a detector is not considerably changed when varying the nadir angle in which the neutrino arrives at Earth. When considering the capacity for reconstructing the supernova distance, Hyper-K performs the best due to its large mass, making it less subjected to the statistical fluctuations behind the neutrino interaction. In the case where the supernova occurs inside the Milky Way galaxy, all detectors have capacity for obtaining its direction; meanwhile if the supernova occurs outside the Milky Way, as it was the case of SN1987, DUNE and Super-Kamiokande have large uncertainties and lose their ability to provide a reliable estimate for the distance. Our simulations show that in fact, the constraints on the total luminosity of a supernova make it possible to obtain the distance from the observed neutrino spectrum. Moreover, if the distance is also obtained from the electromagnetic spectrum, both approaches may be compared to input constraints in supernova models and equations of state for neutron stars.

Upon investigation of the possible use of neutrino elastic-scattering events for reconstructing the direction of the supernova, we found large uncertainties and wide probability distributions, resulting in regions in the skymap that cover almost the entire sky. We conclude that the neutrino elastic-scattering channel is not a reliable source alone to use as measurement of a supernova direction in Hyper-Kamiokande.

Furthermore, we developed a python code fully open source that might be used by the community. It is in our goal to turn this code into a python library, freely available. This initiative adds to existing ones of creating an scientific library for astroparticle physics in Python, such as SNEWPY), bringing the programming language closer to new generations of scientists.

Further work may improve the generalization of the results by considering neutrino collective effects, a wider range of supernova models and maybe new physics that might affect the detection spectrum. This last steps are part of an ongoing project to explore various different aspects of the neutrino burst of a core collapse supernova and the amount of information that might be acquired by observing such an event.

Bibliography

[1] Kippenhahn, R., Weigert, A. & Weiss, A. *Stellar structure and evolution*, vol. 192 (Springer, 1990). Citado 2 vezes nas páginas 11 and 27.

[2] Spurio, M., Spurio & Bellantone. *Probes of Multimessenger Astrophysics* (Springer, 2018). Citado 3 vezes nas páginas 11, 27, and 28.

[3] Mirizzi, A. *et al.* Supernova neutrinos: production, oscillations and detection. *La Rivista del Nuovo Cimento* **39**, 1–112 (2016). URL https://doi.org/10.1393/ncr/i2016-10120-8. Citado 4 vezes nas páginas 12, 28, 42, and 71.

[4] Dighe, A., Kachelriess, M., Raffelt, G. & Tomas, R. Signatures of supernova neutrino oscillations in the earth mantle and core. *Journal of Cosmology and Astroparticle Physics* **2004**, 004 (2004). URL https://doi.org/10.1088/1475-7516/2004/01/004. Citado 3 vezes nas páginas 12, 52, and 57.

[5] Scholberg, K., Albert, J. B. & Vasel, J. Snowglobes: Supernova observatories with globes. *Astrophysics Source Code Library* ascl–2109 (2021). Citado 4 vezes nas páginas 13, 61, 66, and 69.

[6] Giunti, C. & Kim, C. W. *Fundamentals of neutrino physics and astrophysics* (Oxford university press, 2007). Citado 2 vezes nas páginas 13 and 63.

[7] Shao, D.-S., Tang, S.-P., Jiang, J.-L. & Fan, Y.-Z. Maximum mass cutoff in the neutron star mass distribution and the prospect of forming supramassive objects in the double neutron star mergers. *Physical Review D* **102**, 063006 (2020). URL https://doi.org/10.1103/PhysRevD.102.063006. Citado 2 vezes nas páginas 15 and 90.

[8] Guetta, D., Hooper, D., Alvarez-Muniz, J., Halzen, F. & Reuveni, E. Neutrinos from individual gamma-ray bursts in the batse catalog. *Astroparticle Physics* **20**, 429–455 (2004). URL https://doi.org/10.1016/S0927-6505(03)00211-1. Citado na página 22.

[9] Murase, K. & Nagataki, S. High energy neutrino emission and neutrino background from gamma-ray bursts in the internal shock model. *Physical Review D* **73**, 063002 (2006). URL https://doi.org/10.1103/PhysRevD.73.063002. Citado na página 22.

[10] Habig, A. & Scholberg, K. The supernova early warning system. *Nature Reviews Physics* **2**, 458–460 (2020). URL https://doi.org/10.1038/s42254-020-0221-5. Citado na página 22.

[11] Lin, Z. & Lunardini, C. Observing cosmological binary mergers with next generation neutrino and gravitational wave detectors. *Physical Review D* **101**, 023016 (2020). URL https://doi.org/10.1103/PhysRevD.101.023016. Citado na página 22.

[12] Turatto, M. Classification of supernovae. In *Supernovae and Gamma-Ray Bursters*, 21–36 (Springer, 2003). Citado na página 22.

[13] Chin, Y.-N. & Huang, Y.-L. Identification of the guest star of ad 185 as a comet rather than a supernova. *Nature* **371**, 398–399 (1994). URL https://doi.org/10.1038/371398a0. Citado na página 24.

[14] Zhao, F.-Y., Strom, R. & Jiang, S.-Y. The guest star of ad185 must have been a supernova. *Chinese Journal of Astronomy and Astrophysics* **6**, 635 (2006). URL https://doi.org/10.1088/1009-9271/6/5/17. Citado na página 24.

[15] Stothers, R. Is the supernova of ad 185 recorded in ancient roman literature? *Isis* **68**, 443–447 (1977). URL https://doi.org/10.1086/351822. Citado na página 24.

[16] Wang, Z., Qu, Q.-Y. & Chen, Y. Is rx j1713. 7-3946 the remnant of the ad393 guest star? *Astronomy and Astrophysics* **318**, L59–L61 (1997). URL https://adsabs.harvard.edu/full/record/seri/A%2BA../0318/1997A%26A...318L..59W.html. Citado na página 24.

[17] Mayall, N. U. The crab nebula, a probable supernova. *Leaflet of the Astronomical Society of the Pacific* **3**, 145 (1939). URL https://adsabs.harvard.edu/full/1939aspl....3..145m. Citado na página 24.

[18] Lundmark, K. Suspected new stars recorded in old chronicles and among recent meridian observations. *Publications of the Astronomical Society of the Pacific* **33**, 225–238 (1921). URL https://doi.org/10.1086/123101. Citado na página 24.

[19] Shapiro, S. L. & Teukolsky, S. A. *Black holes, white dwarfs, and neutron stars: The physics of compact objects* (John Wiley & Sons, 2008). Citado 2 vezes nas páginas 24 and 89.

[20] Lada, C. J. & Lada, E. A. Embedded clusters in molecular clouds. *Annual Review of Astronomy and Astrophysics* **41**, 57–115 (2003). URL https://doi.org/10.1146/annurev.astro.41.011802.094844. Citado na página 25.

[21] Zhang, G.-Y., André, P., Men'shchikov, A. & Wang, K. Fragmentation of star-forming filaments in the x-shaped nebula of the california molecular cloud. *Astronomy & Astrophysics* **642**, A76 (2020). URL https://doi.org/10.1051/0004-6361/202037721. Citado na página 25.

[22] Jain, P. *An introduction to astronomy and astrophysics* (CRC Press, 2016). Citado na página 26.

[23] Vanbeveren, D., De Loore, C. & Van Rensbergen, W. Massive stars. *The Astronomy and Astrophysics Review* **9**, 63–152 (1998). URL https://doi.org/10.1007/s001590050015. Citado na página 26.

[24] Woosley, S. E., Heger, A. & Weaver, T. A. The evolution and explosion of massive stars. *Reviews of modern physics* **74**, 1015 (2002). URL https://doi.org/10.1103/RevModPhys.74.1015. Citado na página 27.

[25] Janka, H.-T. Neutrino emission from supernovae. *arXiv preprint* (2017). URL https://doi.org/10.1007/978-3-319-21846-5_4. Citado 2 vezes nas páginas 28 and 41.

[26] Burrows, A. & Vartanyan, D. Core-collapse supernova explosion theory. *Nature* **589**, 29–39 (2021). URL https://doi.org/10.1038/s41586-020-03059-w. Citado 2 vezes nas páginas 28 and 29.

[27] Bethe, H. A. Supernova mechanisms. *Reviews of Modern Physics* **62**, 801 (1990). URL https://doi.org/10.1103/RevModPhys.62.801. Citado na página 28.

[28] Pascal, A., Novak, J. & Oertel, M. Proto-neutron star evolution with improved charged-current neutrino–nucleon interactions. *Monthly Notices of the Royal Astronomical Society* **511**, 356–370 (2022). URL https://doi.org/10.1093/mnras/stac016. Citado na página 30.

[29] Brdar, V., Lindner, M. & Xu, X.-J. Neutrino astronomy with supernova neutrinos. *Journal of Cosmology and Astroparticle Physics* **2018**, 025 (2018). URL https://doi.org/10.1088/1475-7516/2018/04/025. Citado na página 30.

[30] Fermi, E. Versuch einer theorie der β-strahlen. i. *Zeitschrift für Physik* **88**, 161–177 (1934). URL https://doi.org/10.1007/BF01351864. Citado na página 31.

[31] Cowan, C. L., Reines, F., Harrison, F. B., Kruse, H. W. & McGuire, A. D. Detection of the free neutrino: A confirmation. *Science* **124**, 103–104 (1956). URL 10.1126/science.124.3212.103. Citado 2 vezes nas páginas 31 and 59.

[32] Majorana, E. Teoria simmetrica dell'elettrone e del positrone. *Il Nuovo Cimento (1924-1942)* **14**, 171–184 (1937). URL https://doi.org/10.1007/BF02961314. Citado na página 32.

[33] Adams, D. *et al.* Improved limit on neutrinoless double-beta decay in te 130 with cuore. *Physical review letters* **124**, 122501 (2020). URL https://doi.org/10.1103/PhysRevLett.124.122501. Citado na página 32.

[34] Armengaud, E. *et al.* A new limit for neutrinoless double-beta decay of 100 mo from the cupid-mo experiment (cupid-mo collaboration). *Physical Review Letters* **126**, 181802 (2021). URL https://doi.org/10.1103/PhysRevLett.126.181802ï¿¿. Citado na página 32.

[35] Arnquist, I. *et al.* Final result of the majorana demonstrator's search for neutrinoless double-β decay in ge 76. *Physical Review Letters* **130**, 062501 (2023). URL https://doi.org/10.1103/PhysRevLett.130.062501. Citado na página 32.

[36] Lande, K. *et al.* Solar neutrino observations with the homestake 37cl detector. In *AIP Conference Proceedings*, vol. 243, 1122–1133 (American Institute of Physics, 1992). URL https://doi.org/10.1063/1.41548. Citado na página 32.

[37] Haxton, W. The solar neutrino problem. *Annual Review of Astronomy and Astrophysics* **33**, 459–503 (1995). URL https://doi.org/10.1146/annurev.aa.33.090195.002331. Citado na página 32.

[38] Pontecorvo, B. Mesonium and antimesonium. *Zhur. Eksptl'. i Teoret. Fiz.* **33** (1957). Citado 2 vezes nas páginas 32 and 40.

[39] Fukuda, Y. *et al.* Evidence for oscillation of atmospheric neutrinos. *Physical review letters* **81**, 1562 (1998). URL https://doi.org/10.1103/PhysRevLett.81.1562. Citado 3 vezes nas páginas 33, 40, and 59.

[40] Ahmad, Q. R. *et al.* Measurement of the rate of ν e+ d$\rightarrow$ p+ p+ e- interactions produced by b 8 solar neutrinos at the sudbury neutrino observatory. *Physical review letters* **87**, 071301 (2001). URL https://doi.org/10.1103/PhysRevLett.87.071301. Citado 2 vezes nas páginas 33 and 40.

[41] Gonzalez-Garcia, M. C., Maltoni, M. & Schwetz, T. Global analyses of neutrino oscillation experiments. *Nuclear Physics B* **908**, 199–217 (2016). URL https://doi.org/10.1016/j.nuclphysb.2016.02.033. Citado 2 vezes nas páginas 33 and 40.

[42] Maki, Z., Nakagawa, M. & Sakata, S. Remarks on the unified model of elementary particles. *Progress of Theoretical Physics* **28**, 870–880 (1962). URL https://doi.org/10.1143/PTP.28.870. Citado na página 34.

[43] Aguilar-Arevalo, A. *et al.* Miniboone and microboone joint fit to a 3+ 1 sterile neutrino scenario. *arXiv preprint arXiv:2201.01724* (2022). URL https://doi.org/10.48550/arXiv.2201.01724. Citado na página 34.

[44] Diaz, A., Argüelles, C., Collin, G., Conrad, J. & Shaevitz, M. Where are we with light sterile neutrinos? *Physics Reports* **884**, 1–59 (2020). URL https://doi.org/10.1016/j.physrep.2020.08.005. Citado na página 34.

[45] Gariazzo, S., Giunti, C., Laveder, M., Li, Y. & Zavanin, E. Light sterile neutrinos. *Journal of Physics G: Nuclear and Particle Physics* **43**, 033001 (2016). URL https://doi.org/10.1088/0954-3899/43/3/033001. Citado na página 34.

[46] Abe, K. *et al.* Measurements of neutrino oscillation parameters from the t2k experiment using 3.6×10^{21} protons on target. *arXiv preprint* (2023). URL https://doi.org/10.48550/arXiv.2303.03222. Citado na página 36.

[47] Group, P. D. *et al.* Review of particle physics. *Progress of Theoretical and Experimental Physics* **2022**, 083C01 (2022). URL https://doi.org/10.1093/ptep/ptac097. Citado 2 vezes nas páginas 36 and 50.

[48] Sakurai, J. J. & Commins, E. D. Modern quantum mechanics, revised edition (1995). Citado na página 37.

[49] Kayser, B. On the quantum mechanics of neutrino oscillation. *Physical Review D* **24**, 110 (1981). URL https://doi.org/10.1103/PhysRevD.24.110. Citado 2 vezes nas páginas 37 and 51.

[50] Kiers, K., Nussinov, S. & Weiss, N. Coherence effects in neutrino oscillations. *Physical Review D* **53**, 537 (1996). URL https://doi.org/10.1103/PhysRevD.53.537. Citado 3 vezes nas páginas 37, 39, and 51.

[51] Comsa, G. Comment on" direct measurement of the longitudinal coherence length of a thermal neutron beam". *Physical Review Letters* **51**, 1105 (1983). URL https://doi.org/10.1103/PhysRevLett.51.1105. Citado na página 39.

[52] Maltoni, M. & Yu. Smirnov, A. Solar neutrinos and neutrino physics. *The European Physical Journal A* **52**, 87 (2016). URL https://doi.org/10.1140/epja/i2016-16087-0. Citado na página 39.

[53] Xu, X.-J., Wang, Z. & Chen, S. Solar neutrino physics. *Progress in Particle and Nuclear Physics* 104043 (2023). URL https://doi.org/10.1016/j.ppnp.2023.104043. Citado na página 39.

[54] Cleveland, B. T. *et al.* Measurement of the solar electron neutrino flux with the homestake chlorine detector. *The Astrophysical Journal* **496**, 505 (1998). URL https://doi.org/10.1086/305343. Citado na página 40.

[55] Zha, S., O'Connor, E. P. & da Silva Schneider, A. Progenitor dependence of hadron-quark phase transition in failing core-collapse supernovae. *The Astrophysical Journal* **911**, 74 (2021). URL https://doi.org/10.3847/1538-4357/abec4c. Citado na página 41.

[56] Wolfenstein, L. Neutrino oscillations in matter. *Physical Review D* **17**, 2369–2374 (1978). URL https://doi.org/10.1103/PhysRevD.17.2369. Citado 2 vezes nas páginas 41 and 42.

[57] Smirnov, A. Y. The msw effect and solar neutrinos. *arXiv preprint* (2003). URL https://doi.org/10.48550/arXiv.hep-ph/0305106. Citado na página 41.

[58] Mikheyev, S. & Smirnov, A. Y. Resonant amplification of ν oscillations in matter and solar-neutrino spectroscopy. *Il Nuovo Cimento C* **9**, 17–26 (1986). Citado na página 42.

[59] Bahcall, J. N. & Bethe, H. Solution of the solar-neutrino problem. *Physical Review Letters* **65**, 2233 (1990). URL https://doi.org/10.1103/PhysRevLett.65.2233. Citado na página 42.

[60] Kuo, T.-K. & Pantaleone, J. Solar-neutrino problem and three-neutrino oscillations. *Physical review letters* **57**, 1805 (1986). URL https://doi.org/10.1103/PhysRevLett.57.1805. Citado na página 43.

[61] Botella, F., Lim, C.-S. & Marciano, W. Radiative corrections to neutrino indices of refraction. *Physical Review D* **35**, 896 (1987). URL https://doi.org/10.1103/PhysRevD.35.896. Citado na página 44.

[62] Fukugita, M. & Yanagida, T. *Physics of Neutrinos: and Application to Astrophysics* (Springer Science & Business Media, 2013). Citado na página 44.

[63] Parke, S. J. Nonadiabatic level crossing in resonant neutrino oscillations. *Physical Review Letters* **57**, 1275 (1986). URL https://doi.org/10.1103/PhysRevLett.57.1275. Citado na página 47.

[64] Landau, L. On the theory of transfer of energy at collisions ii. *Phys. Z. Sowjetunion* **2**, 118 (1932). Citado na página 47.

[65] Zener, C. Non-adiabatic crossing of energy levels. *Proceedings of the Royal Society of London. Series A, Containing Papers of a Mathematical and Physical Character*

137, 696–702 (1932). URL https://doi.org/10.1098/rspa.1932.0165. Citado na página 47.

[66] Mikheev, S. & Smirnov, A. Y. Resonance amplification of oscillations in matter and spectroscopy of solar neutrinos. *Yadernaya Fizika* **42**, 1441–1448 (1985). Citado na página 47.

[67] Janka, H.-T. & Hillebrandt, W. Monte carlo simulations of neutrino transport in type ii supernovae. *Astronomy and Astrophysics Supplement Series* **78**, 375–397 (1989). URL https://legacy.adsabs.harvard.edu/full/1989A%26AS...78..375J. Citado 2 vezes nas páginas 47 and 74.

[68] Brown, G., Bethe, H. & Baym, G. Supernova theory. *Nuclear Physics A* **375**, 481–532 (1982). URL https://doi.org/10.1016/0375-9474(82)90025-2. Citado 2 vezes nas páginas 47 and 74.

[69] Agafonova, N. Y. *et al.* Study of the effect of neutrino oscillations on the supernova neutrino signal in the lvd detector. *Astroparticle Physics* **27**, 254–270 (2007). URL https://doi.org/10.1016/j.astropartphys.2006.11.004. Citado na página 50.

[70] Abe, K. *et al.* Solar neutrino measurements in super-kamiokande-iv. *Physical Review D* **94**, 052010 (2016). URL https://doi.org/10.1103/PhysRevD.94.052010. Citado na página 51.

[71] Dziewonski, A. M. & Anderson, D. L. Preliminary reference earth model. *Physics of the earth and planetary interiors* **25**, 297–356 (1981). URL https://doi.org/10.1016/0031-9201(81)90046-7. Citado na página 52.

[72] Dighe, A. S., Keil, M. T. & Raffelt, G. G. Identifying earth matter effects on supernova neutrinos at a single detector. *Journal of Cosmology and Astroparticle Physics* **2003**, 006 (2003). URL https://doi.org/10.1088/1475-7516/2003/06/006. Citado na página 57.

[73] Strumia, A. & Vissani, F. Precise quasielastic neutrino/nucleon cross-section. *Physics Letters B* **564**, 42–54 (2003). URL https://doi.org/10.1016/S0370-2693(03)00616-6. Citado na página 60.

[74] Abe, K. *et al.* First gadolinium loading to super-kamiokande. *Nuclear Instruments and Methods in Physics Research Section A: Accelerators, Spectrometers, Detectors and Associated Equipment* **1027**, 166248 (2022). URL https://doi.org/10.1016/j.nima.2021.166248. Citado na página 60.

[75] Simpson, C. *et al.* Sensitivity of super-kamiokande with gadolinium to low energy antineutrinos from pre-supernova emission. *The Astrophysical Journal* **885**, 133 (2019). URL https://doi.org/10.3847/1538-4357/ab4883. Citado na página 60.

[76] Suzuki, Y. The super-kamiokande experiment. *The European Physical Journal C* **79**, 1–18 (2019). URL https://doi.org/10.1140/epjc/s10052-019-6796-2. Citado na página 61.

[77] Nakahata, M. *et al.* Calibration of super-kamiokande using an electron linac: The super-kamiokande collaboration. *Nuclear Instruments and Methods in Physics Research Section A: Accelerators, Spectrometers, Detectors and Associated Equipment* **421**, 113–129 (1999). URL https://doi.org/10.1016/S0168-9002(98)01200-5. Citado 2 vezes nas páginas 61 and 62.

[78] De Gouvêa, A., Martinez-Soler, I. & Sen, M. Impact of neutrino decays on the supernova neutronization-burst flux. *Physical Review D* **101**, 043013 (2020). URL https://doi.org/10.1103/PhysRevD.101.043013. Citado 2 vezes nas páginas 61 and 66.

[79] Apollonio, M. *et al.* Determination of neutrino incoming direction in the chooz experiment and its application to supernova explosion location by scintillator detectors. *Physical Review D* **61**, 012001 (1999). URL https://doi.org/10.1103/PhysRevD.61.012001. Citado 2 vezes nas páginas 62 and 79.

[80] Suzuki, Y. The sun, neutrinos and super-kamiokande. *Proceedings of the Japan Academy, Series B* **96**, 204–233 (2020). Citado na página 62.

[81] Kuramoto, T., Fukugita, M., Kohyama, Y. & Kubodera, K. Neutrino-induced reaction cross sections at intermediate energies for chlorine and water detectors. *Nuclear Physics A* **512**, 711–736 (1990). URL https://doi.org/10.1016/0375-9474(90)90232-B. Citado na página 62.

[82] Abe, K. *et al.* Hyper-kamiokande design report. *arXiv preprint* (2018). URL https://doi.org/10.48550/arXiv.1805.04163. Citado na página 64.

[83] Abi, B. *et al.* The dune far detector interim design report volume 1: Physics, technology and strategies. *arXiv preprint* (2018). URL https://doi.org/10.48550/arXiv.1807.10334. Citado na página 64.

[84] Acciarri, R. *et al.* Summary of the second workshop on liquid argon time projection chamber research and development in the united states. *Journal of instrumentation* **10**, T07006 (2015). URL https://doi.org/10.1088/1748-0221/10/07/T07006. Citado na página 64.

[85] Abi, B. *et al.* Deep underground neutrino experiment (dune), far detector technical design report, volume ii: Dune physics. *arXiv preprint arXiv:2002.03005* (2020). Citado 2 vezes nas páginas 64 and 65.

[86] Stoenner, R., Schaeffer, O. & Katcoff, S. Half-lives of argon-37, argon-39, and argon-42. *Science* **148**, 1325–1328 (1965). URL https://doi.org/10.1126/science.148.3675.1325. Citado na página 65.

[87] Benetti, P. *et al.* Measurement of the specific activity of 39ar in natural argon. *Nuclear Instruments and Methods in Physics Research Section A: Accelerators, Spectrometers, Detectors and Associated Equipment* **574**, 83–88 (2007). URL https://doi.org/10.1016/j.nima.2007.01.106. Citado na página 65.

[88] An, F. *et al.* Neutrino physics with juno. *Journal of Physics G: Nuclear and Particle Physics* **43**, 030401 (2016). Citado na página 67.

[89] Laha, R., Beacom, J. F. & Agarwalla, S. K. New power to measure supernova ν_e with large liquid scintillator detectors. *arXiv preprint* (2014). URL https://doi.org/10.48550/arXiv.1412.8425. Citado na página 68.

[90] Katti, S. & Rao, A. V. Handbook of the poisson distribution (1968). Citado na página 77.

[91] Friedland, A. & Li, S. W. Understanding the energy resolution of liquid argon neutrino detectors. *Physical Review D* **99**, 036009 (2019). URL https://doi.org/10.1103/PhysRevD.99.036009. Citado na página 77.

[92] Abi, B. *et al.* Supernova neutrino burst detection with the deep underground neutrino experiment. *The European Physical Journal C* **81**, 1–26 (2021). URL https://doi.org/10.1140/epjc/s10052-021-09166-w. Citado na página 77.

[93] Beacom, J. F. & Vogel, P. Can a supernova be located by its neutrinos? *Physical Review D* **60**, 033007 (1999). URL https://doi.org/10.1103/PhysRevD.60.033007. Citado na página 79.

[94] Burrows, A., Klein, K. & Gandhi, R. The future of supernova neutrino detection. *Physical Review D* **45**, 3361 (1992). URL https://doi.org/10.1103/PhysRevD.45.3361. Citado na página 79.

[95] Özel, F., Psaltis, D., Narayan, R. & Villarreal, A. S. On the mass distribution and birth masses of neutron stars. *The Astrophysical Journal* **757**, 55 (2012). URL https://doi.org/10.1088/0004-637X/757/1/55. Citado 2 vezes nas páginas 90 and 91.

[96] Barkov, M. V. & Komissarov, S. S. Recycling of neutron stars in common envelopes and hypernova explosions. *Monthly Notices of the Royal Astronomical Society* **415**, 944–958 (2011). URL https://doi.org/10.1111/j.1365-2966.2011.18762.x. Citado na página 90.

[97] Farrow, N., Zhu, X.-J. & Thrane, E. The mass distribution of galactic double neutron stars. *The Astrophysical Journal* **876**, 18 (2019). URL https://doi.org/10.3847/1538-4357/ab12e3. Citado na página 91.

[98] Farr, W. M. & Chatziioannou, K. A population-informed mass estimate for pulsar j0740+ 6620. *Research Notes of the AAS* **4**, 65 (2020). URL https://doi.org/10.3847/2515-5172/ab9088. Citado na página 91.

[99] Landry, P. & Read, J. S. The mass distribution of neutron stars in gravitational-wave binaries. *The Astrophysical Journal Letters* **921**, L25 (2021). URL https://doi.org/10.3847/2041-8213/ac2f3e. Citado na página 91.

[100] Lattimer, J. M. & Prakash, M. Neutron star observations: Prognosis for equation of state constraints. *Physics reports* **442**, 109–165 (2007). URL https://doi.org/10.1016/j.physrep.2007.02.003. Citado na página 91.

[101] Ohnaka, K. *et al.* High spectral resolution imaging of the dynamical atmosphere of the red supergiant antares in the co first overtone lines with vlti/amber. *Astronomy & Astrophysics* **555**, A24 (2013). URL https://doi.org/10.1051/0004-6361/201321063. Citado na página 93.

[102] Joyce, M. *et al.* Standing on the shoulders of giants: New mass and distance estimates for betelgeuse through combined evolutionary, asteroseismic, and hydrodynamic simulations with mesa. *The Astrophysical Journal* **902**, 63 (2020). URL https://doi.org/10.3847/1538-4357/abb8db. Citado na página 93.

[103] Fryer, C. L. *et al.* Core collapse supernovae and multi-messenger astronomy. *Bulletin of the American Astronomical Society* **51** (2019). URL https://www.osti.gov/biblio/1571744. Citado na página 93.

[104] Ott, C. D. Probing the core-collapse supernova mechanism with gravitational waves. *Classical and Quantum Gravity* **26**, 204015 (2009). URL https://doi.org/10.1088/0264-9381/26/20/204015. Citado na página 93.

[105] Yakunin, K. N. *et al.* Gravitational waves from core collapse supernovae. *Classical and Quantum Gravity* **27**, 194005 (2010). URL https://doi.org/10.1088/0264-9381/27/19/194005. Citado na página 93.

[106] Linzer, N. & Scholberg, K. Triangulation pointing to core-collapse supernovae with next-generation neutrino detectors. *Physical Review D* **100**, 103005 (2019). URL https://doi.org/10.1103/PhysRevD.100.103005. Citado na página 101.

Appendix

APPENDIX A – Fitting for α and $\langle E \rangle$ varying the distance

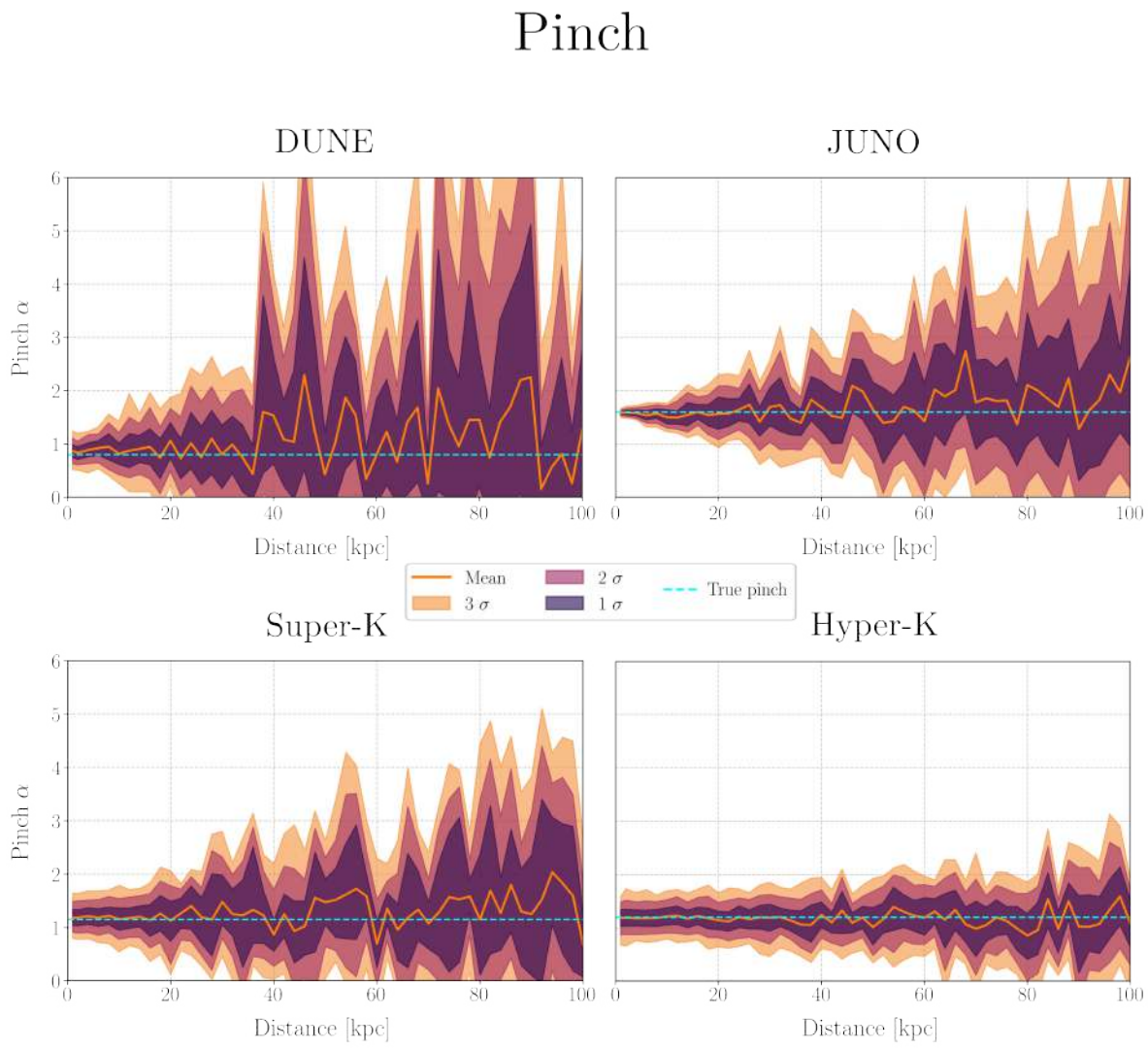

Figure 41 – Pinch reconstruction from detection spectrum for all four detectors (DUNE - *top left*, JUNO - *top right*, Super-Kamiokande - *bottom left* and Hyper-Kamiokande - *bottom right*). Dashed lines represent the true value for the parameter that should be observed in each detector.

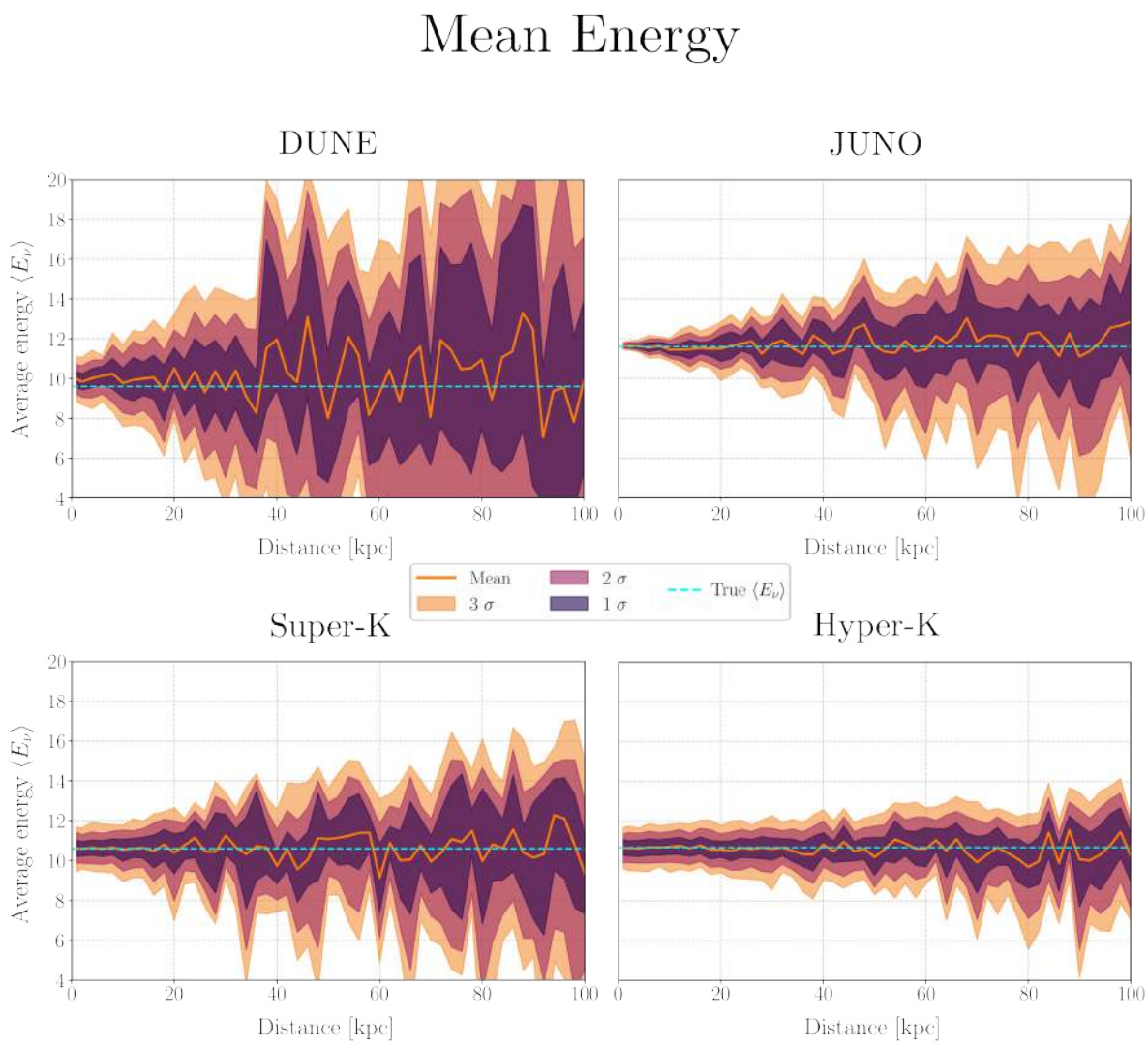

Figure 42 – Mean energy reconstruction from detection spectrum for all four detectors (DUNE - *top left*, JUNO - *top right*, Super-Kamiokande - *bottom left* and Hyper-Kamiokande - *bottom right*). Dashed lines represent the true value for the parameter that should be observed in each detector.